CARBON NANOTUBE TRANSISTORS: CAPACITANCE MEASUREMENTS, LOCALIZED DAMAGE, AND USE AS GOLD SCAFFOLDING

A Dissertation

Presented to the Faculty of the Graduate School

of Cornell University

in Partial Fulfillment of the Requirements for the Degree of

Doctor of Philosophy

by

Luke Anthony Kaiser Donev

May 2009

CARBON NANOTUBE TRANSISTORS: CAPACITANCE MEASUREMENTS, LOCALIZED DAMAGE, AND USE AS GOLD SCAFFOLDING

Luke Anthony Kaiser Donev, Ph.D.

Cornell University 2009

Carbon nanotubes are incredible materials with interesting mechanical and electrical properties. This thesis presents diverse experiments based on carbon nanotube transistors.

We measured the capacitance of individual carbon nanotubes. The density of states of a carbon nanotube will influence the tube's capacitance. We report good agreement with theory and that we successfully probe the tube's density of states.

We show it is possible to open holes into the carbon nanotubes without completely destroying the conductance of the tube. The application of localized damage to nanotube transistors opens up several exciting potential device geometries.

We also present several experiments where carbon nanotubes are used as nanoscale scaffolding for the deposition and manipulation of gold. Nanometer scale balls of gold are deposited on nanotubes from an atomic force microscope. Nanotubes are also used to influence gold wires undergoing electromigration.

This thesis demonstrates just some of many novel techniques being applied to carbon nanotubes, and lays groundwork for the exciting applications nanotubes will help realize.

BIOGRAPHICAL SKETCH

Luke Anthony Kaiser Donev was born on August 19, 1979 in Toronto, Canada. He was greeted by his parents Mary and Stef and brother Jason. After some international travel, the family added Luke's sister Amanda in 1983, and then moved to southern California, U.S.A. in 1986. After attending Atherwood, El Tejon, and Bakersfield High School, Luke went to the University of California at Davis on an A.F.R.O.T.C. scholarship as a physics major in 1997. Luke figured out he could pay for college in other ways (including CalGrant and eventually a Regents scholarship and a Goldwater scholarship), left R.O.T.C. and began working in the lab of Professor Rena Zieve. His time in Professor Zieve's lab was productive, instructive, and an excellent opportunity. It was one of many joyful experiences at Davis, which culminated in graduation with highest honors, and the chancellor's award for excellence in undergraduate research for his senior thesis on quantized vortices in superfluid helium.

Luke then went on to graduate school at Cornell University in 2001. He joined the research group of Professor Paul McEuen, who kindly didn't look too closely at how much fun Luke was having doing science outreach, dancing, machining, woodworking, cooking, and judo. Luke picked up a masters degree in 2004, and is excited about graduating 24th grade and getting his doctorate.

Dedicated to those who find this useful and further this work.

ACKNOWLEDGEMENTS

It's weird to think that I've been in graduate school for almost a third of my life. My time in Ithaca has been an incredible learning experience both outside and inside the lab. There are a lot of people I am grateful to have had in my life who helped me both to and through graduate school. I have undoubtedly forgotten some. The process of compiling a thesis has left me a little discombobulated. I will happily sign a copy of the thesis as amends.

To my committee, and my adviser Professor Paul McEuen, I say thank you. Paul has worked hard over the years teaching science, the process of science, when not to quit; and most importantly, how to communicate. I still have much to learn, but I appreciate his guidance along the way.

I'm grateful to all the labmates I've gotten to interact with over the years, and after more than seven years, there have been a lot. Jiwoong Park, Abhay Pasupathy, Jacob Grose, Radek Bialczak, and Professor Dan Ralph brought me into the low temperature corridor and showed an impressive dedication to research. I'm grateful for my summer at the University of Erlangen with Professor Alexey Ustinov and his group; Marcus Schuster, Andreas Wallraff, Francesca Pignatelli, Abdufarrukh Abdumalikov, and Alexander Kemp; for showing me there are other ways to approach being a physicist than the American mindset.

I've had a bevy of excellent interactions with professors and teachers while at Cornell. Professor Erich Mueller gave me many hours of help with Mathmatica and my A exam, and showed me what it is theorists do all day. Professor David Tanenbaum is a wonderful example of long-term enthusiasm for being a physics professor. Professor James Sethna is infectiously enthusiastic about everything. Professor Louis Albright is dedicated to getting people to look at the larger picture. Tom Cook, Abby Nash, Bob Snedeker, Rob Ilic, and Eric Smith

were invaluable in the wealth of their experience, their willingness to pass on hands-on skills, and the indirect reminders to enjoy life outside of lab.

When I joined the McEuen group, Ji-Yoong Park, Alex Yanson, Vera Sazonova, Sami Rosenblatt, Scott Bunch, Markus Brink, and Ethan Minot were senior members who made research seem easy; as though they had it all figured out. Ethan in particular helped me grow my first nanotubes and was inspirational in balancing work and recreation. It was weird as those ranks began to thin and I was suddenly one of the old timers. It was nice to have new excellent post-docs like Patrycja Paruch, Ken Bosnick, Zhaohui Zhong, and Jun Zhu around to talk with about physics, career paths, and everything else. I owe a special debt to the post-doc Shahal Ilani, an insightful and driven experimentalist without whom the capacitance experiment in this thesis would be a shadow of what it is.

Xinjian Zhou and I started in the McEuen group at the same time. While we never worked closely, he taught me indirectly to appreciate a lot of things I had taken for granted about operating in one's native country. Lisa Larrimore started after I did and showed what dedication, focus, and organization can do (as she's already graduated). Her well-organized thesis [63](also done in L^AT_EX) was exceptionally useful in constructing the bibliography of this one. She and her husband Nick are also phenomenal cooks I was happy to learn from. For one summer I worked with Derrick Stokes as an REU and I'm grateful for the insight and growing opportunity that provided. Hiram Conley was also at Cornell for a summer, and was a fantastic contribution to our research effort and the group ultimate frisbee team. Although the research is not represented here, I was fortunate to play with and learn on the impressive optical system built by Yaqiong Xu and Arthur Barnard

I am full of confidence that the group will continue to excel after I leave. Arend van der Zand has an inspirationally analytic mind and appreciation for life. Samantha Roberts' resilience and determination are exemplary. Nathan Gabor is the best example of a renaissance scientist I've ever met. Wrapping up my research has prevented me from getting to know Jonathan Alden, Melina Blees, and Xiaodong Xu particularly well, but they are already working on exciting research that I trust will move them through Cornell faster than I did.

It has been interesting to see Jiwoong come back as Professor Park. I'm grateful for the chance to work in his lab with his very talented and dedicated students Mark Levendorf, Adam Wei Tsen, and Daniel Joh. I wish them all a quick completion on the adjacent building, and a minimum of vibrational noise.

The staff of the physics department deserves a special thanks for making it possible to do the research we do. I'm particularly grateful to have interacted with Douglas Milton, Vince Kotmel, and Lisa Margosian. I'd also like to thank Nevjinder Singhota, Kevin Dilley, and Jane Earle for maintaining a top notch outreach program. They made outreach enjoyable, productive, and efficient so we could get back to research. Fellow graduate student Amy Richter was a fabulous partner in many outreach activities, and I thank her for having a complementary skill set.

Graduate school has been only a part of my time in Ithaca. The social networks that opened up to me have been incalculably valuable. I'm thankful to senseis Bill Myers and M.P. Rouse, for the judo club they maintain, and to my fellow judoka over the years for throwing me around and keeping me sane. Thank you to Cindy Overstreet and the rest of the Ithaca swing dancers for many wonderful times. Karen Veale, Steve Weidner, Greg and Petra Trembley, and the rest of the local SCAdians, I will take the random skills you've given me

everywhere I go. I'm incredibly grateful for the vibrant contradance community here. Organizers Ted Crane, Pamela Goddard, and the Hands Four board have given a real gift to the community. There are too many dancers to name, but I'm indebted to the community as a whole. Contra was an unexpected joy to discover, and I anticipate it growing to be a larger part of my life.

My luck with housemates has gotten progressively better the longer I've lived in Ithaca. From living on my own, to Jon Peck and Rick Clinite who made S&S livable (with the help of escaping to Jerry Shipman's parties), to Triphammer, where I discovered the joys of community living. Bryant Adams, Sarah Rose Clune, and Anna Schliessmann taught me what was important in a home. Bryant Adams, Sarah Rose Adams, Tim Ball (and Lydia Dempsey) gave me a home with music. Bryant, Sarah Rose, Gail Blake, Jennifer Dotson, and Corvid Adams have made a home happen even during my thesis.

Of my Ithaca friends, I owe a special thank you to Bryant, for introducing me to Triphammer and contradancing, and being a wonderful resource and thoughtful friend. He and Sarah Rose have provided untold hours of conversation, support, honesty, and friendship. Thank you to Anna, for shedding light on things I didn't know needed illumination. Thanks to Jan Irvahn, for the juggling and the awareness of graduate school as something that could be left. Thank you to Erica Tabbert, Karlyn D. Beer, and Katie Burns, for the dances and the understanding. I still don't understand how I was blessed with your friendships. Riley Sisson deserves thanks for his patience, care, and insight. I was supported and had my life enriched by Abra Brisbin. I'm grateful to her, and know she will make an excellent professor, mentor, and teacher. Sophia Smith-Savedoff has probably most clearly seen what the end of my graduate trajectory has been like. Her patience, support, cooking, motivation, and presence have

been recharging and invigorating.

I would not have made it to Cornell and Ithaca without the benefit of many people earlier in my life. I fondly remember my undergraduate days at U.C. Davis. I owe thanks to Professor Rena Zieve for bringing me into her lab and getting me excited about being an experimentalist. Thank you to Randy Harris for being an incredibly gifted teacher and using our doubts to make us learn. Mick and Sarah Martin; Amber and Chris Marsh; Joan Bisbing; Jeanne Fishback and her family; Nick and Melissa Wunschel; Chrissy Brady; Dawn Burnell; Anthony Parisi; Jessica Hunt; and Wendy Alcaraz have been constant in their support across a continent and countless changes in their own lives.

I'm grateful to the friends and teachers from my time in Bakersfield. Thanks go to Mario Martinez and his family for their friendship and cutting down on my commute. Thank you to Ms. Hall for teaching me to check my work. I'm grateful to Mr. Wilmot and Mr. Nelson whose science classes are still shaping what I'm doing with my life. Thank you to John Hazlett, for his friendship, and the reminder that there are some things that defy explanation.

Last but certainly not least, thank you to my family. Thank you to my brother Jason for fighting battles so I wouldn't have to, blazing trails I didn't know existed, letting me learn from his experiences, and the labrats. Thank you to my sister Amanda for support, a sense of rationality at all hours, and hubris deflation. Flo, Don, Kim, Kiera, Kelson, Kit, Annemarie, grandparents, and the rest of my extended family; thank you for the intangible international network of support. To my mom and dad, Mary and Stef, whose extraordinary help with this thesis is par for the course in their incredible support throughout my life, thank you. I love you all.

Ithaca, January 2009

TABLE OF CONTENTS

LIST OF FIGURES

CHAPTER 1

OVERVIEW

This thesis describes three experiments that focus on carbon nanotubes. Carbon nanotubes are hollow straws of carbon of various lengths that are nanometers in diameter. They are rolled up sheets of the honeycomb graphite lattice. Figure 1.1 shows a short segment of a carbon nanotube.

Carbon nanotubes have one of the highest strength to weight ratios of any known material and are chemically and thermally resilient. They are also conductive, creating one-dimensional wires and semiconductors [102]. There is evidence that their properties have been used for centuries [99], and have naturally occurred for millennium [80], but their structure wasn't directly observed until 1991 [45]. There is an extensive amount of research into carbon nanotubes, with innumerable applications. The research presented here is a very small part of an active field of research.

The relevant attributes of carbon nanotubes for the experiments in this thesis are their small size, high aspect ratio, resilience, and electronic characteristics. We'll explore some of the basic theory of carbon nanotubes in chapter 2. Chapter 3 deals with the process of creating transistors based on carbon nanotubes. These transistors will be the basis of the experiments in this thesis.

Chapter 4 discusses capacitance measurements and their use as a probe of the electronic states of the carbon nanotube. Theoretical predictions are compared with measurements for the capacitance of an individual carbon nanotube. This measurement is relevant for electronic applications based on carbon nanotubes, as well as providing insight into the fundamental physics of the tube.

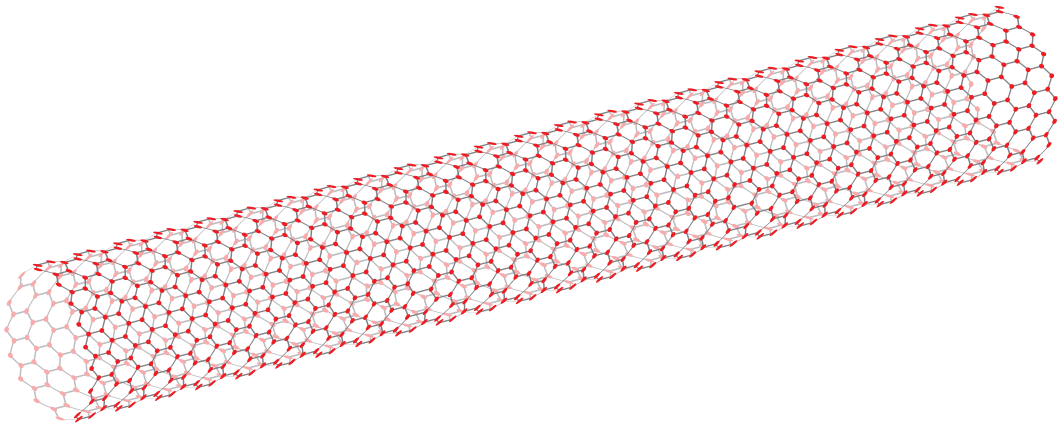

Figure 1.1: A short segment of carbon nanotube. Circles represent carbon atoms, and the connecting lines are bonds between atoms. The front half of the tube is colored darker than the back half for clarity.

Chapter 5 looks at partially cutting into a carbon nanotube. We use an oxygen plasma to burn holes into the tube without completely destroying its conductivity. We then look at the structure, stability, and sensitivity of an opened nanotube, as well as potential applications.

Chapter 6 highlights several ways nanotubes can be used as scaffolding for depositing and moving gold. Nanometer-sized gold balls are deposited onto nanotubes with an atomic force microscope. We also use carbon nanotubes to influence the formation of electromigrated gaps in wires crossing the tubes.

CHAPTER 2

CARBON NANOTUBE FUNDAMENTALS

This chapter will provide the basic theoretical background for the physical and electronic structure of carbon nanotubes. Several examples of the different structures of carbon nanotubes will be discussed, followed by an analysis of how that structure influences their electronic properties. Particular detail will be provided for determining the bandgap and density of states of the nanotube, as these will be of interest in chapter 4. We culminate by laying the foundations for looking at carbon nanotubes as field-effect transistors, which is how they will be used in the experiments in this thesis.

2.1 Physical structure of carbon nanotubes

A carbon nanotube is graphite rolled up into a tube. Graphite is a long known form of carbon in which the atoms are arranged in layers. Each layer is a honeycomb lattice of sp^2 hybridized carbon atoms. A single layer of graphite, called graphene, is shown at the top of figure 2.1. The vertices represent carbon atoms, and the lines are bonds. The grey diamond is the unit cell for graphene. The lattice vectors, shown in blue, can be used to tile a plane with the unit cell. The unit cell contains two atoms, shown in orange and green. There are two atoms in the unit cell because they are not equivalent, the mirror-imaged bonds coming off these atoms makes them distinct from each other. The bottom of figure 2.1 shows three graphene layers stacked on top of each other to form graphite. Usually the stack repeats after two layers, but other stackings are possible.

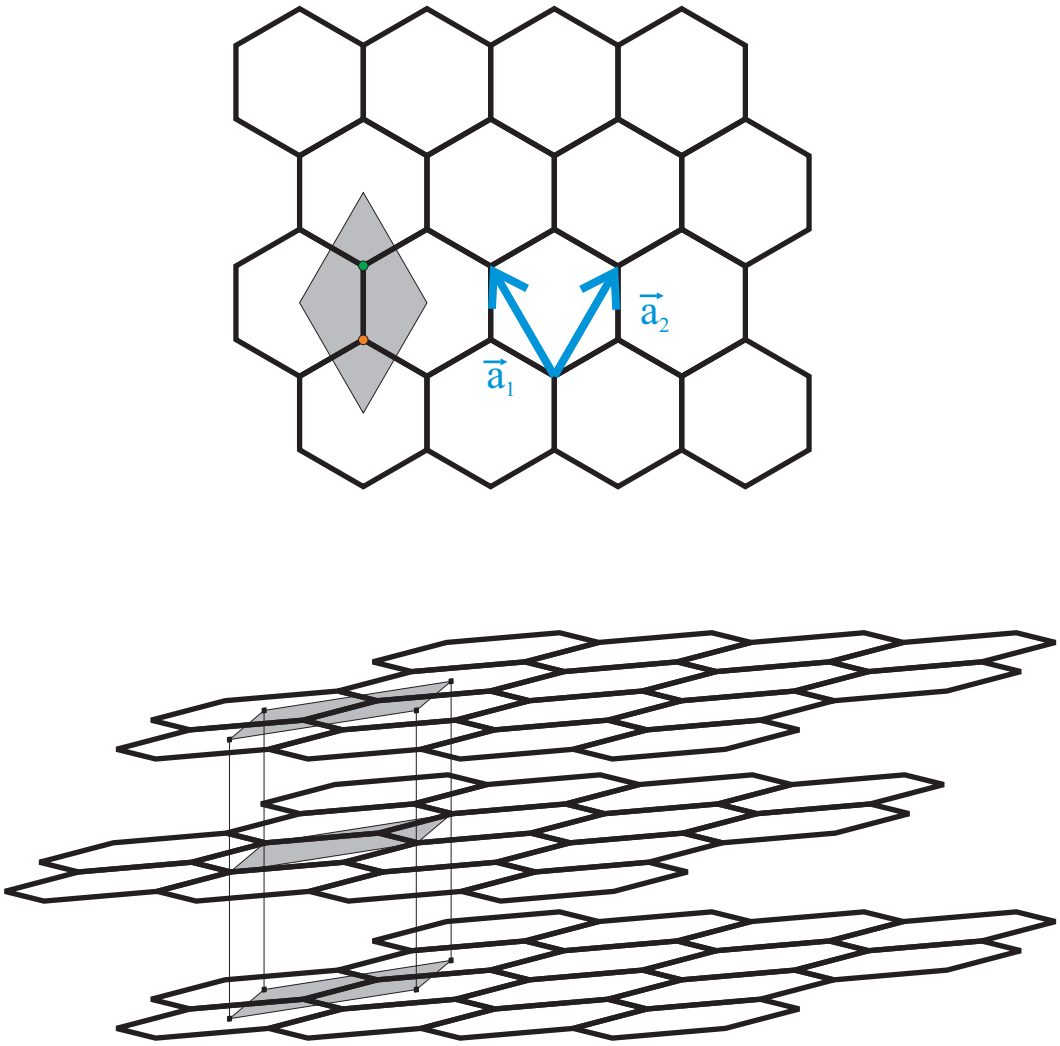

Figure 2.1: The structure of graphite. Top: the structure of one layer, showing the lattice vectors (blue) and unit cell (grey) for the layer. The two mirror-image lattice sites of the unit cell are shown in orange and green. Bottom: three stacked layers, showing the repeating pattern for layer stacking. Note that the second layer is offset laterally from the other two.

The lattice vectors for graphene have the equations:

$$\overrightarrow{a_1} = -\frac{a}{2}\hat{x} + \frac{a\sqrt{3}}{2}\hat{y}, \tag{2.1}$$

$$\overrightarrow{a_2} = +\frac{a}{2}\hat{x} + \frac{a\sqrt{3}}{2}\hat{y}. \tag{2.2}$$

And the relations:

$$\overrightarrow{a_1} \cdot \overrightarrow{a_1} = \overrightarrow{a_2} \cdot \overrightarrow{a_2} = a^2, \tag{2.3}$$

$$\overrightarrow{a_1} \cdot \overrightarrow{a_2} = \frac{a^2}{2}. \tag{2.4}$$

Where $|\overrightarrow{a}|$ is the lattice constant, $a = \sqrt{3} * a_{C-C} = \sqrt{3} * 0.142$ nm $= 0.246$ nm, where a_{C-C} is the carbon-carbon bond length of 0.142 nm in graphene. The third lattice vector for graphite is for the spacing between layers, has length 0.335 nm [102] , and won't be particularly pertinent in this thesis.

The structure of a carbon nanotube (CNT) is that of a graphite layer rolled into a closed cylinder. If just one layer of graphite is rolled into a cylinder, the single cylinder is called a single-walled carbon nanotube (SWCNT). If n layers are rolled around each other, the result is n concentric tubes. The concentric tubes are called a multi-wall carbon nanotube (MWCNT). Figure 2.2 shows one layer being rolled into one tube and three layers being rolled into three tubes. Most of our experiments focus on single-walled carbon nanotubes because they are a simpler system. For now, we will restrict our discussion to single-walled tubes.

Although we've shown featureless sheets in figure 2.2, the structure of our graphene sheets makes rolling them up more interesting. The first discovery of nanotubes where the structure was visualized was in 1991 using a Transmission Electron Microscope [45]. The symmetry of the honeycomb lattice allows for many discrete ways to roll up the sheet. How the sheet is rolled will determine

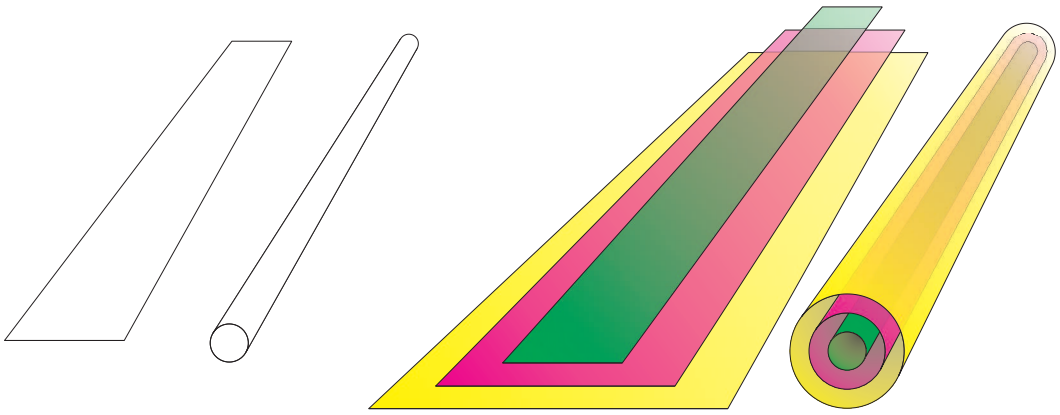

Figure 2.2: On the left, the white sheet is rolled into a single tube. On the right, three sheets (colored for clarity) are rolled into three concentric cylinders.

the diameter of the tube and, as we'll see in section 2.2, the electrical properties. Graphene has two mirror-image atom sites (orange and green points shown in figure 2.1). Picking any two points of the same type (i.e. two of the orange class or two of the green class) and rolling the sheet such that those points overlap creates a tube. We'll now look at several examples.

Figure 2.3 shows a graphene layer. The lattice vectors are in blue, and a unit cell is marked in grey. The red vector $\overrightarrow{C_h}$ links two sites of the same type (orange) that will be rolled on top of each other to create a tube. The tube consists of the atoms that are inside the width specified by $\overrightarrow{C_h}$, shown by the dotted lines. The tube this represents is shown in figure 2.4.

$\overrightarrow{C_h}$ is described by integer multiples of the lattice vectors, in this case $4\overrightarrow{a_1}+2\overrightarrow{a_2}$ (shown in figure 2.3 in light blue). $\overrightarrow{C_h}$ is called the chiral vector, as it specifies the chirality (amount of twist) of the tube. The tube corresponding to the chiral vector

$$\overrightarrow{C_h} = n\overrightarrow{a_1} + m\overrightarrow{a_2} \tag{2.5}$$

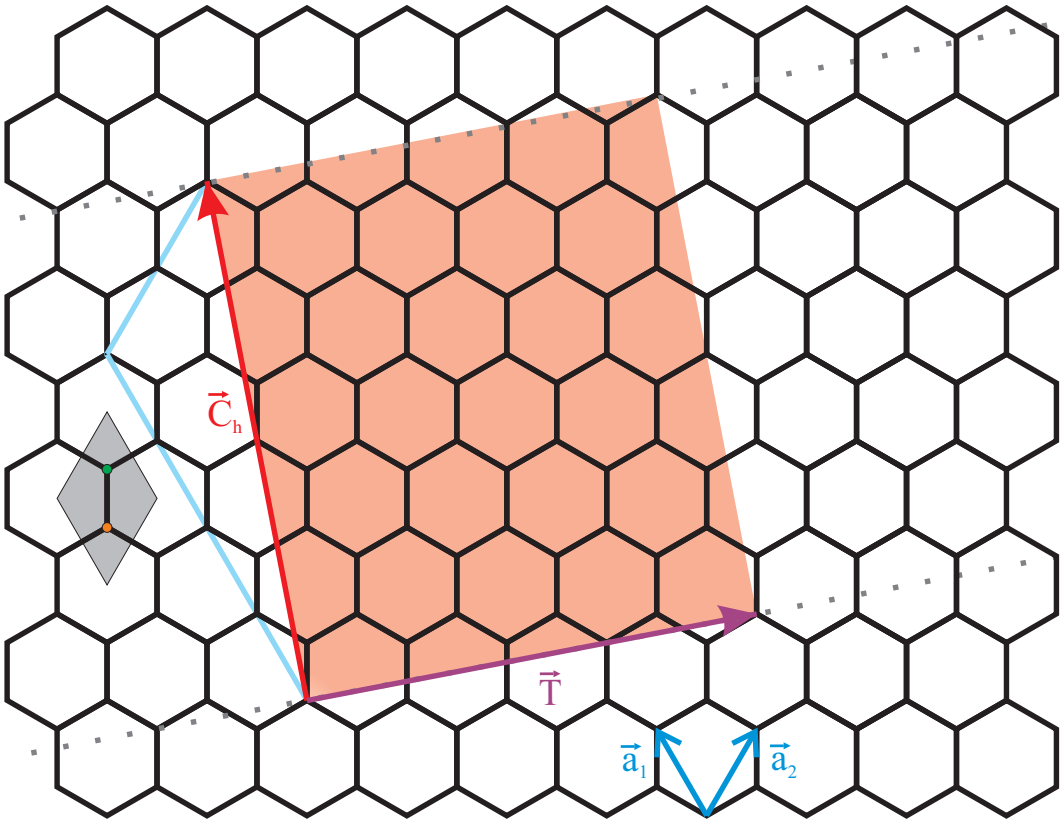

Figure 2.3: A graphene sheet, lattice vectors $\vec{a_1}$ and $\vec{a_2}$ in blue and unit cell shaded in grey. The red vector $\vec{C_h}$ describes how to roll up the graphene into a specific nanotube. The region between the dotted lines is rolled into a cylinder (the resulting tube shown in figure 2.4). The purple vector $\vec{T}$ is perpendicular to $\vec{C_h}$ and describes unit cell of the nanotube (shaded in peach). $\vec{C_h}$ here is $4\vec{a_1} + 2\vec{a_2}$, so this is called a (4,2) nanotube.

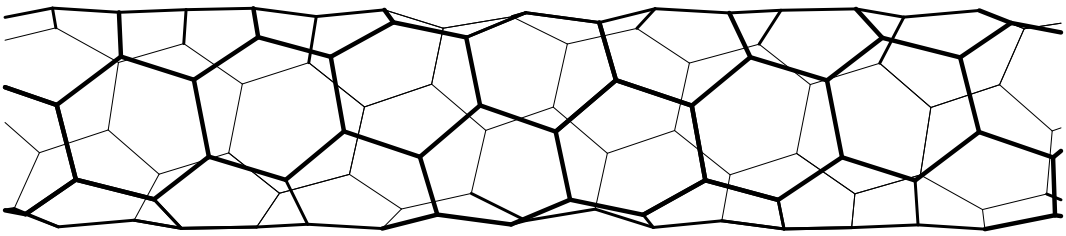

Figure 2.4: The (4,2) carbon nanotube created by rolling up a graphene sheet around the $4\vec{a_1} + 2\vec{a_2}$ vector shown in figure 2.3.

is called an (n, m) tube. By convention $n \geq m$. The magnitude of $\overrightarrow{C_h}$ is the circumference of the tube, and using equations 2.3 and 2.4:

$$|\overrightarrow{C_h}| = |n\overrightarrow{a_1} + m\overrightarrow{a_2}| = a\sqrt{n^2 + m^2 + nm}. \tag{2.6}$$

The purple arrow $\overrightarrow{T}$ in figure 2.3 is the translation vector of the nanotube, and determines the unit cell of the tube (shaded in peach). $\overrightarrow{T}$ is perpendicular to $\overrightarrow{C_h}$. It starts at the same initial point and goes until it exactly hits a lattice point of the same type. (In this example it passes through a green-type lattice point before reaching an orange one.) $|\overrightarrow{T}|$ is at most $\sqrt{3}|\overrightarrow{C_h}|$, but may be smaller if the symmetry of the tube results in $\overrightarrow{T}$ hitting an equivalent lattice position in a shorter distance.

We want to express $\overrightarrow{T}$ in terms of $\overrightarrow{a_1}$ and $\overrightarrow{a_2}$, and we know it is perpendicular to $\overrightarrow{C_h}$. We thus have $\overrightarrow{T} \cdot \overrightarrow{C_h} = (A\overrightarrow{a_1} + B\overrightarrow{a_2}) \cdot (n\overrightarrow{a_1} + m\overrightarrow{a_2}) = 0$. Using equations 2.3 and 2.4 reduces this to $a^2\left(An + Bm + \frac{Am}{2} + \frac{Bn}{2}\right) = 0$. Multiplying through by $2a^2$ and rearranging gives us the incompletely constrained equation $A(2n + m) = -B(2m + n)$. This works for $A = \frac{2m+n}{F}$ and $B = -\frac{2n+m}{F}$, where F is a common factor. Because we want $\overrightarrow{T}$ to go to the first lattice point equivalent to the initial one, we want $|\overrightarrow{T}|$ to be as small as possible. That means F should be the greatest common divisor of $(2m + n)$ and $(2n + m)$. We use $\gcd(p, q)$ to signify the greatest common divisor of two integers p and q. We can now succinctly write:

$$F = \gcd(2m + n, 2n + m) \tag{2.7}$$

$$\overrightarrow{T} = \left(\frac{2m + n}{F}\right)\overrightarrow{a_1} - \left(\frac{2n + m}{F}\right)\overrightarrow{a_2}, \tag{2.8}$$

$$|\overrightarrow{T}| = \frac{a\sqrt{3}}{F}\sqrt{n^2 + m^2 + nm} = \frac{\sqrt{3}|\overrightarrow{C_h}|}{F}. \tag{2.9}$$

The number of graphene unit cells in the nanotube's unit cell, N, is just the area of the nanotube cell divided by the area of the graphene unit cell:

$$N = \frac{|\overrightarrow{C_h} \times \overrightarrow{T}|}{|\overrightarrow{a_1} \times \overrightarrow{a_2}|} = \frac{(n^2 + m^2 + nm)\frac{a^2\sqrt{3}}{F}}{\frac{\sqrt{3}}{2}a^2} = 2\frac{n^2 + m^2 + nm}{F}. \tag{2.10}$$

Even though we tiled the lattice with a diamond, the area is the same as the hexagon of the graphene lattice, so the number of diamond-shaped graphene unit cells is the same as the number of hexagons in the nanotubes unit cell. N for our first example nanotube is 28, since F is 2 for a (4,2) tube.

Having used our first example to discuss the parameters of a nanotube, we now show two more examples that have special symmetries. Figure 2.5 shows a graphene lattice with a different chiral vector. The lattice vectors are again shown in blue, and here the chiral vector is $\overrightarrow{C_h} = 5\overrightarrow{a_1} + 5\overrightarrow{a_2}$. The special case where $n = m$ is called an armchair tube because the pattern of atoms along the circumference looks (a bit) like an armchair (pattern highlighted in yellow in figure 2.5, the armchair is on its side). The translation vector $\overrightarrow{T}$ describing the nanotube's unit cell is much shorter in this case because of the alignment of $\overrightarrow{C_h}$ with respect to the lattice. $\overrightarrow{T}$ hits another green-class lattice site well before reaching $\sqrt{3}|\overrightarrow{C_h}|$ in length, and is $|\overrightarrow{C_h}|/5\sqrt{3}$ because $F = 15$.

The nanotube formed by the chiral vector $\overrightarrow{C_h} = 5\overrightarrow{a_1} + 5\overrightarrow{a_2}$ is shown in figure 2.6. Note that the diameter of this tube is larger than the tube in figure 2.4, because the magnitude of the chiral vector is larger than the one in figure 2.3.

As a final example of graphene being rolled into a nanotube, we look at the case where the chiral vector is entirely along one lattice vector of the graphene. The graphene sheet for $\overrightarrow{C_h} = 5\overrightarrow{a_1} + 0\overrightarrow{a_2}$ is shown in figure 2.7. The nanotube formed by the chiral vector $\overrightarrow{C_h} = 5\overrightarrow{a_1} + 0\overrightarrow{a_2}$ is shown in figure 2.8. All nanotubes

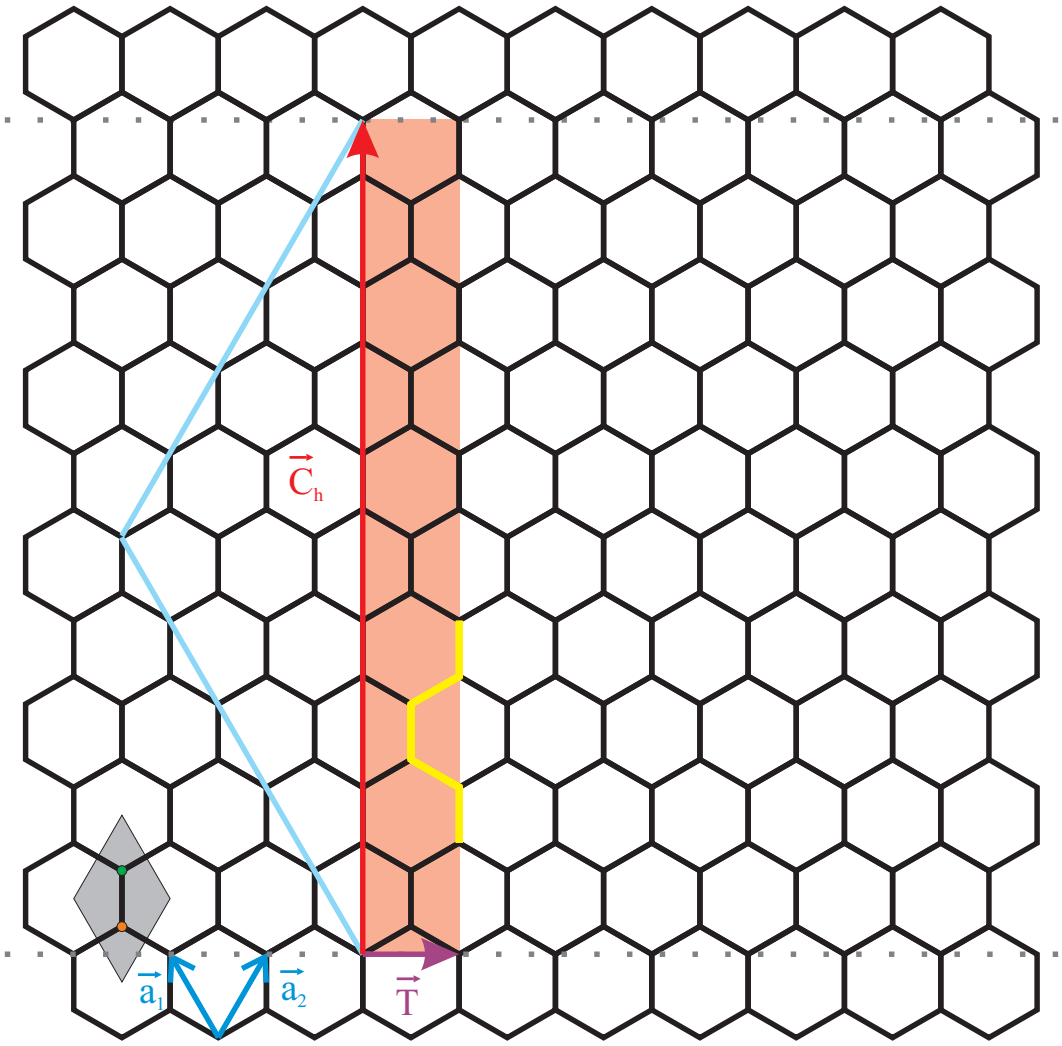

Figure 2.5: A graphene sheet, lattice vectors $\vec{a_1}$ and $\vec{a_2}$ in blue and unit cell shaded in grey. The red vector $\vec{C_h}$ describes how to roll up the graphene into a specific nanotube. The region between the dotted lines is rolled into a cylinder (the resulting tube shown in figure 2.6). The purple vector $\vec{T}$ is perpendicular to $\vec{C_h}$ and describes unit cell of the nanotube (shaded in peach). $\vec{C_h} = 5\vec{a_1} + 5\vec{a_2}$, giving a (5,5) nanotube. Nanotubes with chiral vectors (n, n) are called armchair tubes because of the pattern (shown in yellow) around their circumference.

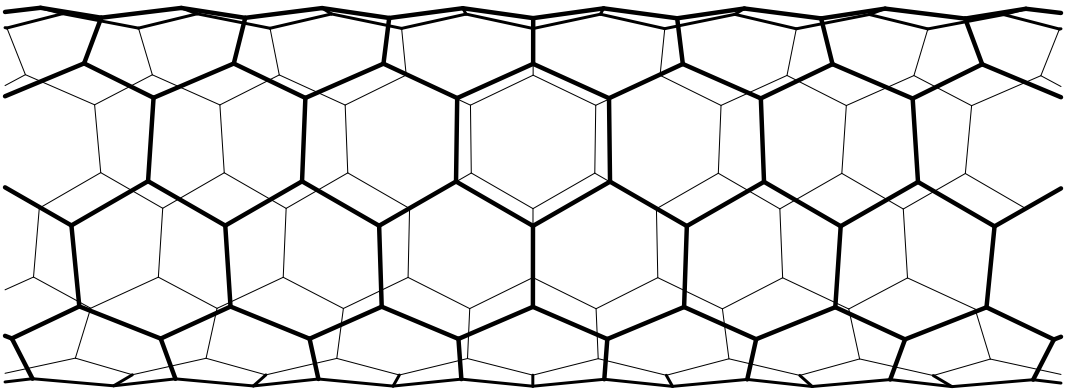

Figure 2.6: The (5,5) carbon nanotube created by rolling up a graphene sheet around the $5\overrightarrow{a_1} + 5\overrightarrow{a_2}$ vector shown in figure 2.5. This is an armchair nanotube.

with a chiral vector of $(n, 0)$ give a tube with a zigzag structure around the circumference. All nanotubes are either zigzag $(n, 0)$, armchair (n, n), or chiral.

Section 2.2 will discuss how the tube's chirality determines the electrical properties of the tube. In all the different chiral cases though, the honeycomb lattice closes in on itself. This means the walls of the tube are a closed lattice, with bonds of sp^2 hybridization. This strong carbon bond and defect-free lattice provides a resilient structure. The π bonds in the structure provide for delocalized electrons that make conduction possible. Some bonding energy is lost by bending the planar π bonds into a cylinder, as the overlap between orbitals decreases. This puts a lower limit of 0.7 nm diameter for stable isolated carbon nanotubes[102].[1] From the energy perspective there's no upper limit to the diameter of a carbon tube. However, if the tube is larger than 2 nm in diameter, it becomes likely (for our growth mechanisms) that the tube is composed of more

[1]The short width of a graphene hex is 0.256 nm. A 0.7 nm diameter tube is thus more than eight carbon hexes around. All the example tubes shown are too small to be stable single-walled nanotubes, but illustrate the principles involved.

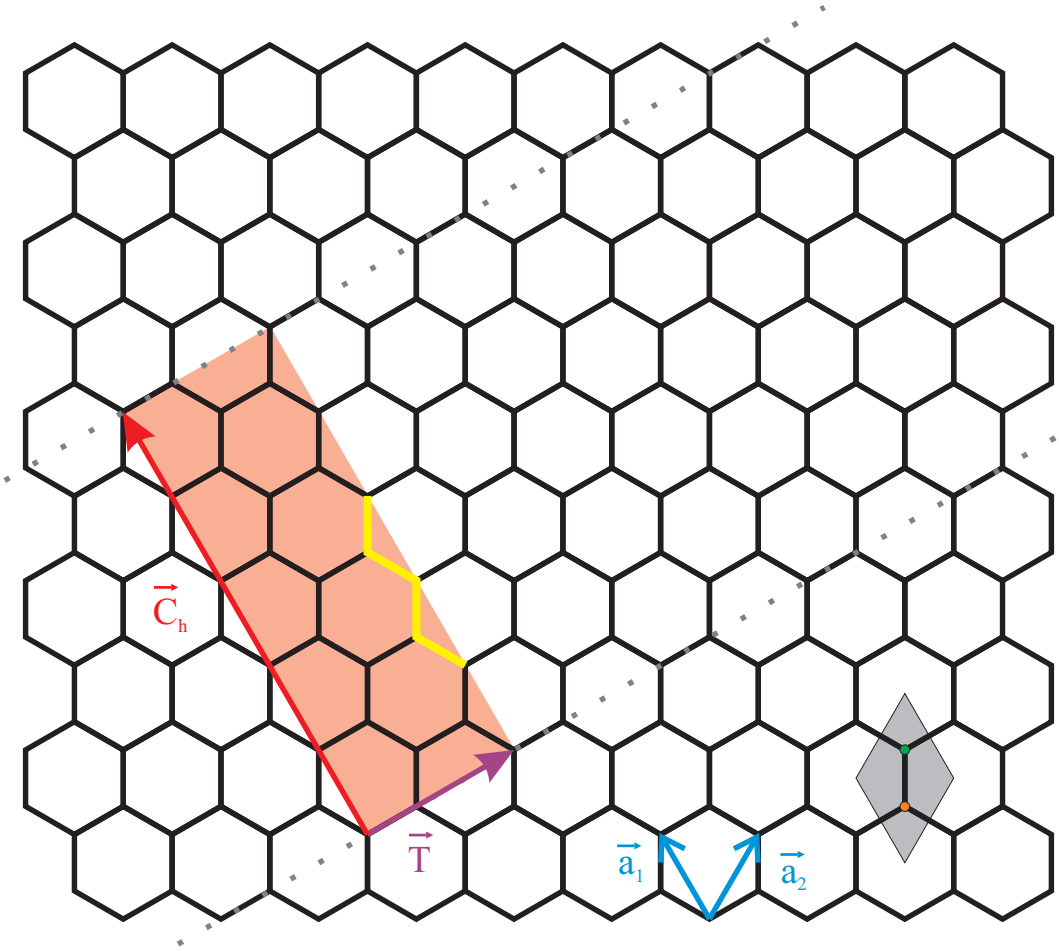

Figure 2.7: A graphene sheet, lattice vectors $\vec{a_1}$ and $\vec{a_2}$ in blue and unit cell shaded in grey. The red vector $\vec{C_h}$ describes how to roll up the graphene into a specific nanotube. The region between the dotted grey lines is rolled into a cylinder (the resulting tube shown in figure 2.8). The purple vector $\vec{T}$ is perpendicular to $\vec{C_h}$ and describes unit cell of the nanotube (shaded in peach). $\vec{C_h} = 5\vec{a_1} + 0\vec{a_2}$, giving a (5,0) nanotube. Chiral vectors $(n, 0)$ give a zigzag nanotube, so named because of the zigzag pattern around the circumference (shown in yellow).

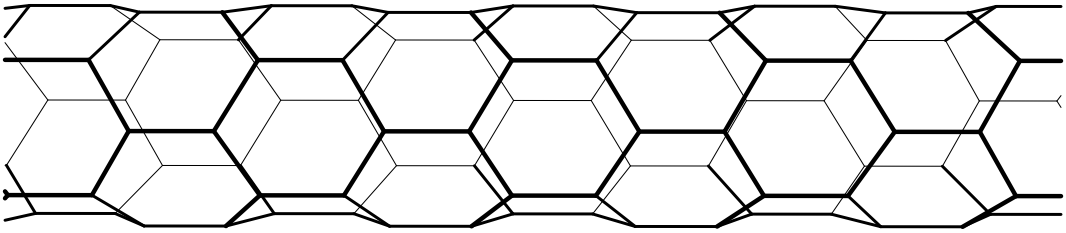

Figure 2.8: The (5,0) carbon nanotube created by rolling up a graphene sheet around the $5\overrightarrow{a_1} + 0\overrightarrow{a_2}$ vector shown in figure 2.7. This is a zigzag nanotube.

than one concentric tube in a multi-wall tube. Large-diameter single-walled nanotubes would also not retain the shape of a cylinder; they would collapse into two parallel sheets joined by small half-tubes along two edges.

There is no theoretical limit to the length of a carbon nanotube. The current record for length of individual tube is on the order of centimeters [145], giving an aspect ratio of seven orders of magnitude. For our experiments, tubes micrometers in length are sufficient. We use the three orders of magnitude aspect ratio to have a nanometer scale feature that can easily be contacted and interacted with along its length (described in section 3.4). Because we'll be covering the ends of our nanotubes with electrical contacts, the capping of the nanotube is not particularly relevant to our experiments. Nanotubes can be open on the end, or capped with a dome of carbon atoms in hexagons and pentagons (the pentagons both being more strained and contracting the curvature).

Although we've conceptually described them as rolled up sheets, carbon nanotubes aren't formed by taking layers of graphene and rolling them up. They're grown from carbon feedstock at high temperatures in a variety of ways

[102]. Our particular method for growing and contacting nanotubes will be discussed in chapter 3, but first we discuss the electronic properties that make these tubes so useful.

2.2 Electronic structure of carbon nanotubes

The electronic structure of a carbon nanotube is that of graphene modified by the tube's structure and reduced dimensionality. We briefly sketch why graphene is a zero-bandgap semiconductor [102], and then show how the nanotube's band structure is extracted from graphene's. Once we've extracted the band structure of the nanotube, we'll show how its chirality determines whether the tube is metallic or a semiconductor. We'll then determine the bandgap for the semiconducting nanotubes, and then the density of states.

2.2.1 The reciprocal lattice for graphene

As discussed in section 2.1, the sp^2 hybridization of carbon atoms results in a planar arrangement of carbon atoms with three bonding directions with 120° between them. Figure 2.9a shows a section of graphene. The unit cell is shaded in grey, and the two inequivalent carbon atoms sites are marked with green and orange.

We want to look at the reciprocal lattice of graphene because it will give us information about the momentum states, $\vec{k}$, available to electrons in the graphene. Figure 2.9b shows the reciprocal lattice of graphene. The first Brillouin zone, the unit cell of the reciprocal lattice, is shaded in grey. The reciprocal

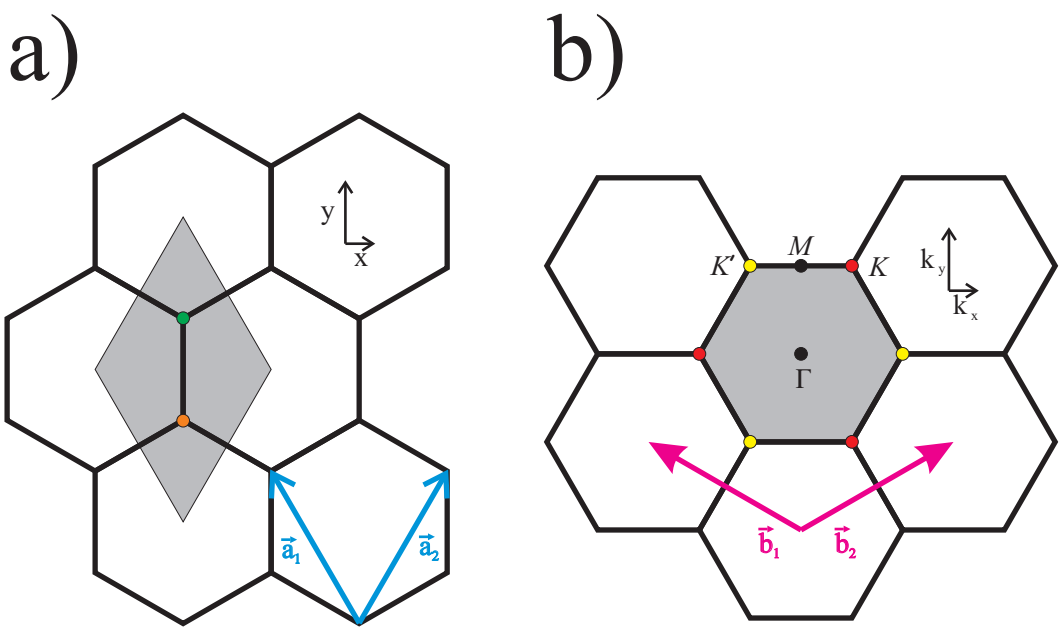

Figure 2.9: a) Section of a graphene lattice. The unit cell is shaded in grey. The two inequivalent lattice points are shown with orange and green circles. The lattice vectors are shown in blue. b) Section of the reciprocal lattice. The first Brillouin zone is shaded in grey. Points of high symmetry are labeled. The reciprocal lattice vectors are shown in magenta.

lattice vectors are:

$$\vec{b_1} = -\frac{2\pi}{a}\hat{k_x} + \frac{2\pi}{a\sqrt{3}}\hat{k_y}, \tag{2.11}$$

$$\vec{b_2} = +\frac{2\pi}{a}\hat{k_x} + \frac{2\pi}{a\sqrt{3}}\hat{k_y}. \tag{2.12}$$

We've used $a_{mp}b_{np} = 2\pi\delta_{mn}$, [2] which gives a reciprocal lattice constant of $\frac{4\pi}{a\sqrt{3}}$ and the relations:

$$\vec{b_1}\cdot\vec{b_1} = \vec{b_2}\cdot\vec{b_2} = \frac{4}{3}\left(\frac{2\pi}{a}\right)^2, \tag{2.13}$$

$$\vec{b_1}\cdot\vec{b_2} = -\frac{2}{3}\left(\frac{2\pi}{a}\right)^2. \tag{2.14}$$

[2] Here we are summing over the shared index p and δ_{mn} is the Kronecker delta: $\delta_{11} = \delta_{22} = 1$; $\delta_{12} = \delta_{21} = 0$.

Some of the points of high symmetry in k space are labeled in figure 2.9b. Γ is where $\overrightarrow{k} = 0$. M is at the midpoint of a boundary segment of the Brillouin zone, for instance $\overrightarrow{k} = \frac{2\pi}{a\sqrt{3}}\hat{k_y}$. Of particular interest are the vertices of the Brillouin zone, called the Dirac points, marked with red and yellow in figure 2.9. There are three red points, and three yellow points. The red points are all equivalent to each other, as they are linked by reciprocal lattice vectors. By the same logic, the yellow points are all also equivalent. These points, labeled K and K', are where $|\overrightarrow{k}|$ is maximum at $\frac{4\pi}{3a}$ and, as we'll show, are special points in the band structure of graphene.

We now know the extent of $\overrightarrow{k}$ for the electrons in a graphene sheet. We want to use this information in conjunction with the band structure of graphene to determine what the density of states looks like. The high symmetry of graphene makes it straightforward to carry out a tight binding calculation for the system. Reference [63] does a good job detailing the steps, which won't be repeated here; for more elaborate versions see [128],[103], and [38]. We focus instead on the results for the valence and conduction band most relevant for carrying current. Figure 2.10 shows the energy dispersion of graphene around the Fermi energy in the first Brillouin zone. The surface shows the allowed energy values for different $\overrightarrow{k}$s. The upper conduction band touches the lower valence band at the K and K' points shown in figure 2.9. The six points of contact between the bands are the two Dirac points (each point is only $\frac{1}{3}$ in the zone, and $6 * \frac{1}{3} = 2$).[3] The sp^2 hybridization leaves one electron per atom, or two per unit cell. These two electrons exactly fill the valence band of the graphene, making graphene a zero band-gap semiconductor. The dispersion relation, from the tight binding

[3]The other way to think about it is as discussed previously: because four of the points are linked by reciprocal lattice vectors to the other two, they're degenerate points.

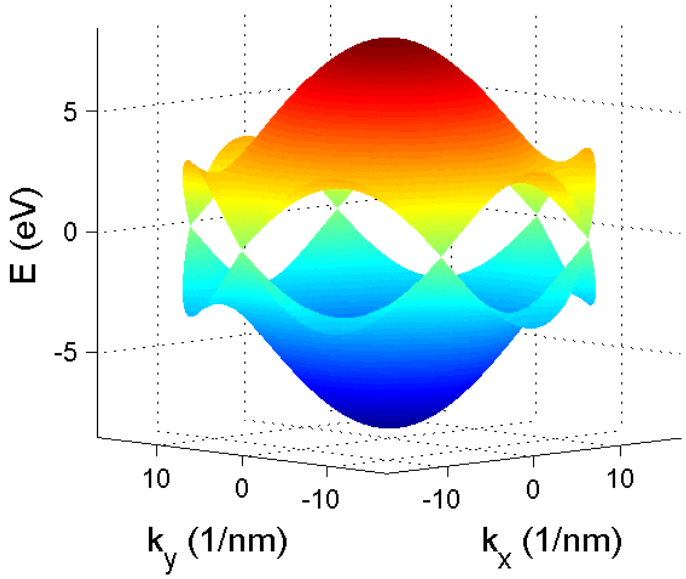

Figure 2.10: Band structure of graphene, plotted for $|\vec{k}| < \frac{4\pi}{3a}$, which slightly exceeds the first Brillouin zone. The vertical axis is energy in eV, and the horizontal axes are $\vec{k_x}$ and $\vec{k_y}$ in (1/nm). The valence band is shown in blue, and the conduction band is shown in red. The two bands touch at the K and K' Dirac points.

calculation [102], is

$$E_{g\,2D}(k_x, k_y) = \pm t \sqrt{1 + 4\cos\left(\frac{k_x a}{2}\right)\cos\left(\frac{k_y a\sqrt{3}}{2}\right) + 4\cos^2\left(\frac{k_x a}{2}\right)}. \tag{2.15}$$

The parameter t here comes from the transfer integral between the carbon atoms, and has a value of $t = -2.7eV$ [100]. We can see that at Γ, where $\vec{k} = 0$, the two bands are separated by $6t$. At the M points, such as $\vec{k} = \frac{2\pi}{a\sqrt{3}}\hat{k_y}$, the bands are separated by $2t$. The $\vec{k}$ of one of the K points is $\vec{\Gamma K} = \frac{1}{3}(2\vec{b_1} + \vec{b_2}) = (-\frac{2\pi}{3a}\hat{k_x} + \frac{2\pi}{a\sqrt{3}}\hat{k_y})$. Plugging this in equation 2.15 to confirm gives $E_{g\,2D}\left(-\frac{2\pi}{3a}, \frac{2\pi}{a\sqrt{3}}\right) =$

$\pm t\sqrt{1 + 4\cos(-\frac{\pi}{3})\cos(\pi) + 4\cos^2(-\frac{\pi}{3})} = 0$. So at the K and K' points, the two bands touch.

The fact that the valence and conduction band meet for graphene makes it a zero-bandgap semiconductor. At any electron energy level (inside the $6t$ region we're dealing with), there are available $\overrightarrow{k}$ states for the electrons to be in. That means that when a bias is applied across graphene, there are available states for electrons to transition to such that the electrons have net momentum through the system and can carry a current. Graphene is thus a zero-bandgap conductor, but going from two dimensional flat graphene to a rolled carbon nanotube can change that.

2.2.2 The Brillouin zone for carbon nanotubes

Taking a segment of two-dimensional graphene and rolling the sheet into a cylinder (à la section 2.1) results in additional quantization to the graphene band structure. The phase accumulated for an electron going around the circumference of the the nanotube must be an integer multiple of 2π. The directionality of the nanotube gives us an orientation to talk about the $\overrightarrow{k}$ components: $\overrightarrow{K_\parallel}$ along the length of the tube and $\overrightarrow{K_\perp}$ around the circumference. These vectors tie back in to the chiral vector described in section 2.1. The chiral vector $\overrightarrow{C_h}$ described the circumference of the nanotube. A component aligned with $\overrightarrow{C_h}$ goes around the tube, and is thus perpendicular to the axis of the tube. We label this component $\overrightarrow{K_\perp}$. The vector $\overrightarrow{T}$ is perpendicular to $\overrightarrow{C_h}$ and describes the unit cell of the nanotube. The $\overrightarrow{k}$ component aligned with $\overrightarrow{T}$ is thus parallel to the tubes axis. We

label this component $\overrightarrow{K_\parallel}$.[4] More formally,

$$\overrightarrow{K_\perp} \cdot \overrightarrow{C_h} = 2\pi, \quad \overrightarrow{K_\perp} \cdot \overrightarrow{T} = 0, \tag{2.16}$$

$$\overrightarrow{K_\parallel} \cdot \overrightarrow{C_h} = 0, \quad \overrightarrow{K_\parallel} \cdot \overrightarrow{T} = 2\pi. \tag{2.17}$$

Using the above and $\overrightarrow{C_h} \cdot \overrightarrow{T} = 0$ establishes that $\overrightarrow{K_\perp} \cdot \overrightarrow{K_\parallel} = 0$. We can use all this to establish equations for $\overrightarrow{K_\perp}$ and $\overrightarrow{K_\parallel}$:

$$\overrightarrow{K_\perp} = \frac{1}{2}\left(\frac{a}{\pi d}\right)^2 \left((2n+m)\overrightarrow{b_1} + (2m+n)\overrightarrow{b_2}\right), \tag{2.18}$$

$$\overrightarrow{K_\parallel} = \frac{1}{N}\left(m\overrightarrow{b_1} - n\overrightarrow{b_2}\right). \tag{2.19}$$

Where we've used that the length of $\overrightarrow{C_h} = a\sqrt{n^2+m^2+nm}$ is the circumference of the nanotube, and thus πd, where d is the diameter of the tube, which makes $\left(\frac{a}{\pi d}\right)^2$ a succinct way to write $1/(n^2+m^2+nm)$. For a sense of scale, it is worth noting:

$$|\overrightarrow{K_\perp}| = \frac{2\pi}{|\overrightarrow{C_h}|} = \frac{2}{d}, \tag{2.20}$$

$$|\overrightarrow{K_\parallel}| = \frac{2\pi}{|\overrightarrow{T}|} = \frac{2F}{d\sqrt{3}}. \tag{2.21}$$

We can now talk about the $\overrightarrow{k}$ of the electron in terms of its $\overrightarrow{K_\perp}$ and $\overrightarrow{K_\parallel}$ components. For a $\overrightarrow{k} = A\overrightarrow{K_\perp} + B\overrightarrow{K_\parallel}$, we know A must be an integer because the wavefunction of the electron around the tube must be a multiple of 2π and $\overrightarrow{K_\perp} \cdot \overrightarrow{C_h} = 2\pi$. Each of these integer values of A will have a one-dimensional Brillouin zone of length $|\overrightarrow{K_\parallel}|$ in the direction specified by $\overrightarrow{K_\parallel}$ (the same direction as $\overrightarrow{T}$). These zones are shown for an example $\overrightarrow{C_h} = 4\overrightarrow{a_1} + 2\overrightarrow{a_2}$ tube in figure 2.11. The first Brillouin zone of graphene is shaded in grey, and the graphene reciprocal lattice vectors are shown in magenta. The $\overrightarrow{K_\perp}$ and $\overrightarrow{K_\parallel}$ vectors are shown in black. The differ-

[4] The finite length of a nanotube introduces quantization effects into $\overrightarrow{K_\parallel}$ as well. However, the length of the tube is orders of magnitude larger than diameter, thus the spacing in $\overrightarrow{K_\parallel}$ is much much smaller. This thesis will not involve tubes of such short length or low enough temperatures for $\overrightarrow{K_\parallel}$ quantization to be noticeable.

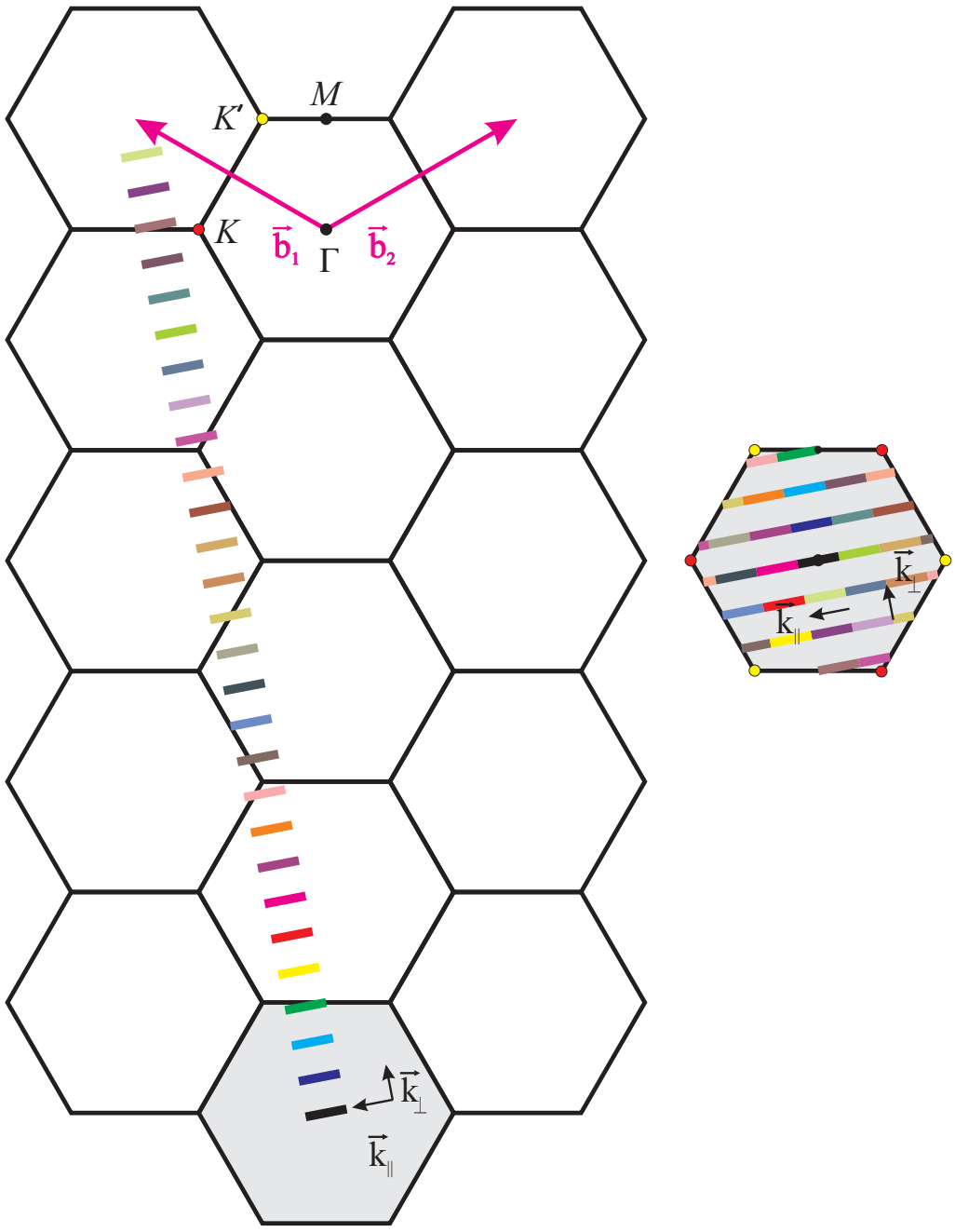

Figure 2.11: The allowable $\vec{k}$ states for a $\vec{C_h} = 4\vec{a_1}+2\vec{a_2}$ nanotube. $\vec{K_\parallel}$ and $\vec{K_\perp}$ are shown in black. The reciprocal lattice vectors are shown in magenta. The first Brillouin zone for graphene is shaded in grey. On the left are the N=28 1D Brillouin zones of length $|\vec{K_\parallel}|$ spaced by $\vec{K_\perp}$, shown in different colors. On the right, the 1D Brillouin zones have been translated into the first Brillouin zone of graphene with integer multiples of the reciprocal lattice vectors.

ent allowable 1D zones are the colored lines with the same orientation as $\overrightarrow{K_{\parallel}}$, spaced by $\overrightarrow{K_{\perp}}$. When $A_i * \frac{1}{2}\left(\frac{a}{\pi d}\right)^2 = A_i * \frac{1}{2(n^2+m^2+nm)}$ is an integer, then $A_i * \overrightarrow{K_{\perp}}$ will be a sum of integer multiples of the reciprocal lattice vectors. That overlaps the A_i 1D Brillouin zone with the $A = 0$ Brillouin zone.[5] Figure 2.11 shows the non-overlapping 1D Brillouin zones. There are N 1D Brillouin zones before the allowed $\overrightarrow{k}$ overlap, where N is again the number of hexes in the nanotube unit cell. Each hex contributes one 1D Brillouin zone to construct the allowed $\overrightarrow{k}$ of the nanotube.

The N 1D Brillouin zones can be translated into the Brillouin zone of graphene with the reciprocal lattice vectors with a particularly neat result, shown in the right side of figure 2.11. The N 1D Brillouin zones form lines that cut through the Brillouin zone of the graphene. These lines are the allowable $\overrightarrow{k}$ states for electrons in the nanotube. The achievable energies for the electrons in the nanotube are thus the energies from the graphene band structure, subject to the constraint of the allowed $\overrightarrow{k}$ states.[6] Graphically, each of the lines in the Brillouin zone in figure 2.11 represents planes perpendicular to the page. The intersection of those planes and the band structure shown in figure 2.10 is the band structure for the nanotube. There is a lot of information in that intersection, so we'll deal with it in pieces. The next section will look at the structure of the intersection as a tool to distinguish two classes of nanotubes with different electrical properties. We'll then go more in depth into the two different types of tubes, again using their band structure.

[5] If $(2n + m)$ and $(2m + n)$ have a common factor, $A * \overrightarrow{K_{\perp}}$ will hit a sum of integer multiples of the reciprocal lattice vectors before A_i, in which case the 1D Brillouin zones simply overlap and repeat faster.

[6] While this has been illustrated instead of exhaustively shown, the assembly of 1D Brillouin zones into lines cutting the Brillouin zone of the graphene is a general result for all tubes. For a more group theory based proof, see [102].

2.2.3 Determining metallic versus semiconducting nanotubes from their chirality

A nanotube is either a semiconductor or a metallic tube based on how its allowed $\overrightarrow{k}$ states interact with the band structure of graphene. If the quantized $\overrightarrow{K_\perp}$ values result in the allowed $\overrightarrow{k}$ missing the K and K' points (as is the case in figure 2.11), then there is a range of energies that is inaccessible to the electrons in the nanotube. This creates a semiconducting nanotube with a bandgap. If the allowed $\overrightarrow{k}$ states intersect the K and K' points, then there are available energy levels from the conduction band to the valence band. This lack of bandgap results in a metallic nanotube.

We'll now look more closely at the allowed $\overrightarrow{k}$ to determine when they intersect the K and K' points. Figure 2.12 shows the simplified Brillouin zone from figure 2.11. The K points are labeled in red, and the K' points in yellow. New points Y and Y' have been added and labeled in dark and light blue. Y is the point where a line perpendicular to the $\overrightarrow{K_\perp}$ intersects a K point, and similarly for Y' and K'. For the lines of allowed $\overrightarrow{k}$ to intersect a K or K' point, the distance YK has to be an integer multiple of $|\overrightarrow{K_\perp}|$. YK is the component of ΓK in the $\overrightarrow{K_\perp}$ direction:

$$YK = \overrightarrow{\Gamma K} \cdot \frac{\overrightarrow{K_\perp}}{|\overrightarrow{K_\perp}|} \tag{2.22}$$

Each K point has a corresponding K' point with the opposite coordinates, so YK=$Y'K'$. We'll look at the K' point $\frac{1}{3}(2\overrightarrow{b_1} + \overrightarrow{b_2})$, and using equations 2.18, 2.13, and 2.14:

$$YK = \overrightarrow{\Gamma K'} \cdot \frac{\overrightarrow{K_\perp}}{|\overrightarrow{K_\perp}|} = \frac{d}{NF}\left(\frac{2\pi}{a}\right)^2 \frac{2n+m}{3} = \frac{2}{d}\frac{2n+m}{3} = |\overrightarrow{K_\perp}|\frac{2n+m}{3}. \tag{2.23}$$

Thus YK is an integer multiple of $|\overrightarrow{K_\perp}|$ when $2n+m$ is divisible by three. If $2n+m$

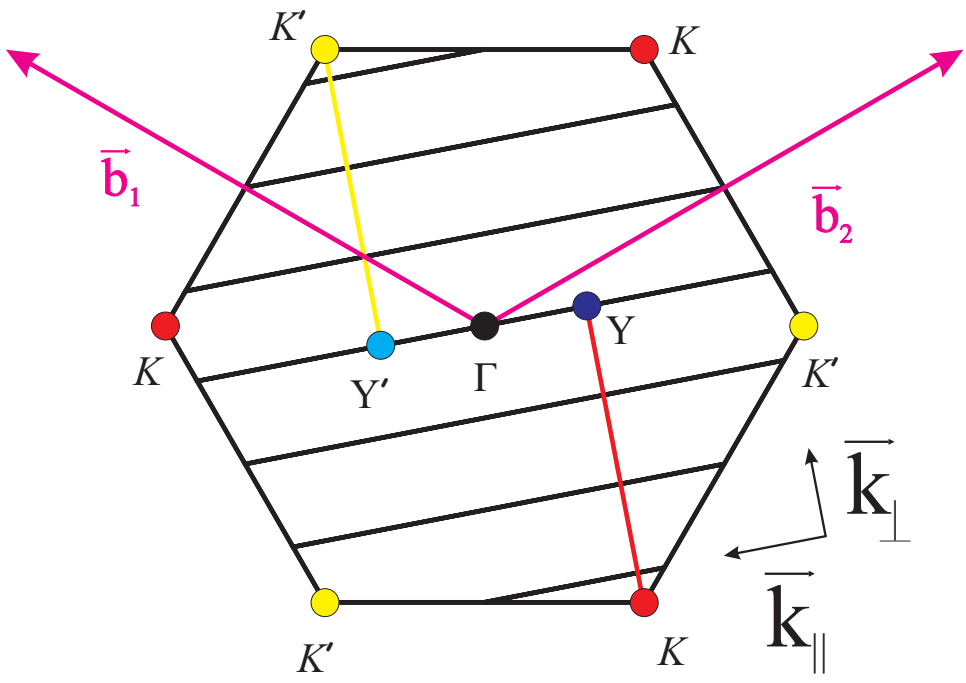

Figure 2.12: The Brillouin zone from figure 2.11 with K points labeled in red and K' points in yellow. New points Y and Y' are added and labeled in dark and light blue. The reciprocal lattice vectors are their usual magenta.

is divisible by three, then $2n + m - 3m$ is divisible by three (since $3m$ is divisible by three, and a multiple of three minus a multiple of three is divisible by three). If $2n + m - 3m = 2n - 2m$ is divisibly by three, then $n - m$ is divisible by three because dividing $2n - 2m$ by a factor of two can't change if it's a multiple of three. Equation 2.23's simple result can be phrased as: if $n - m$ is a multiple of three, then $\vec{k}$ intersects the K and K' points.

We care about this because $\vec{k}$ intersecting the Dirac points means there is no bandgap. If $\vec{k}$ missed the K and K' points, then there are no allowed $\vec{k}$ states with energy equal to zero. That energy gap means the tube is a semiconductor, whereas if there is not a gap, the tube is metallic. This straightforward result, if n-m is a multiple of three, then the tube is metallic, gives a first order classifica-

tion for all carbon nanotubes [85] [132].

Although we showed equation 2.23 for only one of the K K' pairs, the others are equivalent through reciprocal lattice translations, so if $n - m$ is not divisible by three, $\overrightarrow{k}$ misses the K and K' points and the tube has a semiconducting bandgap. Because YK is $|\overrightarrow{K_\perp}|\frac{2n+m}{3}$, if $\overrightarrow{k}$ misses the K and K' points, it misses them by $\pm\frac{1}{3}\overrightarrow{K_\perp}$ and $\pm\frac{2}{3}\overrightarrow{K_\perp}$. This is a general result for semiconducting nanotubes [104]. The result of the allowed $\overrightarrow{k}$ missing the Dirac points is a bandgap for semiconducting tubes, which we explore in the next section.

In our experiments, metallic nanotubes often have bandgaps from defects or interactions with the substrate. These tubes are used as semiconducting tubes with small bandgaps. It's worth noting that strain in the tube [78] [137] and magnetic fields [18] [2] [47] can create bandgaps in metallic tubes. More intricate theoretical work predicts that for very small nanotubes, curvature in the tube itself can create bandgaps [38] [54]. Recent experimental work has shown that most metallic nanotubes have a bandgap of 10 to 100 meV [24], which is below the energy resolution of our experiments. The next section's quantitative analysis of the bandgap in semiconducting tubes will also give us qualitative insight into relevant gaps in metallic tubes.

2.2.4 The bandgap of semiconducting nanotubes

If the K points of the Brillouin zone are not intersected by the allowed $\overrightarrow{k}$ of the nanotube, the tube will have a bandgap. We can determine the size of the gap for a semiconducting tube where $n - m$ is not divisible by three. We'll use the structure of graphene's bands, and the geometric results from section 2.2.3.

Referring back to equation 2.15, the slope of the band structure in any direction near the K points is:

$$\left.\frac{dE}{d\overrightarrow{k}}\right|_{\overrightarrow{k}=\overrightarrow{\Gamma K}} = \pm\frac{ta\sqrt{3}}{2}. \tag{2.24}$$

Getting this slope is a tricky, but interesting, mathematical process, so we'll step through it here. For simplicity, we'll calculate the slope along the line $k_x = \frac{4\pi}{3a}$ which intersects the right K' point. The slope of $E_{g\,2D}(k_x, k_y)$ around the K and K' Dirac points is independent of direction[7], so we'll choose this simple case for clarity. Using equation 2.15 and $k_x = \frac{4\pi}{3a}$ gives:

$$E_{g\,2D}(\tfrac{4\pi}{3a}, k_y) = \pm t\sqrt{2 - 2\cos\left(\tfrac{k_y a\sqrt{3}}{2}\right)}. \tag{2.25}$$

Taking a derivative with respect to $\overrightarrow{k_y}$,

$$\left.\frac{\partial E_{g\,2D}}{\partial k_y}\right|_{k_x=\frac{4\pi}{3a}} = \pm\frac{ta\sqrt{3}}{2}\frac{\sin\left(\frac{k_y a\sqrt{3}}{2}\right)}{\sqrt{2 - 2\cos\left(\frac{k_y a\sqrt{3}}{2}\right)}}, \tag{2.26}$$

and evaluating at the K' point $k_x = \frac{4\pi}{3a}$, $k_y = 0$ gives $\pm\frac{ta\sqrt{3}}{2}\frac{0}{0}$, which is undefined. We get to use L'Hospital's Rule, which states that if a numerator and denominator of a fraction go to zero, the ratio is the ratio of the derivatives; i.e.:

$$\text{if} \quad \lim_{x\to x_\circ}\frac{F(x_\circ)}{G(x_\circ)} = \frac{0}{0} \quad \text{then} \quad \lim_{x\to x_\circ}\frac{F(x_\circ)}{G(x_\circ)} = \frac{F'(x_\circ)}{G'(x_\circ)}. \tag{2.27}$$

We want to take the derivative of the numerator and denominator of equation 2.26 with respect to k_y (not just the derivative with respect to k_y, but of the top and bottom separately). The denominator of 2.26 is $E_{g\,2D}/(\pm t)$, which gives:

$$\lim_{k_y\to 0}\frac{\partial E_{g\,2D}}{\partial k_y} = \frac{\frac{ta\sqrt{3}}{2}\sin\left(\frac{k_y a\sqrt{3}}{2}\right)}{\frac{E_{g\,2D}}{t}} = \frac{\frac{3t^2a^2}{4}\cos\left(\frac{k_y a\sqrt{3}}{2}\right)}{\frac{\partial E_{g\,2D}}{\partial k_y}}. \tag{2.28}$$

[7]We show in the $\overrightarrow{k_y}$ direction here. The $\overrightarrow{k_x}$ is similar, but with slightly more algebra. The arbitrary $\overrightarrow{k}$ is similar, but with a lot more algebra.

It may look like things are getting worse, be we can regroup,

$$\lim_{k_y \to 0} \left(\frac{\partial E_{g\,2D}}{\partial k_y} \right)^2 = \frac{3t^2a^2}{4} \cos\left(\frac{k_y a\sqrt{3}}{2} \right), \tag{2.29}$$

take the square root, and now plug in $k_y = 0$, which gives

$$\lim_{k_y \to 0} \left. \frac{\partial E_{g\,2D}}{\partial k_y} \right|_{k_x = \frac{4\pi}{3a}} = \pm \frac{ta\sqrt{3}}{2}. \tag{2.30}$$

This was the result stated a page ago in equation 2.24, but now we've seen where it comes from and are ready to put it to use.

For energies near zero, the band structure of graphene can be described as pairs of cones touching tip to tip at the K points. Figure 2.13 shows these cones and their intersection with the allowed $\overrightarrow{k}$. On the right are the allowed $\overrightarrow{k}$ passing through the Brillouin zone. On the left are the touching cones at the Dirac points, and the intersection of the allowed $\overrightarrow{k}$ with those cones.

We know that allowed $\overrightarrow{k}$ of a semiconducting nanotube misses the K points by $\pm\frac{1}{3}\overrightarrow{K_\perp}$ and $\pm\frac{2}{3}\overrightarrow{K_\perp}$. The magnitude of $\overrightarrow{K_\perp}$ is $\frac{2}{d}$. If $\overrightarrow{k}$ missed the K point of $E = 0$ by $\pm\frac{1}{3}\frac{2}{d}$, and the slope of $E(\overrightarrow{k})$ is $\frac{ta\sqrt{3}}{2}$, then the gap between the highest energy states in the valence band and the lowest energy states in the conduction band is

$$E_{gap} = 2 * \frac{ta\sqrt{3}}{2} * \frac{1}{3}\frac{2}{d} = \frac{2ta}{d\sqrt{3}} = \frac{2ta_{C-C}}{d}. \tag{2.31}$$

Where t is the overlap integral from the tight binding calculation and has a value of $t \approx -2.7eV$, $a = 0.249$ nm is the lattice constant of graphene, ($a_{C-C} = 0.144$ nm is the nearest neighbor carbon-carbon distance in graphene,) and d is the diameter of the tube. The incredible thing about this is that the bandgap of a semiconducting nanotube depends only on the diameter of the tube:

$$E_{gap} = \frac{0.78eV}{d[\text{in nm}]}. \tag{2.32}$$

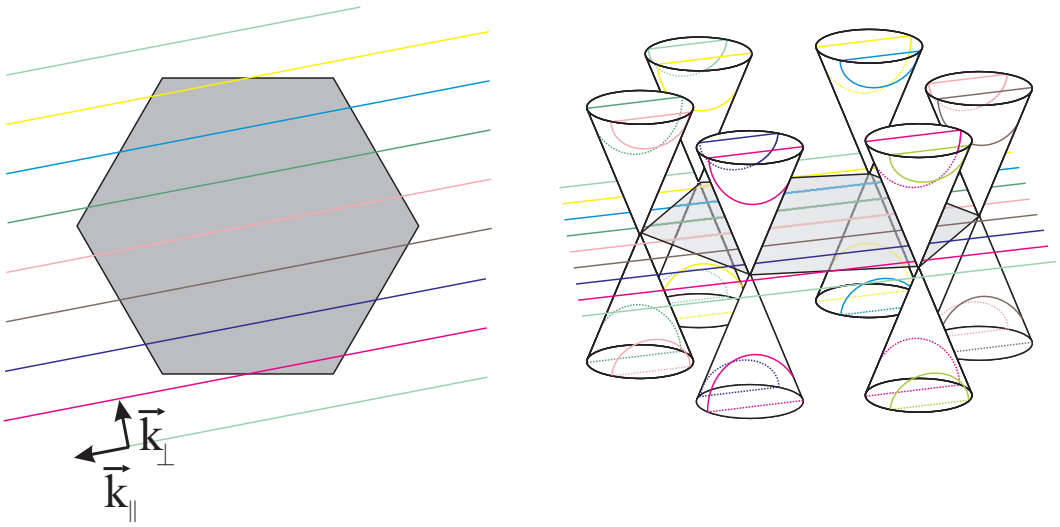

Figure 2.13: Schematic of allowed k-states intersecting graphene's band structure. On the left, the allowed $\vec{k}$ states cutting through the first Brillouin zone. On the right, the intersection of these allowed $\vec{k}$ states with the band structure of graphene, which near the Fermi energy can be approximated by cones touching at the Dirac points.

This was predicted [102] and has been experimentally established [132]. The larger the diameter of a semiconducting tube, the smaller the bandgap. The smallest stable tubes have bandgaps around an eV. The opportunity to custom-design bandgaps of a semiconducting wire is one of the many exciting possibilities of carbon nanotubes. Having established the band structure of the tube, we look at this structure's implications for the effective mass of electrons in the tube, the Fermi velocity, and then use the band structure to determine the tube's density of states.

2.2.5 Fermi velocity and effective mass in a carbon nanotube

The band structure of carbon nanotubes results in interesting effective masses for the electrons in the tube. The velocity of the carriers in the band is related to the first derivative of the band [108]:

$$v = \frac{1}{\hbar}\frac{\partial E}{\partial k}. \tag{2.33}$$

The effective mass, m_{eff}, of an electron in a semiconductor is given by the curvature of band [108]:

$$m_{eff} = \frac{\hbar^2}{\partial^2 E/\partial k^2}. \tag{2.34}$$

We showed in the previous section that for metallic nanotubes the band structure near the Fermi energy is two intersecting lines. The curvature of the band is thus the derivative of a constant slope, which is zero. The electrons and holes in the valence and conduction bands of a metallic nanotube thus have an effective mass of zero. Many theorists thus find nanotubes (and graphene) an interesting system to consider massless Dirac fermions[83] with an effective "speed of light" of the velocity of the carriers in the band:

$$v_F = \frac{1}{\hbar}\frac{\partial E}{\partial k} = \frac{1}{\hbar}\frac{ta\sqrt{3}}{2} \cong 8.8 * 10^5 m/s. \tag{2.35}$$

This is the group velocity for electrons and holes in metallic nanotubes near the Dirac point, and is called the Fermi velocity.

For semiconducting nanotubes, the valence and conduction band form a hyperbola (shown in figure 2.13). The generic equation of a hyperbola is

$$\frac{y^2}{A^2} - \frac{x^2}{B^2} = 1. \tag{2.36}$$

We want a hyperbola in E where the intercept at $K_{\|} = 0$ is half the bandgap, so $A = \frac{ta}{dsqrt3}$. The asymptotes of a hyperbola have slope $\pm\frac{A}{B}$, which has to be equal

to the slope of the cone calculated in equation 2.30. B is thus $\frac{2}{3d}$. This gives the equation of our hyperbola in E and $K_{\parallel}$ as

$$\frac{E^2}{(\frac{ta}{d\sqrt{3}})^2} - \frac{K_{\parallel}^2}{(\frac{2}{3d})^2}. \tag{2.37}$$

The curvature of a hyperbola at its minimum is $\frac{A}{B^2}$, which we use with equation 2.34 to give

$$m_{eff,\ sc} = \frac{4\hbar^2}{tad3\sqrt{3}}. \tag{2.38}$$

The velocity of the electrons and holes at the edge of the band in a semiconducting tube is zero, because the extremum in the energy gives $\frac{\partial E}{\partial K_{\parallel}} = 0$. Away from the Dirac points, the velocity quickly approaches the limit of v_F in equation 2.35.

An analysis of the band structure has thus allowed us to write expressions for the effective mass and Fermi velocity for metallic and semiconducting tubes. We now look at how the band structure determines the density of states for a carbon nanotube.

2.2.6 Density of States of a carbon nanotube

The density of states of the carbon nanotube determines electrical properties of the tube. We sketch the derivation for the density of states of metallic and semiconducting carbon nanotubes. For metallic tubes, the density of states is constant near the Fermi energy. For semiconducting tubes, the density of states is zero inside the bandgap, peaks to infinity at the edge of the bandgap, and then tails off.

We stated above that the available energies for a nanotube were the intersection of graphene's band structure with the allowed $\overrightarrow{k}$ states of the nanotube.

The intersection near the Dirac points looks like a plane intersecting a cone, giving a conic section of allowed states. For a metallic tube, the intersection is through the points of the cone, and the conic section is the degenerate case of two intersecting lines. For a semi-conducting tube when the allowed $\vec{k}$ states do not pass through the Dirac point, the conic section is a hyperbola.

We know the shape of available energy as a function of wave-vector, which we can use to get the density of states. If we want to know the density of states as a function of energy, we want the change in total number of available states for a change in the energy. This is the limit as the change in energy goes to zero:

$$\text{Density of states at } E = g(E) = \left| \lim_{\Delta E \to 0} \frac{\Delta \text{total states}}{\Delta E} \right|. \tag{2.39}$$

The density of states, g(E), is thus the derivative of the states with respect to energy. This can be represented as one over the derivative of the energy with respect to the states. We know the energy as a function of the state, it is the conic section intersections. The density of states is thus one over the derivative of the conic sections.

For metallic nanotubes, the allowed energies are the two intersecting lines running through the K points. The derivative of these lines is just the slope of the lines, i.e. the slope of the cones, which were calculated in equation 2.30. As there are two lines of the same magnitude slope, we'll take two times one over the slope as our density. We need another factor of two for the electron spin degeneracy, which gives the density of states (per unit length) for a metallic tube of:

$$g(E)_{metallic} = \frac{8}{ta\sqrt{3}} = \frac{4}{\hbar v_F}, \tag{2.40}$$

where v_F is the Fermi velocity from equation 2.35. It means that for a metallic nanotube there is a flat density of states near the Fermi energy. As we move

away from the Fermi energy, more states become available as the lines of allowed $\vec{k}$ intersect the graphene band structure at higher energies. These additional states will have a density structure similar to the density of states for semiconducting nanotubes, which we explain below.

For semiconducting nanotubes, the intersection of the allowed $\vec{k}$ states and the band structure of graphene near the Dirac points is not two intersecting lines, but a hyperbola. That means that the derivative of the available energy with respect to the states is not a constant, but goes as $\vec{k}_{\parallel}$ minus an offset. When that goes to zero, the density of states of a semiconducting nanotube goes to infinity.

We can see a sketch of the intersection of the allowed $\vec{k}$ states with the band structure of graphene in figure 2.13. Near the Dirac points, the band structure of graphene can be approximated as a group of cones that are linear in $\vec{k}$. On the left side of the figure, we see the lines of allowed $\vec{k}$ states cutting through the Brillouin zone. On the right side, we see how these lines intersect the band structure. These curves are the allowed $\vec{k}$ states and their corresponding energy.

If this tube were metallic, the allowed $\vec{k}$ states would intersect the Dirac points, and the upper and lower curves would meet at the Dirac point. As this is the (4,2) non-metallic tube, the allowed $\vec{k}$ states miss the Dirac points and generate hyperbolas for dispersion relations. The density of states will be one over the derivative along these hyperbolas. At the minimum E for a conduction band (and maximum E for a valence band), the derivative goes to zero and gives an infinite density of states for semiconducting tubes. We'll now step through the math in more detail.

As a reminder, the equation of two cones touching at $(0,0,0)$ with slope m is $x^2 - y^2 = \frac{z^2}{m^2}$. The slope can be seen from looking at the points $(0,0,0)$ and $(1,0,m)$, showing a rise of m for a run of 1. The cones we're interested in are (for the different K and K' points):

$$(\overrightarrow{k} - \overrightarrow{\Gamma K}) \cdot (\overrightarrow{k} - \overrightarrow{\Gamma K}) = \frac{E^2}{\frac{3t^2a^2}{4}}. \tag{2.41}$$

The constraints on $\overrightarrow{k}$ give the hyperbolas of allowed $E(\overrightarrow{k})$ as

$$(\overrightarrow{k_\parallel} - \overrightarrow{\Gamma Y}) \cdot (\overrightarrow{k_\parallel} - \overrightarrow{\Gamma Y}) - (\overrightarrow{k_\perp} - \overrightarrow{YK}) \cdot (\overrightarrow{k_\perp} - \overrightarrow{YK}) = \frac{4E^2}{3t^2a^2}, \tag{2.42}$$

where $\overrightarrow{k}$ is only allowed to be $\overrightarrow{k_\parallel} + \overrightarrow{k_\perp}$. We've shown that for a semiconducting nanotube, the allowed $\overrightarrow{k}$ miss the Dirac points by $\frac{1}{3}\frac{2}{d}$. The allowed $\overrightarrow{k}$ states thus intersect the cones with a plane $\frac{2}{3d}$ from the tip of the cone. Since we're going through all this only for the structure of the derivative, we'll ignore the offsets for the moment and look at the hyperbola closest to the Dirac point

$$\frac{4E^2}{E_{gap}^2} - k_{\parallel,\circ}^2 = 1 \tag{2.43}$$

where $k_{\parallel,\circ}$ is the $\overrightarrow{k_\parallel}$ component from the YK line. This leaves us with an equation for $E(k_{\parallel,\circ})$:

$$E(k_{\parallel,\circ}) = \frac{E_g ap}{2}\sqrt{1 + k_{\parallel,\circ}^2}, \tag{2.44}$$

giving

$$\frac{\partial E}{\partial k_{\parallel,\circ}} = \frac{E_{gap}|k_{\parallel,\circ}}{2\sqrt{1 + k_{\parallel,\circ}^2}} = \frac{|k_{\parallel,\circ}E_{gap}^2}{4E} \tag{2.45}$$

which at $k_{\parallel,\circ} = 0$ (i.e. at $\overrightarrow{k_\parallel} = \overrightarrow{\Gamma Y}$) is zero. $\frac{\partial E}{\partial k} = 0$ means that $\frac{\partial k}{\partial E}$ is infinite. That means that semiconducting nanotubes have an infinite density of states at the edge of their bandgaps. In fact, for any line of allowed $\overrightarrow{k}$ slicing through the Brillouin zone that doesn't intersect a Dirac point, there will a band of states with a gap around the Fermi energy, and then an infinite density of states at

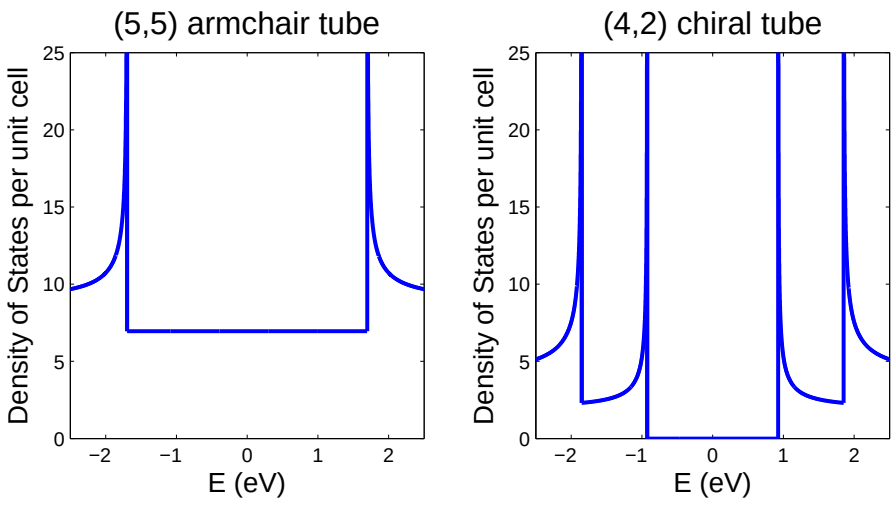

Figure 2.14: Density of states per unit cell versus energy for an armchair (5,5) nanotube on the left and a semiconducting (4,2) nanotube on the right.

the edge of the bandgap. (These bands will all have gaps around the same $\pm\vec{k}_{\|}$ values, but around different $\vec{k}_{\perp}$ values, and thus different total $\vec{k}$). Metallic nanotubes also have these additional bands for the $\vec{k}_{\perp}$ values that do not intersect the Dirac points.

Examples of densities of states for two different nanotubes are shown in figure 2.14. On the left, the density of states as a function of energy is shown for a (5,5) armchair nanotube. There is a region of constant density around the Fermi energy (E=0), corresponding to where the allowed $\vec{k}$ intersect the Dirac points. At higher energies, the $\vec{k}$ that are one $\vec{k}_{\perp}$ from the Dirac points add another set of states, and so on for the other lines of allowed $\vec{k}$ at higher energies (not shown). On the right, the density of states as a function of energy for a (4,2) chiral nanotube. There are no available states in the bandgap region around E=0. At the edge of this region, the $\vec{k}$ that missed the Dirac points by $\frac{1}{3}\vec{k}_{\perp}$ contribute a band. At higher energies the $\vec{k}$ that missed the Dirac points by $\frac{2}{3}\vec{k}_{\perp}$ contribute their

band. Other lines of allowed $\overrightarrow{k}$ would contribute more bands at higher energies (not shown). Now that we've seen the band structure of carbon nanotubes, we can take a look at making electrical elements out of carbon nanotubes.

2.2.7 Carbon nanotubes as electrical elements

We've shown that metallic carbon nanotubes have a finite density of states at all Fermi energy levels. Semiconducting nanotubes have a finite density of states outside of their band gap. When the nanotube has available states for charge carriers to pass through, the tubes can be used to create very small wires, a couple of nanometers across but microns or more long. The small width makes them functionally one-dimensional conductors, which creates interesting phenomenon[53] we'll explore and exploit.

The conductance through a 1D conductor is given by the Landauer formula [22] [7]:

$$G = \frac{e^2}{h} \sum_i T_i(E_F) \cong 39\mu S * \sum_i T_i(E_F) \cong \frac{\sum_i T_i(E_F)}{26k\Omega}, \tag{2.46}$$

where G is the conductance, $\frac{e^2}{h}$ is the quantum of conductance, and $T_i(E_F)$ is the transmission probability of the ith channel as a function of Fermi energy. A charge carrier in a nanotube has four available channels[76], giving a theoretical maximum conductance of $\frac{4e^2}{h} \approx 155\ \mu S \approx (6.5k\Omega)^{-1}$. This theoretical maximum conductance for short single-walled nanotubes has been nearly realized for metallic [59] and semiconducting [51] nanotubes. This is a realization of ballistic conduction through the nanotube for both electrons and holes, and gives a finite minimum resistance for these devices.

Away from the ballistic limit for short devices, acoustic phonons in the nan-

otube will scatter charge carriers for longer tubes[147]. In this incoherent model of conduction, the conductance of the tube goes as the ratio of the mean free path of a charge carrier, l, to the length of the device, L,[22]:

$$G = \frac{4e^2}{h}\frac{l}{L}. \tag{2.47}$$

For metallic nanotubes, mean free paths of 1.6 μm have been observed at room temperature [90] for device geometries similar to what we'll employ. For semiconducting tubes, the mean free path depends on the doping of the tube [76], and can go from zero when the tube does not conduct to hundreds of nanometers [51]. For very short mean free paths, the conductance can be modeled with the diffusive limit [22], where

$$G = en\mu. \tag{2.48}$$

Here, e is the fundamental charge, n is the number of available carriers, and μ is the mobility of those carriers. The number of available carriers will be set by the Fermi energy and the nanotube's density of states. The mobility is an intrinsic property of a material. Mobilities for carbon nanotubes have been measured of up to 10000 $\frac{cm^2}{Vs}$ for configurations similar to ours [147].

For a semiconducting nanotube to pass a current, the Fermi energy has to be moved out of the band gap of the tube. Shifting the Fermi energy such that there is a partially filled band creates available states for carriers to pass through the tube. A straightforward way of moving the Fermi energy level out of the bandgap of the nanotube is to make the nanotube the active element in a field-effect transistor ([120],[74]). A transistor is a three-terminal electrical element where the conductance between two of the terminals (the source and the drain) is controlled by the third terminal (the gate). In a field-effect transistor, the gate is capacitively coupled to whatever is conducting between the source and the

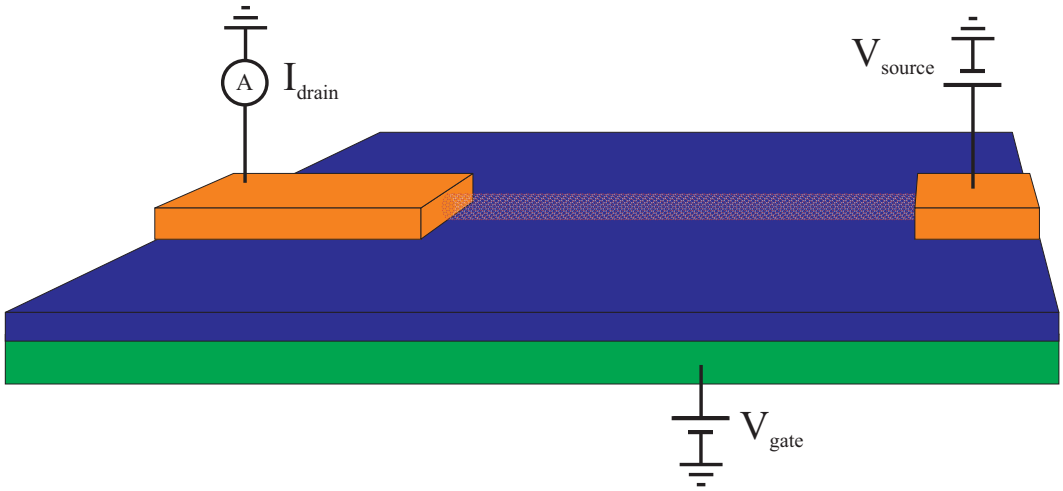

Figure 2.15: Schematic of a carbon nanotube field-effect transistor. Nanotube (red) in between two electrical contacts (orange). The contacts and nanotube are electrically isolated from, but capacitively coupled to, a conducting back gate (green) by an insulating layer (blue).

drain, and influences its conductance.[8] For a semiconducting nanotube, we attach a source and drain electrode to the tube and capacitively couple the tube to an external voltage source (referred to as the gate voltage), allowing us to shift the Fermi energy in and out of the bandgap. A side view schematic of a CNT transistor is shown in figure 2.15, where the nanotube is used as a small wire between two electrical contacts (orange). The conductance of the nanotube will be influenced by the voltage on the gate (green). The gate is isolated from, but capacitively coupled to, the tube (and contacts) through the insulating layer (blue).

[8] A simple transistor can be constructed from an electron gun, electron collector, and a voltage source. Imagine taking an electron gun that shoots out a beam of electrons. If that beam is aimed at an electron collecting target, a current is passed from the gun to the target. One can think of the gun as a source and the target as the drain of electrons. If the voltage source is placed near but not in the electron beam, the beam can continue to strike the target. As the voltage from the voltage source is increased, it can deflect the electrons as they fly past. For deflections that change the number of electrons that reach the target, the current from gun to target changes. The current, and conductance, are thus controlled by an external field.

When thinking of a semiconducting nanotube in a field effect transistor, we now have another way of looking at the number of available carriers in equation 2.48. Using the relation Q=CV, we can take the charge on the system *en* as CV. The relevant capacitance is the capacitance to the gate (per unit length), which will set the Fermi level of the nanotube. The relevant V is not the voltage on the gate, but $\Delta V = V_o - V_{gate}$. ΔV is the difference between the gate voltage V_{gate} and the voltage where there are no available carriers on the tube, V_o (the edge of the bandgap). This gives an equation for conductance of

$$G = \mu \frac{C}{L} |V_o - V_{gate}|, \tag{2.49}$$

which can be rearranged to solve for mobility:

$$\mu = \frac{G}{|V_o - V_{gate}|} \frac{L}{C}. \tag{2.50}$$

The previously mentioned mobility measurements use equation 2.50 to determine the mobility from the conductance. Doing so requires knowing the capacitance, which we will discuss measuring in chapter 4 after we discuss how to create a nanotube transistor as pictured in figure 2.15 in chapter 3. The rest of the experiments in this thesis (chapters 5 and 6) will also be based on carbon nanotube transistors.

CHAPTER 3

FABRICATION

3.1 Introduction

The experiments in this thesis all involve carbon nanotube transistors with electrical contacts, as shown in figure 2.15. This chapter will discuss the fabrication steps involved in making these electrical devices. We detail an efficient way to make electrical measurements to determine which sets of contacts are bridged by a nanotube.

Fabrication is intricately linked to the facilities and equipment available. Cornell has world-class resources in the Cornell NanoScale Science and Technology Facility (CNF), both in terms of equipment and knowledgeable staff. Courses on nanofabrication and lithography are regularly offered at the CNF. This chapter is not a stand alone substitute for learning from the CNF, but a description of what was accomplished while there.

As an end goal, figure 3.1 shows a schematic of a carbon nanotube transistor. This is the basic starting point for our experiments, and will be the end result of the fabrication steps described below. We have a carbon nanotube between two electrical contacts on top of a back gate. The electrical contacts allow us to couple external electrical signals to the carbon nanotube. The space between the contacts defines the minimum length of the tube. The back gate allows us to change the Fermi energy of the tube; which, as discussed in section 2.2.7, can affect the conductance. The nanotube grows from a catalyst pad. The pad is under one of the electrodes, and the nanotube crosses to the other electrode.

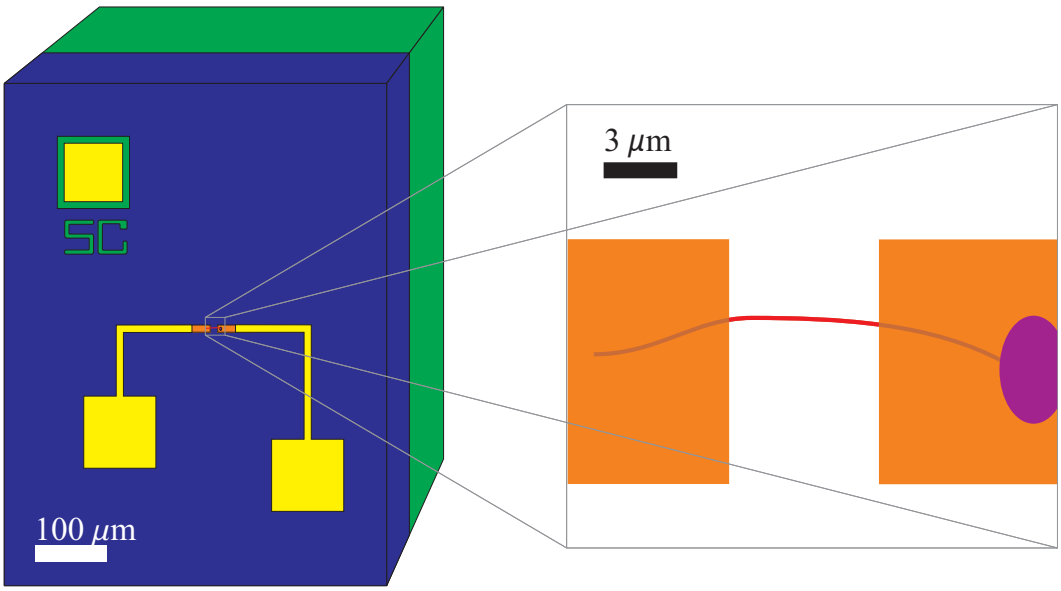

Figure 3.1: Schematic of device. Green is degenerately doped silicon back gate, also visible in back gate contact and device label. Blue is 200 nm layer of silicon dioxide. Gold is contact pads for nanotube. Orange is palladium for electrical contact to nanotube. Purple is catalyst. Nanotube shown in red. Expanded area shows a closer look at nanotube section. The distance between palladium contacts is varied to affect yield and give different lengths of nanotube.

Ideally, we want long, straight, single-walled carbon nanotubes. We want the tubes to conduct well, and have gate dependent conductance. Single-walled tubes simplify the physics in our system. Straight nanotubes allow easier and more accurate length measurements, and prevent complications from loops. Gate dependent conductance in the nanotubes is advantageous because it gives us a knob to affect the system. We want tubes with good conductance to improve signal-to-noise (easier to generate larger currents). More space between contacts requires longer tubes, but gives more room for interdigitated lithographic steps.

After growing nanotubes, we want to measure their conductance. Hundreds

of catalyst pads on a wafer are run through a furnace in a given growth. Only some of those pairs will grow nanotubes that bridge the gap between electrodes. Conductance measurements are a fast way of determining which electrode pairs have nanotubes and warrant further investigation.

The rest of the chapter will be more detailed information on the various fabrication procedures. Section 3.2 will discuss preparing the wafer for fabrication. Section 3.3 will discuss depositing catalyst and growing nanotubes. Section 3.4 details deposition of the electrodes. Section 3.5 discusses how we efficiently determine which pairs of electrodes are bridged by nanotubes. Section 3.6 describes with extra detail the fabrication of top gates used specifically in the capacitance experiment of chapter 4. Additional fabrication information pertinent to specific experiments in later chapters can be found in sections 5.3 and 6.2, with discussions of its effects on the related experiment.

3.2 Preparing the wafer

The platform of our devices is the wafer. We used degenerately doped silicon wafers with 200 nm of thermally growth silicon dioxide. These wafers can be bought with oxide, or bare doped-silicon wafers can be bought and the oxide grown in Metal Oxide Semiconductor (MOS) furnaces. After the wafer has oxide, alignment marks, back gate contact holes, and device labels were etched 700 nm into the wafer.

The purpose of the alignment marks is to give reference points for the future fabrication steps so they can be in registry with each other. The back gate contact holes allow us to access the back gate from the top of the device with probes or

wirebonds. The device labels (the 5C in figure 3.1) allow for easy distinction between different pairs of electrodes.

We used a 5x g-line stepper[1] and Shipley 1813 photoresist[2] without image-reversal to define the alignment marks and back gate contacts.[3] The alignment marks and back gate contacts were etched into the wafer. First an oxygen descum was used to remove any photoresist residue, then a 200 nm SiO_2 etch, followed by a 500 nm Si etch. Etching was done in various plasma etchers at the CNF: the Oxford 80, Oxford 81, and the Applied Materials RIE 72.

After etching, there were occasionally surface contaminants where the plasma for etching silicon had polymerized the photoresist and made clumps that deposited on the surface and would not come off in either lift-off solvents or an oxygen plasma. A standard MOS clean of the surface, a NH_3OH and H_2O_2 rinse followed by a HCl and H_2O_2 rinse with a brief HF rinse at the end, succeeded in removing the surface contaminates and restoring the previous surface smoothness.

3.3 The catalyst and nanotube growth

After the wafer has been etched, our next step is nanotube growth. We define regions for the catalyst because we want nanotubes in specific places on our

[1] A stepper is a machine with a series of optical elements that takes a mask and focuses light through it so that the mask pattern is produced on the target wafer in a smaller size (here 5 times smaller). After flash exposing the pattern, the wafer is stepped (moved a specific amount) to bring a new area into the focal area to be exposed. The g-line here refers to the wavelength of light used in the exposure: 426 nm.

[2] Here, and in all other uses of Shipley photoresist, we pre-coated the wafer with primer P20.

[3] Image reversal is used for lift-off lithography with metal deposition to create an undercut in the photoresist profile [109]. It is a common enough procedure that it is sometimes assumed, but we will specific if the lithography is image-reversed or not.

chip (between our electrodes). We do nanotube growth before any electrodes are deposited on the surface because the high temperature of our nanotube growth would cause the metals used in our electrodes to melt and diffuse.

To achieve the desired nanotube characteristics, we chose the high-temperature rapid-heating flying-catalyst growth method [44] (a modified chemical vapor deposition growth [57]) from evaporated iron catalyst particles. This growth recipe gives long, straight, mostly single-walled tubes. There are other growth mechanisms in the recipe that can give short, stubby tubes. To simplify out devices, we set the edge of the catalyst pad several microns back from the edge of the electrode to prevent the short tubes from bridging our electrodes.

Catalyst pads were defined with the 5x stepper and Shipley 1805, non-image reversed, and developed in MIF300. Right before deposition, the catalyst pads were cleaned with a brief oxygen plasma. We want the cleanest possible surface for catalyst deposition.[4]

Evaporated iron was used as the catalyst. It tends to give single-walled tubes with smaller diameters, ensuring fewer double or multi-wall tubes. A 1 Angstrom thick sub monolayer of iron was evaporated thermally at a rate of 0.1 Å/s. To achieve such low deposition rates and thicknesses, the tooling factor of the evaporator was artificially inflated from 85% to 400% to increase sensitivity. The evaporator's reported thickness thus has to be multiplied by 0.2125 to infer the deposited thickness.

When evaporated or heated in the growth furnace, the iron has enough mo-

[4] Although not pertinent for evaporated iron, oxygen plasma changes photoresist's surface properties from hydrophobic to hydrophillic, facilitating deposition of a catalyst from solution.

bility on the silicon dioxide to move around until it strikes other iron atoms and forms nanometer-sized clusters. At elevated temperatures (i.e. > 900°C in our growth), these iron nanoparticles catalyze the reaction C_nH_m − > nC + $\frac{m}{2}H_2$. We flow hydrocarbons past our heated catalyst; the hydrogen flows on as a gas and the carbon adsorbs into the iron nanoparticle. The iron becomes supersaturated with carbon. The carbon precipitates out, first forming an end cap along one face of the nanoparticle, then pushing that end cap off and continuing the crystalline growth of the molecule's lattice, resulting in carbon nanotubes [57]. We used Atomic Force Microscopy (AFM) to confirm that the nanotubes grown were mostly in the 1~4 nm diameter range. Figure 3.2 shows an 1 μm by 1 μm AFM image of part of a nanotube. The diameter of the tube is 2.2 nm.

The basic principle behind the flying-catalyst growth is that rapidly heated catalyst particles can lift off the surface of the wafer and be carried in the gas flow, growing a carbon nanotube and trailing it behind. For non-turbulent gas flow, the path of the catalyst particle, and thus the nanotube left behind, is fairly straight. While flying-catalyst growth can result in tubes over a hundred microns long [44], we limited ourselves to devices with an active length of ten microns or less for good conductance.

Nanotube growth remains a process of luck and dedication, with seemingly identical growth efforts yielding drastically different results. Adjustments to gas flow rates and ratios, temperature, placement, cleanliness of tube, and timing can all have appreciable effects. The recipe below serves as some guidelines for growth in the furnace in the McEuen lab, which is a model Lindberg/Blue with one-inch inner diameter quartz tube.

The furnace tube is baked out to clean, open to atmosphere, at 900°C for 30

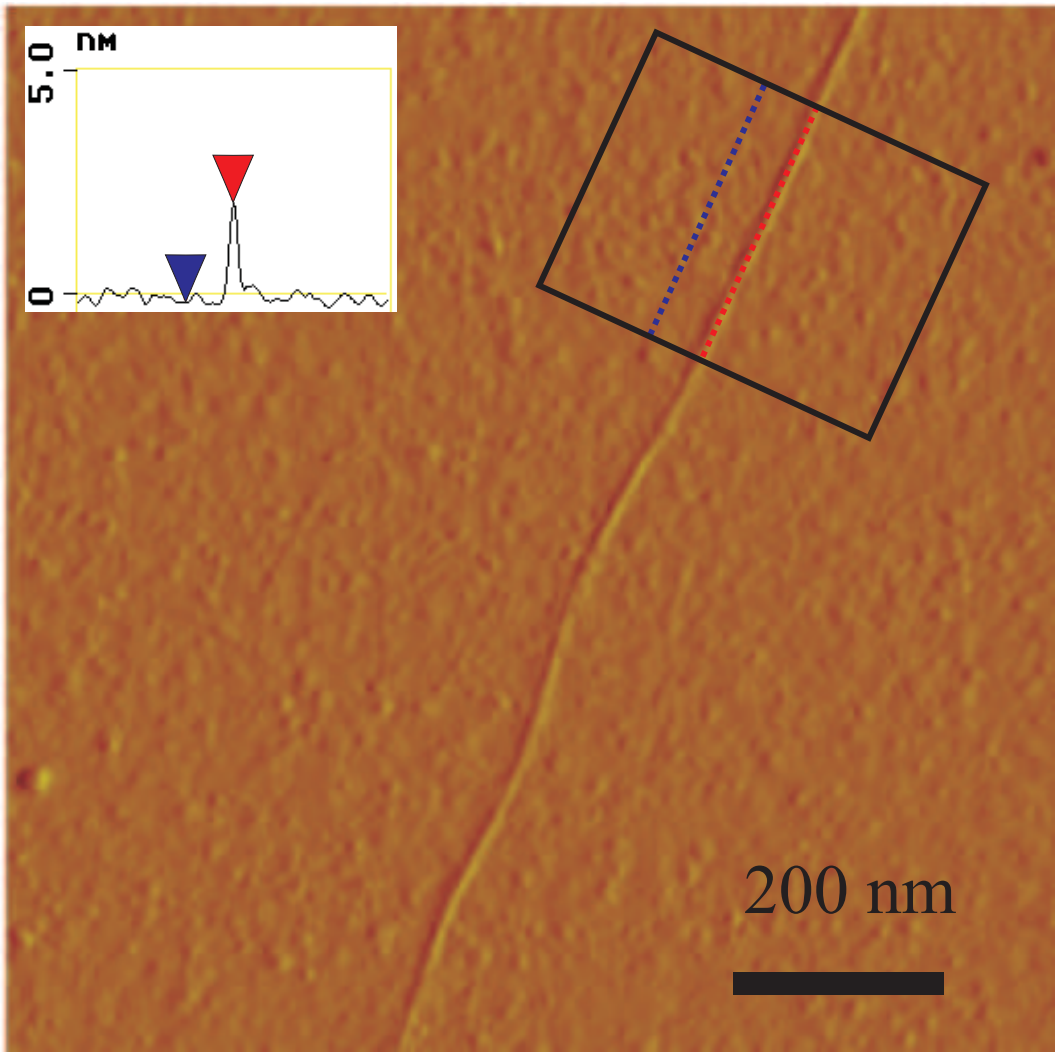

Figure 3.2: An AFM image of part of a nanotube, which allows us to extract the diameter. The tube diameter is averaged over a short length (red dotted line) and compared to an average surface height (blue dotted line) in a small area (inside black box). The tube is 2.2 nm high. Scale bar is 200 nm.

minutes, each third of the tube getting 10 minutes in the middle of the furnace. It is allowed to cool for half an hour. The chip is placed in the tube, and then a permanent marker is used to mark the tube at the edge of the furnace when the chip is centered in the furnace (green mark in figure 3.3, applied in part a). The tube is then moved (toward the upstream side) so that the chip is out of the furnace (3.3b). The gas-flow tubing is then connected to the furnace tube. 0.8 Standard Liters per Minute (SLM) of argon is flowed for six minutes, during which time Snoop (a commercially available soapy water mix) should be used to make sure all the connections on the tube are leak tight (before flowing explosive gases). The furnace temperature is set to 1040°C, and the Ar continues to flow for the six minutes it takes the furnace to heat up and stabilize. 0.2 SLM of H_2, 0.8 SLM of CH_4, and 5.5 Standard Cubic Centimeters per Minute (SCCM) of C_2H_4 is added to the flow for 2 minutes. The 0.8 SLM of Ar is turned off, the tube is moved so that the chip is in the center of the furnace, lining the permanent marker mark up with the edge of the furnace (figure 3.3c), and the temperature is set to 915°C. This is the actual growth step, and the furnace is left this way for 10 minutes. Then, the argon is turned back on at 0.8 SLM. The 0.2 SLM H_2, 0.8 SLM CH_4, and 5.5 SCCM C_2H_4 are turned off. The heat is turned off, and the system is allowed to cool for 30 minutes. This brings the temperature to below 500°C, where it is safe to open the furnace to allow it to cool faster. The argon flow is reduced to 0.3 SLM to save gas. Twenty minutes later, the temperature should be below 100°C, after which the gas flow is turned off, the tube opened, and the wafer piece retrieved. A long hooked aluminum rod is used to initially position the chip and retrieve it from the furnace.

A couple of notes: It is important to continue to flow gas into the tube while cooling to prevent the back-flow of oil into the furnace tube. A double oil trap

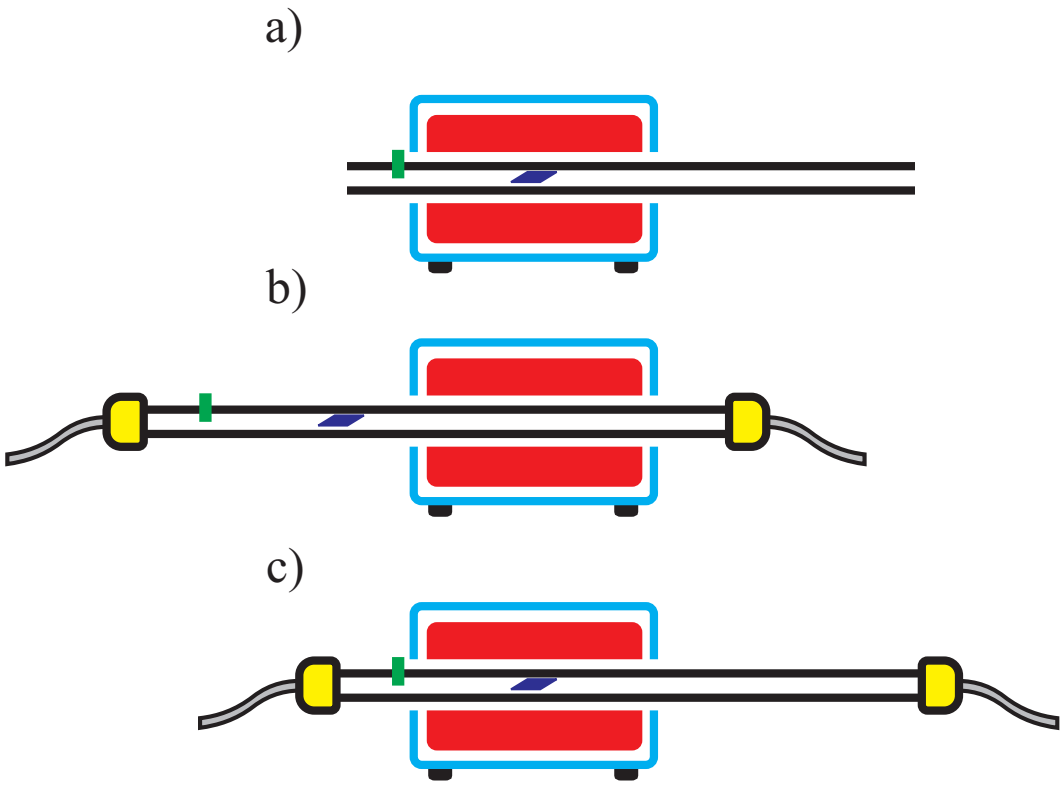

Figure 3.3: Cut away schematic of furnace and growth tube. Furnace box shown in blue, heating element shown in red, permanent marker mark in green, chip in purple, gas flow tubing in grey, fittings in yellow. A) Initial alignment of chip B) Gas flow and preheating furnace C) Growth.

on the downstream side of the furnace (not shown) is used to prevent back-flow of gases into the furnace from the exhaust system. Lore for flying-catalyst growth indicates that the tube should be moved into the furnace as smoothly and as quickly as possible (smooth getting priority over quick). This can often require two people to accomplish effectively, one to move the tube, and one to move the oil trap attached to the end of the tube. When heating the furnace to 1040°C with the majority of the tube sticking out of the upstream side, it may be necessary to put copper cooling fins on the downstream side of the tube to prevent excessive heat from reaching the O-ring and plastics in the tubing connec-

tions (depends on furnace tube length). The flying-catalyst growth gives tubes that grow downstream from the catalyst. The orientation of chip in the furnace should ensure the growth will make nanotubes bridge from one electrode to the next. It is possible to do a flying-catalyst growth with a chip upside-down (allowing a face-up and face-down chip to be stacked). Van der Waals forces, not gravity, is the relevant force for the tube to stick to the surface. The permanent marker mark is not permanent, the high temperature clean will bake it off the tube. As a final note, maintain a log book for the furnace and growth, especially for multiuser facilities.

3.4 Electrode deposition

After growth of the carbon nanotubes, electrodes were deposited for electrical contact. We used a two step/three metal process. In the first step, 10 μm by 50 μm pads of palladium $\sim 30 \pm 10$ nm thick were deposited using Shipley 1813 and standard image-reversal lithography on a 5x stepper. (Image reversal is used to give an undercut photoresist profile to facilitate liftoff of the undesired metal not in the contacts [109].) One pad covers the catalyst pad, and the other is spaced 4 to 10 μm away, downstream (with respect to gas flow) of the catalyst pad. Palladium was used because it makes good p-type contact to carbon nanotubes ([72], [50], [87]). After the palladium pads were deposited and the excess palladium lifted off, more image-reversal lithography was used to put chrome/gold down. A few angstroms to nanometers of chrome was used as an adhesion layer for the $\sim 50 \pm 10$ nm of gold (the gold thickness being at least as much as the palladium thickness). The chrome/gold layer involved large 100 μm by 100 μm contact pads for probing and wire bonding, as well as wiring to connect

those contact pads to the palladium and leave space around the active area of the device for things like AFMing simultaneously with electrical measurement. The chrome/gold layer also included deposits onto the back gate contact areas to allow wirebonding to the doped silicon area. Refer back to figure 3.1 at the beginning of the chapter for a schematic of the device.

3.5 Finding the nanotubes

After the lithography steps were completed, we measured conductance to determine which electrode pairs had carbon nanotubes. The yield of nanotube devices was kept deliberately low to minimize having multiple nanotubes bridge the electrodes. The goal was 10% of electrode pairs having a nanotube, and results varied from less than 1% to more than 30%. While some experiments can be performed with multiple nanotubes, for simplicity and clarity we endeavored to have electrodes with an individual nanotube completing the circuit. Wafer pieces with over a thousand potential devices were run through the one-inch diameter furnace during one growth run. As a consequence, it is important to efficiently and quickly look at thousands of potential devices to determine which actually have nanotubes.

Measuring the conductance between electrode pairs is a high throughput method for determining which pairs have a nanotube. We want to quickly apply a voltage difference between the two electrical contacts and sweep the gate voltage. If there is a conducting nanotube, the voltage difference between the electrodes drives a current. Sweeping the gate voltage helps find devices and gives their conductance as a function of back-gate voltage. Most of our nan-

otube devices have some amount of gate dependence, and sweeping the gate helps to differentiate between nanotubes and problems that might cause conduction between the electrodes, such as residual metal from the lithography steps or gate leakage.

To measure the conductance, two probes are moved in to touch each electrode in a pair, and another probe is used for the back gate. One electrode in the pair was set to 10 mV by a computer controlled DAQ card, and the other was hooked to an Ithaco current pre-amplifier. The current pre-amp outputted a voltage back into the DAQ card, and was read by the computer. The same DAQ card was used to sweep the voltage on the back gate via the third probe. To find which electrode pairs were bridged by nanotubes, the probes are moved from potential device to potential device while looking at the current.[5] Any electrode pair that exhibited a finite current was noted and a detailed scan taken and saved.

Figure 3.4 shows a graph of current versus back-gate voltage. The 10 mV bias between the electrodes drives a current. The current is determined by the conductance of the sample. The graph shows the conductance varying as a function of back-gate voltage. We refer to measuring the conductance between the electrode pairs as a function of back-gate voltage as characterizing the device. This device stops conducting for positive gate voltage, and conducts at negative gate voltage, which tells us that holes are carrying the current. We call this a p-type device because of the positive charge current carriers. The device has some hysteresis in the conductance versus gate voltage curve. The hysteresis is caused by charge traps on the surface being charged or discharged by the back

[5]Although sudden changes to the voltage across a nanotube should be avoided, a change of 10 mV is small enough not to cause a problem.

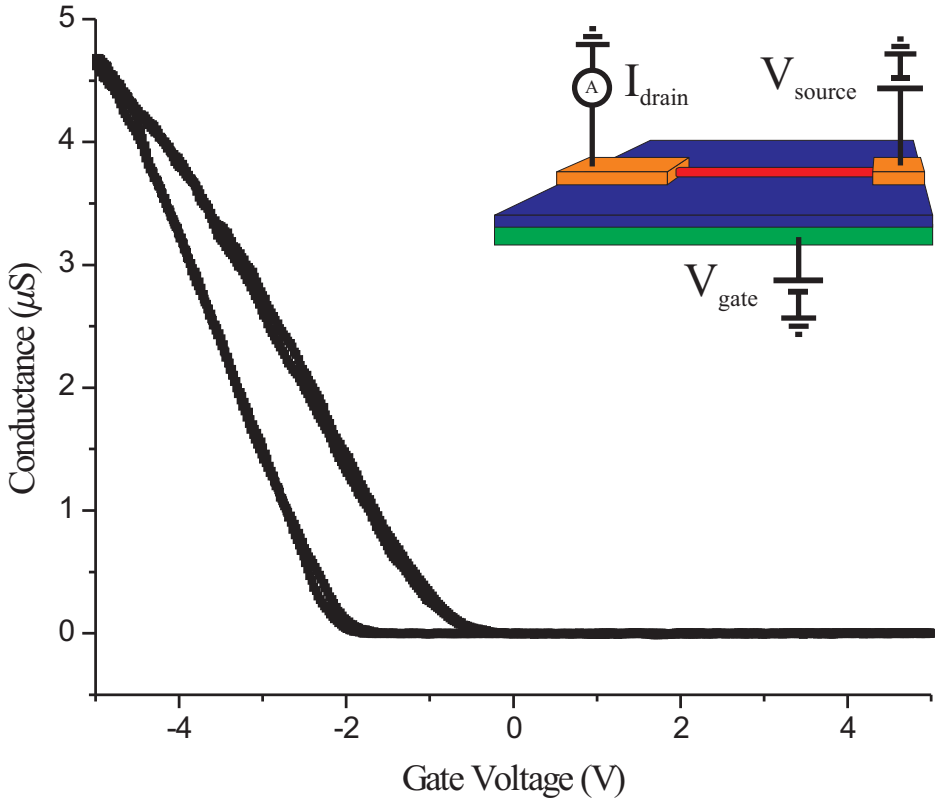

Figure 3.4: Conductance (μS) of a nanotube versus gate voltage (V), measured at 10 mV source-drain. In the gate voltage range we can access it conducts for negative gate voltage, so the holes (p) are carrying the current. There is hysteresis in the gate sweep, causing a slight split in the curve. The inset is a repeat of the CNT transistor, with contacts shown in orange, nanotube in red, oxide in blue and backgate in green.

gate. The conductance here is below the 155 μS theoretical maximum discussed in section 2.2.7 due to a combination of scattering by acoustic phonons [147] and contact resistance between the metal and the nanotube.

Because we want this measurement process to quickly find which electrode pairs have a nanotube, we want a way to continually sweep the back gate while

changing which electrical contacts are being measured. The probe stations used allowed for probes to be placed in a position, and then the chip moved to bring new electrodes into contact with the probes. While the back gate has contact pads on the top surface of the chip, relying on those would require setting the back-gate voltage to zero at the end of every sweep because sudden discrete changes in gate voltage can damage the oxide and the nanotubes.

The following steps were taken to allow quickly changing which electrodes were contacted on top without breaking the electrical connection to the back gate. The back of the wafer piece was scratched with a diamond scribe (to cut through native oxide), and a copper wire was used to rub a eutectic mixture of indium and gallium (liquid metal at room temperature) onto the back of the wafer piece. The wafer piece was then placed on the cleaned and roughened copper plate, with a bit of rubbing of the wafer back against the copper to seat it and ensure good electrical contact. The copper plate was then electrically connected to the back-gate voltage source, either by resting it on a wired platform, or with a flexible wire soldered to the copper plate. This meant that when moving probes from device to device, the back gate remained in electrical contact and thus did not have to be taken to zero voltage between sweeps. The back gate was set to continuously oscillate between plus and minus five volts while looking at the conductance of electrode pairs. This was all done to allow the quick switching of the device being investigated, for higher throughput measuring of potential devices.

After the pairs of electrodes that had nanotubes were determined with conductivity measurements, we measured those pairs with an Atomic Force Microscope (AFM).[6] This let us measure the diameter and the length of the nanotube,

[6]We used a Digital Instruments' Dimension 3100 AFM, using Nanoscope version 4.43r8.

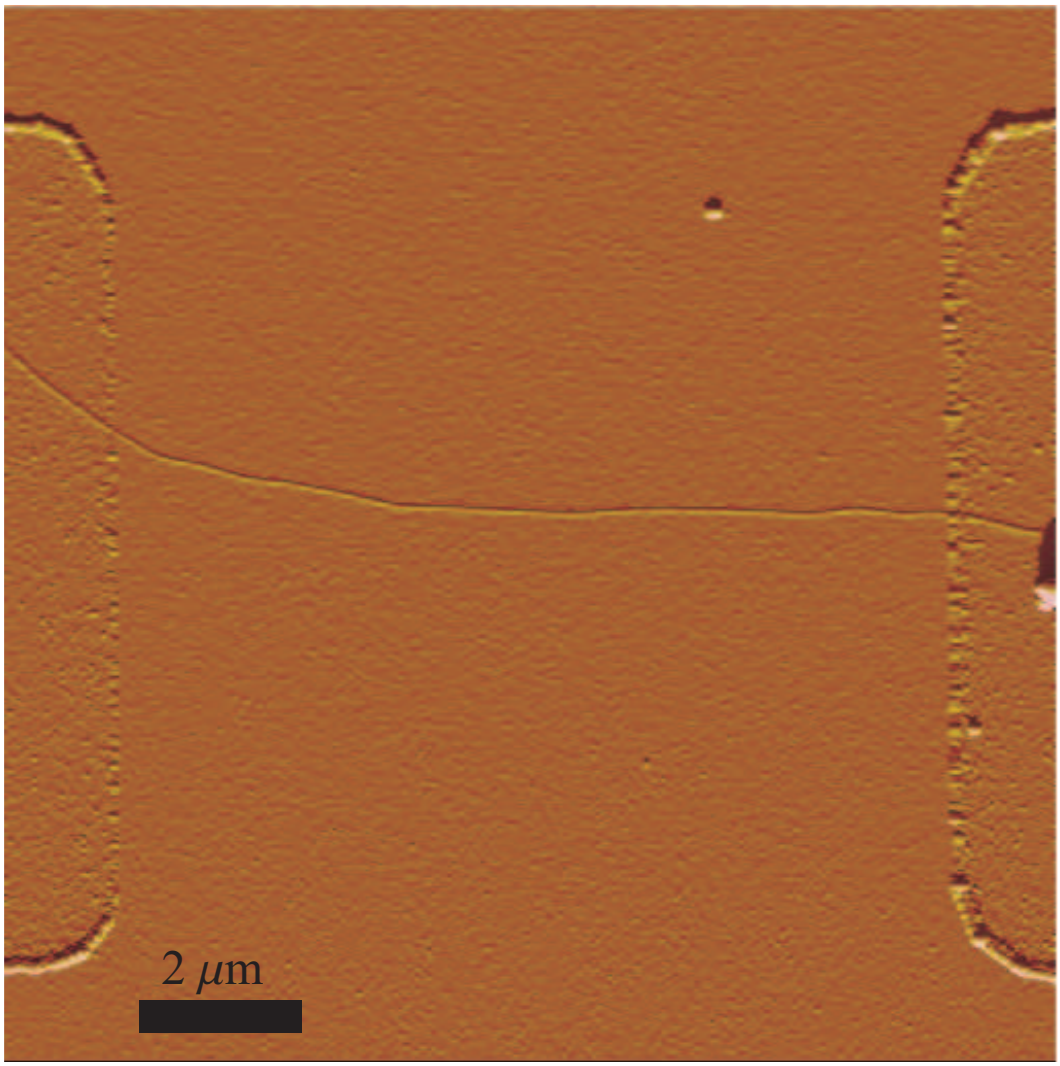

Figure 3.5: An atomic force microscope image of a carbon nanotube transistor. The palladium contacts are visible on the sides of the figure. The nanotube runs from one contact to the other. A small amount of catalyst is visible at the right edge. The scale bar is 2 μm.

and also let us to see how many tubes bridge the electrodes. For these geometric measurements, tapping mode tips were used, with frequencies around 360 KHz. We want to AFM only the electrode pairs we were definitely interested in because of the time intensive nature of using an atomic force microscope. Figure 3.5 shows examples of atomic force microscope image of a nanotube device. The electrical contacts are visible on the right and left, with a tube crossing between them. The fully probed and characterized nanotube transistors are now ready for the unique steps of each of the experiments in this thesis. Chapters 5 and 6 will discuss the specialized fabrication for their experiments. The capacitance experiment of chapter 4 requires a top gate, described in the next section.

3.6 Self-aligned top gate

The following fabrications steps are for a top gate, shown schematically in figure 3.6. The top gate gives the ability to gate the section of nanotube under the top gate without affecting the other sections of the tube. Chapter 4 will go into why this two gate geometry is useful for capacitance experiments. We are certainly not the first to top-gate a nanotube transistor ([134]), but we're doing it in a slightly unusual way and so will provide more detail than in previous fabrication steps. We'll use a self-aligned top gate, where self-aligned means one photolithography step is used for both the barrier oxide and metal electrode.

For the lithography, we used Shipley 1813 spun on at 4000 rpm, giving a photoresist height of 1300 nm to work with during deposition. A two-second exposure in the 5x stepper was used, followed by an 80-minute bake in the NH_3 YES oven. After that image-reversal step, a 30-second ultra-violet flood

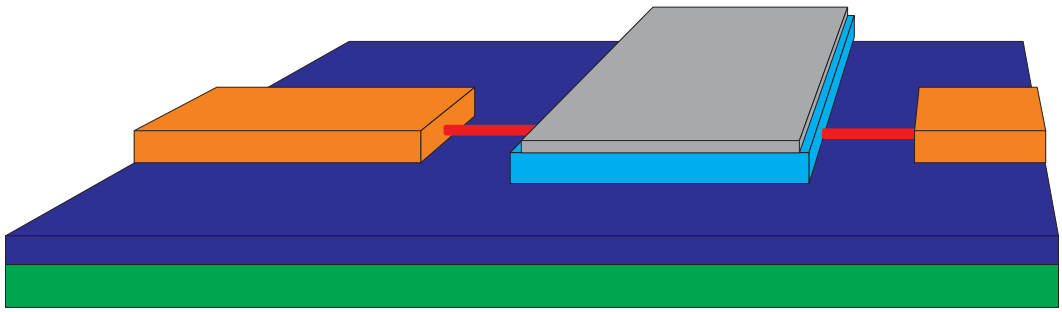

Figure 3.6: The earlier schematic of a CNT FET now with an additional top gate. The nanotube is shown in red. The contacts are orange. The back gate oxide is dark blue, the back gate is green. The top gate oxide is light blue, and the top gate metal is grey.

exposure prepped the wafer for 60 seconds of development in MF 321. After development, the wafer was ready for deposition.

We want to deposit the barrier oxide for the top gate and the metal right on top of it, but we do not want any metal hanging over the edges of the oxide and shorting-out to the nanotube. To accomplish this, we do a three step deposition that relies on the finite thickness of the photoresist. We made two oxide depositions. In the first, the wafer was mounted such that the surface-normal did not point at the evaporation source, but 5° off to the side, see figure 3.7b. Half of the desired oxide thickness was evaporated. The photoresist's thickness and undercut profile means the deposited oxide is not in the middle of the exposed region. We then turned the wafer so that the surface-normal pointed 5° away from the evaporation source to the other side, and deposited the second half of the desired oxide thickness, figure 3.7c. This created a top-hat like oxide profile, with the full width of oxide in the middle, and a skirt of half oxide thickness along the edges. We then moved the wafer to the standard position of surface-normal pointing directly at the evaporation source and deposited the

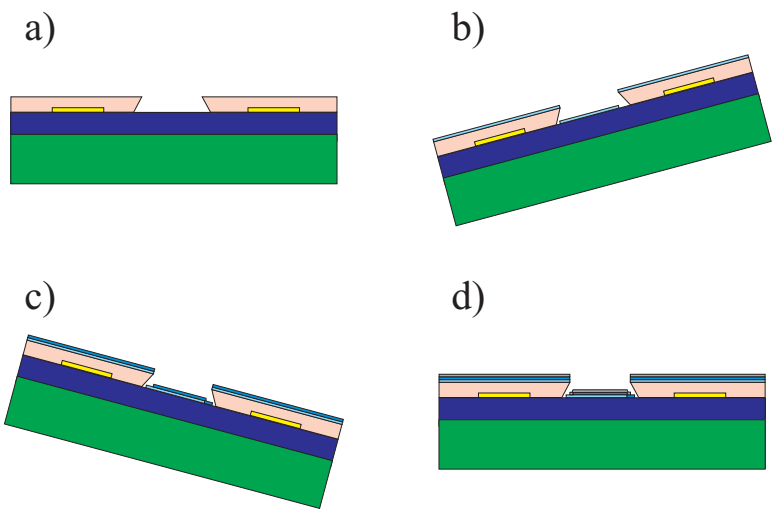

Figure 3.7: Self-aligned top gate deposition. Green is the doped silicon back gate, blue the 200 nm oxide, pink the photoresist, yellow the electrical contacts buried under photoresist. a) The standard orientation for deposition b) The first layer of silicon oxide is deposited (baby blue) c) The second half of the silicon oxide is deposited (sky blue) d) The aluminum for the top gate electrode is deposited (grey). The 15° angle here is an exaggeration of the 5° angle used in the experiment.

metal for the top electrode, figure 3.7d. This metal is mostly on top of the full oxide thickness, with a small amount overhanging onto the half oxide thickness skirt. The oxide skirt extends farther than the metal. The angles in figure 3.7 are exaggerated and the oxide layers colored differently for clarity.

A stage allowing sample rotation while inside the evaporation chamber allowed us to make all three depositions during one pump-down of the chamber. Figure 3.8 shows the rotatable evaporation stage. Given our device geometry and the fact that just two oxide depositions were used, we want to make the axis of rotation of the wafer parallel to the long axis of the top gate, since there won't be a protective skirt all around the top gate. This ensures that where the metal possibly overhangs the oxide (at the tip of the top gate), it is unlikely to

come in contact with a nanotube bridging the electrodes.

We chose aluminum as the top gate metal, because it forms a native surface oxide ~ 2 nm thick and is thus unlikely to short the nanotube at its edges. For barrier oxide, we tried both electron gun evaporated aluminum oxide and thermally evaporated silicon oxide, with more success from the silicon oxide.

For the silicon oxide, a baffle boat was used during deposition. A baffle boat, see figure 3.9, is an evaporation boat with barriers that prevent the evaporated material from going immediately to the target. The thermal evaporation of SiO_x can lead to high energy molecules that do not immediately stick to a surface when evaporating, but instead bounce several times before sticking. To reduce angled deposition from rebounds off the walls of the evaporation chamber, the baffle boat requires evaporated SiO_x to rebound several times before emerging as a fairly collimated evaporation beam. Any silicon oxide molecule that bounces instead of depositing on the wafer would bounce away from the wafer and be unlikely to rebound enough times to come back to the wafer at an oblique angle.

After deposition, we soaked the wafer in 1165 to remove the remaining photoresist and liftoff the material sitting on top of the photoresist. This was followed by an acetone and IPA rinse, then a blow dry using compressed air. If liftoff was not complete, a hypodermic needle was used to draw up 1165 while the wafer was still submerged and spray 1165 across the surface of the wafer. This high-velocity fluid flow was used to remove any loose bits of metal that lifted off the surface but were tenuously stuck to the metal deposited on the surface.

Figure 3.8: Rotatable stage used for angled deposition of material (shown upside-down compared to how it is used). a) Where chip would be placed, with top gate axis running horizontally b) Liquid nitrogen reservoir c) Input and outflow pipes for liquid nitrogen d) Knob for setting angle of stage.

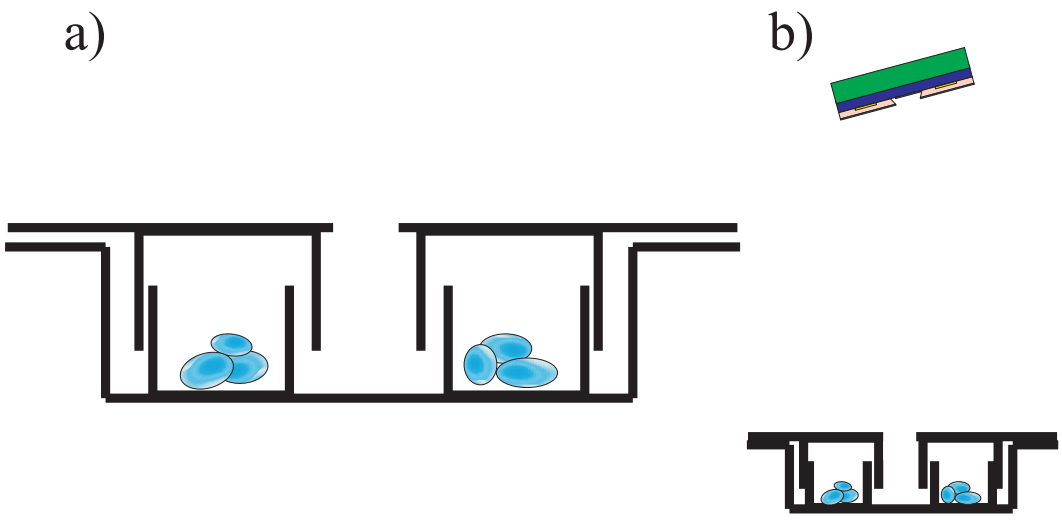

Figure 3.9: a) Cut away cross section of baffle boat used for silicon oxide deposition. Thermal leads would be clipped to the edges, and the entire boat heated to drive evaporation. The evaporating oxide (blue pellets) escapes through the hole in middle after several rebounds. b) Schematic of the baffle boat being used to deposit oxide onto a wafer.

For some initial devices, we used AZ 5214 E photoresist from Clariant instead of Shipley 1813, because AZ 5214 E doesn't require an NH_3 bake for image-reversal. We discovered later, however, that AZ 5214 E tended to leave residue on the nanotubes. This residue made diameter measurements difficult to impossible, and seems to have added local charge traps around the nanotube that prevented clean measurement of capacitance versus top-gate voltage. Devices made with AZ 5214 E were able to contribute to capacitance as a function of length measurements, but for detailed measurements the Shipley photoresist gave much higher quality devices. We suggest that anyone who duplicates of continues this research use Shipley photoresists instead of AZ 5214 E.

CHAPTER 4

CAPACITANCE MEASUREMENT OF INDIVIDUAL CARBON NANOTUBES

4.1 Introduction

We report here the first direct capacitance measurements of individual carbon nanotubes. These measurements show how the band structure of the nanotube affects the capacitance. We model the capacitance of a carbon nanotube and compare our model to the experimental data. Careful analysis of our data reveals evidence of electron-electron interactions. This chapter is an expansion and elaboration of the work reported in "Measurement of the quantum capacitance of interacting electrons in carbon nanotubes," published in Nature Physics[46].

The capacitance of a nanotube is very small, and the structure in that capacitance related to the band structure is even smaller. In section 4.2, we'll sketch the technical challenges and why they are worth undertaking. To meet the technical challenge of isolating the small capacitance, we'll use the two-gate device geometry shown in figure 4.1. The gates affect the conductance in different sections of the nanotube, detailed in section 4.4. Controlling the conductance of sections of the nanotube allows us determine what part of the measured capacitance (section 4.3) comes from the nanotube (section 4.5). We use these tools to measure capacitance as a function of length in section 4.6. Section 4.7 looks closely at the capacitance to see effects from the band structure. We compare our theoretical predictions (section 4.8) to the measured results in section 4.9; and discuss future directions for this research in section 4.10.

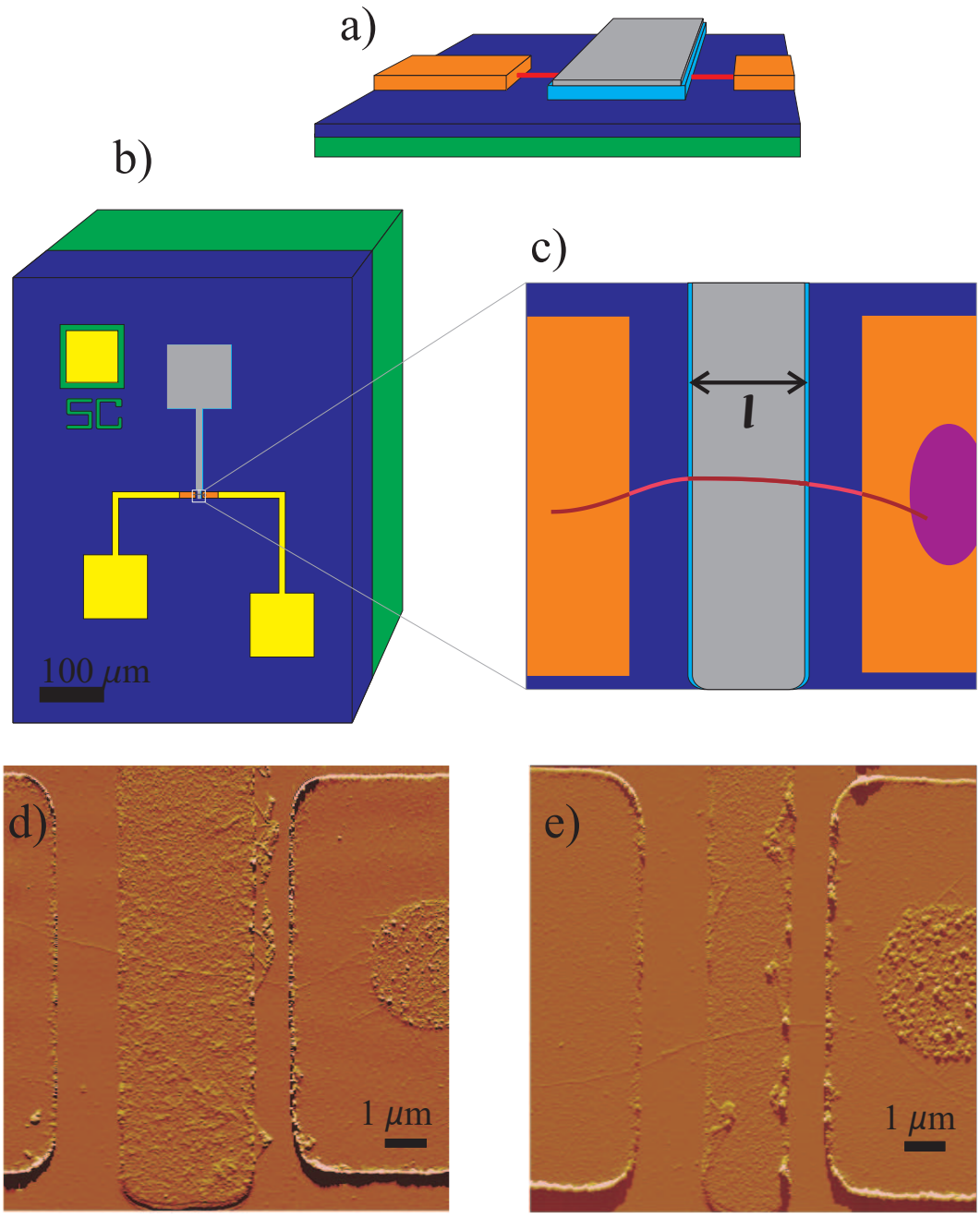

Figure 4.1: Schematic and atomic force microscope images of top-gated devices. a) Schematic side view of top-gated device, as shown in figure 3.6 b) Schematic side view of top gated device as it appears on wafer c) Zoom in of nanotube area, showing catalyst in purple, palladium in orange, nanotube in red, and top gate's barrier oxide in light blue. The distance l is the length of the top-gated section of a straight nanotube. d) and e) AFM images of top-gated devices. Scale bars are 1 μm.

Devices with top gate and back gate are shown in figure 4.1. The schematic of the device is given is 4.1a & b with a blow-up of the nanotube region in 4.1c. The nanotube runs under a top gate that has been interdigitated between two electrical contacts on either end of the nanotube. The width of the top gate, l, can be varied in different devices, as seen in 4.1 d & e, to give different lengths of top-gated nanotube.

4.2 Motivation and challenges

The capacitance of a system is a fundamental and important electrical property [71]. Given the extensive promise of electrical devices involving carbon nanotubes [53], there should be a clear measurement of the capacitance of an individual tube. The capacitance of a nanotube contributes to the RC time of the nanotube, and thus affects the possible speed of any electronics relying on the nanotube. The capacitance is also required to infer the mobility from conductance. Mobility is an important benchmark and comparison tool for different electronic systems. Measuring the capacitance facilitates a deeper understanding of how nanotubes will behave electronically. At a more fundamental level, measuring the capacitance gives us a probe of the density of states of the nanotube. Before describing the predictions for how the density of states will appear in the nanotube's capacitance, we will first establish the size of the electrostatic capacitance.

The signal we expect to see for a nanotube's capacitance is on the order of hundreds of attoFarads. This estimate comes from a simple model. We model the nanotube as a wire of radius d, embedded in oxide with dielectric constant

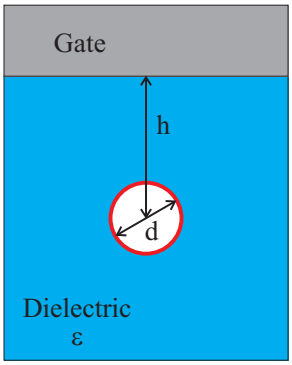

Figure 4.2: A simple model of nanotube, diameter d, a distance h away from a metal gate, embedded in a dielectric with constant ϵ.

ϵ, a distance h away from a gate (see figure 4.2). For this system, the classical electrostatic capacitance per unit length of the wire to the metal plane is:

$$\frac{C_{electrostatic}}{L} = \frac{2\pi\epsilon_o\epsilon}{ln|\frac{4h}{d}|}. \tag{4.1}$$

We use silicon oxide, with an ϵ of 3.9. Our devices have an h of 10 nm. The diameters of our tubes run from 1 to 4 nm, and the lengths involved from 2 to 4 μm. We thus expect electrostatic capacitances for the tube to be roughly 100 to 400 aF. This is a very small capacitance compared to capacitance values encountered in standard laboratory equipment. For instance, the capacitance of a BNC cable to ground is of order 100 nF (that's 100,000,000 aF). Section 4.3 will discuss how we overcome this to extract our small signal.

The challenge of investigating the band structure is even more difficult, because the change in capacitance from the band structure will be roughly 10% of the nanotube's electrostatic capacitance. To see this, we need a more rigorous look at the definition of capacitance. Classically, the capacitance of an object is defined as $C = Q/V$. The capacitance relates the charge on an object to the voltage the object is at, that is $Q = CV$.

More accurately, the capacitance relates the change in electrochemical potential, $\partial\mu_{ec}$, required to change the charge of the system by ∂q[71]:

$$\partial q = C_{Total} * \partial(\mu_{ec}/e). \tag{4.2}$$

We recover the classic $Q = CV$ by integrating equation 4.2 to charge Q and using that the electrochemical potential is determined by the gate voltage $\mu_{ec} = eV_{gate}$.

The electrochemical potential takes into account the energy required from both electrostatics, $e\Phi$, and the chemical potential, μ_c. The chemical potential for our system is to good approximation the Fermi energy, because at the temperature of our experiment, the smearing of the Fermi level is small compared to the Fermi energy. The electrochemical potential is thus

$$\mu_{ec} = \mu_c + e\Phi \cong E_F + e\Phi. \tag{4.3}$$

Using this expression for the electrochemical potential in equation 4.2 gives

$$\partial q = C_{Total}\partial(\mu_{ec}/e) = C_{Total}\partial V_{gate} = C_{Total}(\partial(\mu_c/e) + \partial\Phi). \tag{4.4}$$

We reiterate that electrochemical potential μ_{ec}, *not the electrostatic potential* Φ, is directly set by the gate voltage.

Re-writing 4.4 in terms of C^{-1}_{Total} gives:

$$C^{-1}_{Total} = \frac{1}{e}\frac{\partial}{\partial q}(\mu_{ec}) = \frac{1}{e}\frac{\partial\mu_c}{\partial q} + \frac{\partial\Phi}{\partial q} = C^{-1}_{DoS} + C^{-1}_{electrostatic}. \tag{4.5}$$

The electrostatic capacitance is the $\dfrac{\partial\Phi}{\partial q}$ term, and we assign the term density of states capacitance, C_{DoS}, to the chemical potential term, because [6][28]

$$C^{-1}_{DoS} = \frac{1}{e}\frac{\partial\mu_c}{\partial q} \cong \frac{1}{e}\frac{\partial E_F}{\partial q} = \frac{1}{e^2 L}\frac{1}{g(E)}, \tag{4.6}$$

where $g(E)$ is the density of states and L is the length of the system. We've used that the derivative of the Fermi energy with respect to number of particles is

one over the quantity density of states times length of the system. This means that C_{DoS} is proportional to the density of states. Succinctly, the density of states capacitance per unit length is

$$\frac{C_{DoS}}{L} = C'_{DoS} = e^2 g(E). \tag{4.7}$$

The density of states for a semiconducting carbon nanotube was shown in figure 2.14. C_{DoS} has the same structure, scaled by the square of the charge, see figure 4.3b. There is a central region where C_{DoS} is zero, bounded by van Hove singularities where C_{DoS} is infinite. C_{DoS} decreases from the van Hove singularities as $1/E$, until new van Hove singularities from higher bands appear and drive C_{DoS} back to infinity.

The total capacitance per unit length for a nanotube, the series addition of C_{DoS} and $C_{electrostatic}$, is shown in figure 4.3c. In the center of the C_{Total} plot, the capacitance is zero. For $C_{Total}^{-1} = C_{DoS}^{-1} + C_{electrostatic}^{-1}$, when the density of states capacitance goes to zero, total capacitance must also go to zero. If a charge can't move onto the system because there are no available states, the system has zero capacitance.

The van Hove singularities in C_{DoS}, where the density of states goes to infinity, makes C_{Dos}^{-1} zero, and thus the total capacitance equals the electrostatic capacitance. In energy terms, the two capacitances adding in series means that an electron added to the systems pays an energy cost associated with each capacitor. When the density of states goes to infinity, it doesn't take any level spacing energy to add an electron to the system. The peak capacitance value is thus the purely electrostatic capacitance.

In the tails of the first van Hove singularities, when the density of states capacitance is order 500 aF/um, we expect a 6 aF/um correction to a geometric

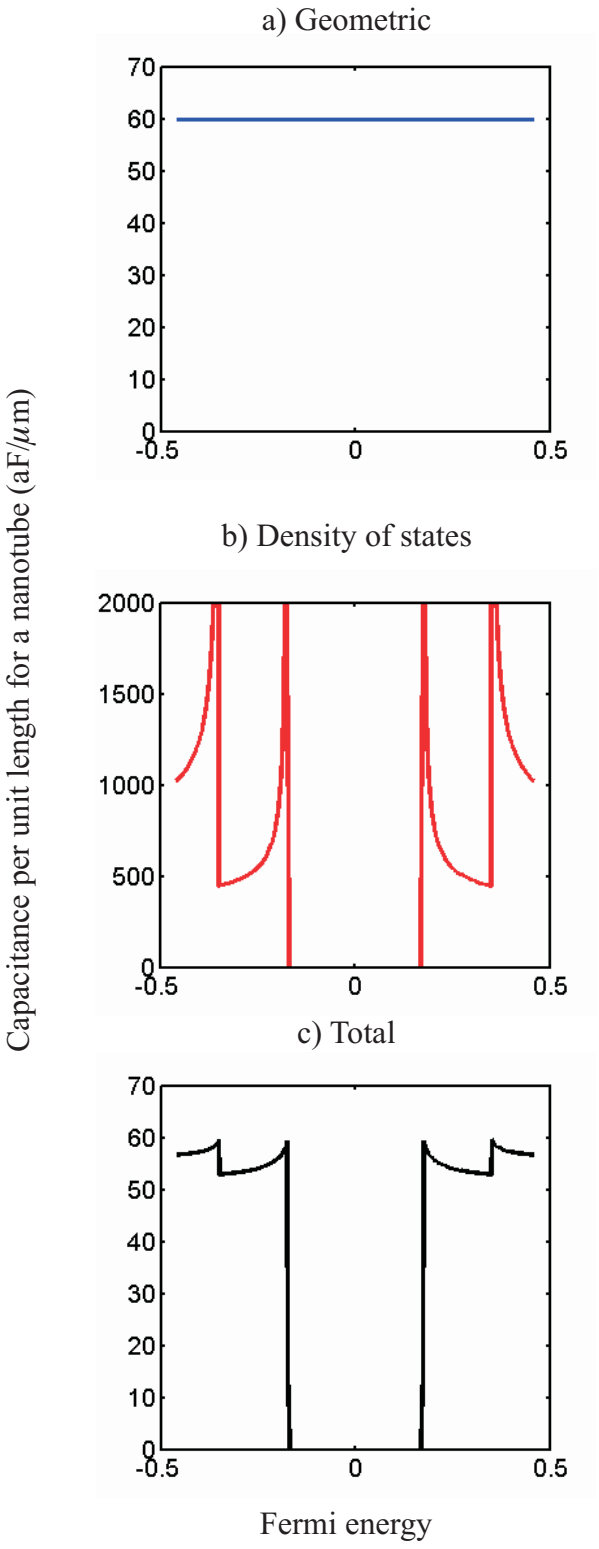

Figure 4.3: Capacitance per unit length for a nanotube, diameter 2.35 nm, embedded in oxide with $\epsilon = 3.9$. a) Geometric b) From density of states c) Total

capacitance signal of 60 aF/um. Outside the bandgap, the density of states information will be a ~10% correction on top of the geometric capacitance. Section 4.3 steps through the measurement technique that achieves an accuracy of 1 aF, allowing us to extract information about the density of states from the capacitance measurement.

4.3 Capacitance measurement

This experiment requires measuring capacitance on the order of attoFarads against background signals that are various orders of magnitude larger. This section highlights the methods used to extract that signal. Figure 4.4 gives a schematic representation of the background capacitance signals. Stray capacitances to ground (such as a BNC's ~10 pF capacitance) are accounted for with a capacitance bridge, which will be discussed in section 4.3.1. We built a shielded cryostat to cool the system, reduce electrical noise, and allow for long averaging times. The cryostat is discussed in section 4.3.2. We minimize on-chip cross-capacitance (i.e. contact pad directly to top gate, ~10 fF) in the design of the device. The dominate capacitive coupling between the contacts and the top gate is through out-of-plane field lines arcing from one to the other. The electrical contacts to the nanotube and top gate are in a plane. On one side of this plane, 200 nm of silicon dioxide away, is the back gate. The back gate is held at a defined voltage, which (helps) prevent a voltage on the contacts from inducing a charge on the top gate. The capacitance to the back gate is functionally a capacitance to ground, and thus removed from the measurement by the capacitance bridge (discussed next).

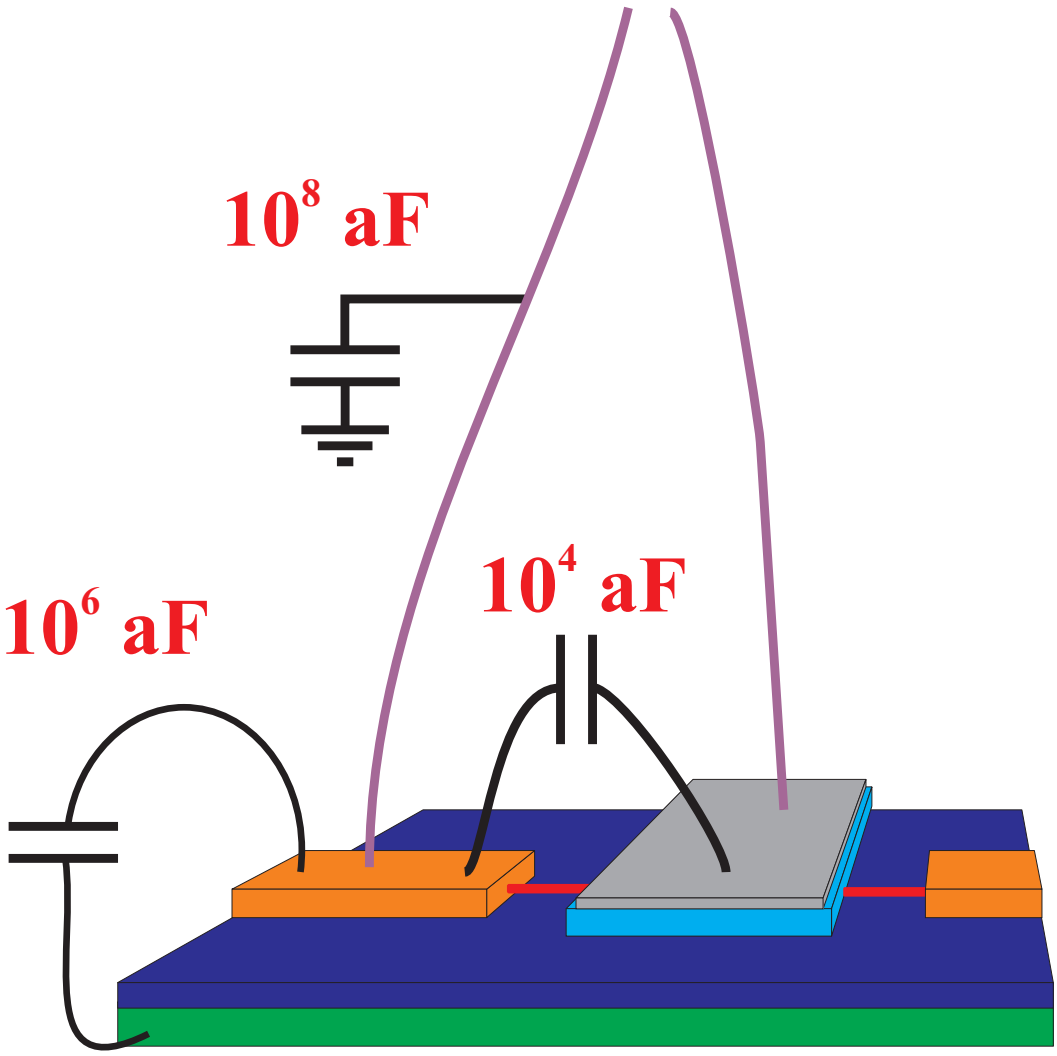

Figure 4.4: Section of schematic showing scale of various background capacitances in the experimental setup. Orange: electrical contact to nanotube. Grey: top gate. Light blue: top gate oxide. Dark blue: back gate oxide. Green: back gate. Red: nanotube. Purple: macroscopic wiring like SMA or BNC cables. Black: examples of capacitive coupling between different electrical components. Macroscopic wiring to ground: 10^8 aF. Contacts to back gate: 10^6 aF. On chip capacitance between electrical contacts and top gate: 10^4 aF.

These techniques allow us measure the small capacitance of the system. We isolate the nanotube's contribution to the capacitance using the distinctive conductance dependence of the top-gate/back-gate system. The conductance is described in section 4.4 and utilized in section 4.5.

4.3.1 Capacitance bridge

A capacitance bridge is a useful tool for measuring small capacitances. The following is a discussion of how a capacitance bridge, schematic shown in figure 4.5, operates. The bridge uses a variable transformer to balance the load between the sample and a known reference. C_o and R_o are a reference capacitor and reference resistor inside the bridge. [1] C_s and R_s are the capacitance and resistance of the sample attached to the capacitance bridge. The sample here will be the nanotube device and all the wiring that leads to it.

The variable transformer balances the system such that the voltage at the detector (red point) is zero. Any stray capacitances to ground or capacitance of shielding (i.e. to ground) is thus just an extra load on the transformer. In figure 4.5, a stray capacitance to ground in the sample is labeled C_{bad} (in grey). C_{bad} is a capacitance from detector point to ground and thus the voltage across it is zero. The sample is different than stray capacitances because the sample's two ends are attached to two leads on the transformer, not to ground.[2]

We used an Andeen Hagerling 2700A capacitance bridge. The measure-

[1] The bridge actually has several different reference capacitors and a calibrated variable resistor R_o.

[2] It is worth noting that the bridge's two sample leads are not symmetric. One cancels out stray capacitances. The other (bottom line with $V_{s,DC}$ in diagram) doesn't cancel stray capacitances. The shielding should thus be attached to the load point side, which is marked on the capacitance bridge.

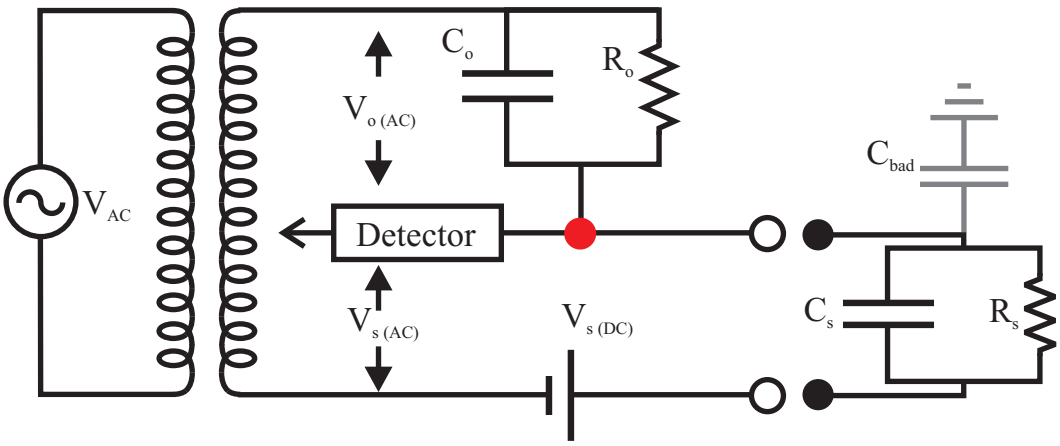

Figure 4.5: Schematic representation of a capacitance bridge. There is an AC voltage coupled to the bridge through an adjustable transformer. The detector balances the bridge by making the voltage at the detection point (red dot) zero; putting $V_{\circ\,(AC)}$ across the reference $C_\circ$ and $R_\circ$ and $V_{S\,(AC)}$ across the sample C_S and R_S. The bridge has an array of reference capacitors and a variable resistor $R_\circ$ to facilitate balancing. Stray capacitances to ground, like C_{bad}, have no AC voltage across them and simply load the transformer. The bridge allows for DC gating of the sample through $V_{S\,(DC)}$.

ments were performed with an AC excitation voltage of 25 to 100 mV at a frequency of 1 kHz. The noise level of the capacitance bridge was 50 $e/\sqrt{\text{Hz}}$. If we measure for time $t_{measurement}$, then the charge resolution of the bridge is $\frac{50e/\sqrt{\text{Hz}}}{sqrt t_{measurement}}$. The charge accuracy becomes a capacitance accuracy using $C = Q/V$ where the V here is the excitation voltage. This means for very fine scans, we could average roughly two hours with a 100 mV excitation,

$$C = \frac{\frac{50e/\sqrt{\text{Hz}}}{sqrt 7200\text{s}}}{100\text{mV}} = 9.4 * 10^{-19}\text{aF}, \tag{4.8}$$

for an accuracy of 1 aF.

In our devices, we measure the capacitance from top gate to nanotube. Both

contacts used to measure conductance of the nanotube were electrically connected to one side of the capacitance bridge, and the top gate was connected to the other side.

The bridge allowed us to apply a DC voltage to the top gate while measuring the capacitance. This is important both for gating the center section of the nanotube into a region where the nanotube conducts well, and for looking at the capacitance as a function of top-gate voltage, discussed in section 4.7.

4.3.2 Nitrogen cryostat for capacitance measurement

The attoFarad resolution of the capacitance bridge requires long averaging times. We built a shielded probe stick that allowed us to cryogenically cool the sample to reduce electrical noise and drift.

Figure 4.6 is a picture of the system.[3] The chip is ensconced in a grounded Faraday cage to reduce pickup of external fields. The cage is inside a vacuum can (also grounded). Electrical contact to the sample was through six shielded SMA lines running the length of the stick[4] and accessible at the top. The vacuum can used a taper fit seal with vacuum grease.[5] Low temperature was used to freeze out mobile charges on the surface of the chip, reduce electronic noise, and increase stability to allow for averaging. The measurements were carried

[3]It is important in any cryogenic system like this to have a pressure relief valve. If cryogenic liquid leaks into a vacuum can, it will attempt to evaporate and expand rapidly when the can is removed from the cooling storage dewar. If the leak closes when the can is pulled out (condensation plugs it, etc.), or it can't vent pressure fast enough, a vacuum can without a pressure relief valve functionally becomes a bomb.

[4]Six is more than required, but always build a cryostat with more wires than you think you need.

[5]To remove can, screw the vacuum-can remover (figure 4.6l) onto the bottom of the vacuum can. The disk is free to move on the screw. Allowing the disk to fall ~inch onto the screw-head breaks taper fit seal.

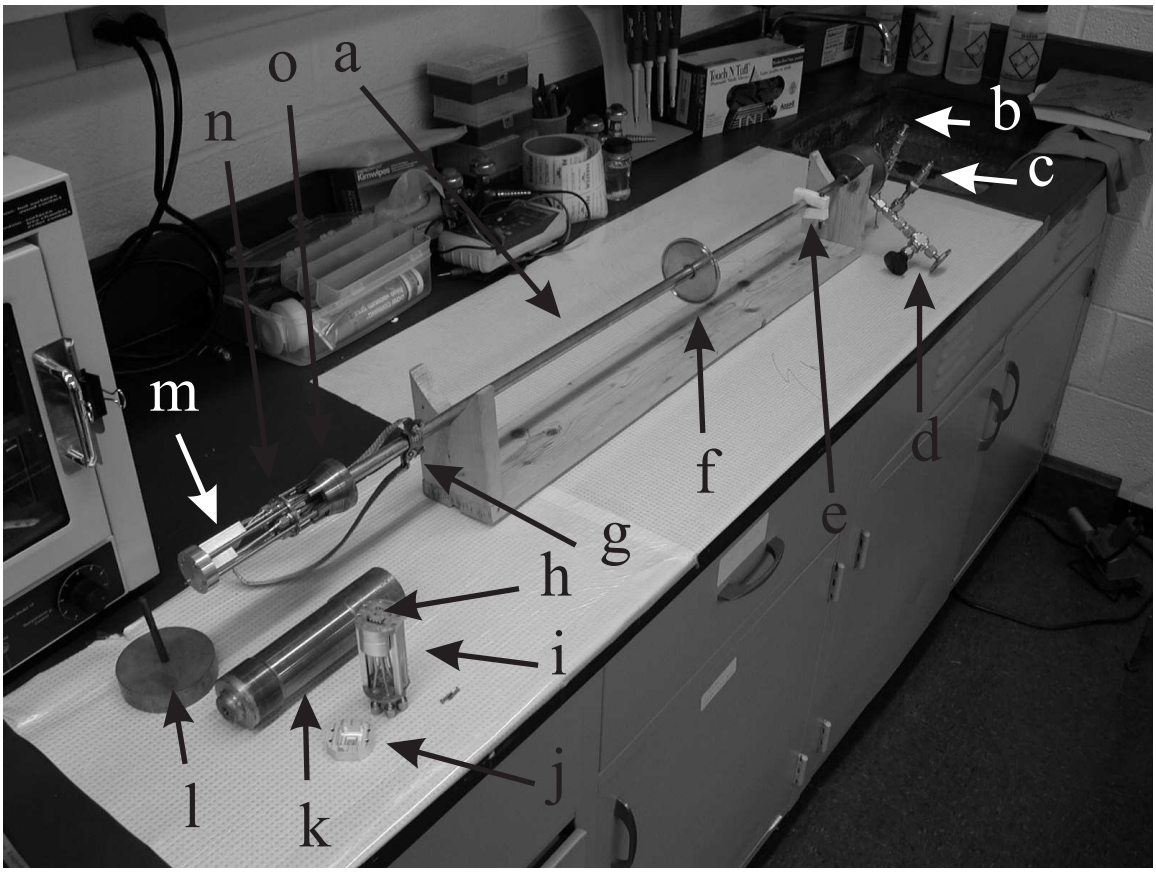

Figure 4.6: Picture of the cryostat used in the capacitance experiment. a) Stainless steel tube for submerging sample in cryogenic dewar b) SMA connectors with BNC adaptors at top of cryostat c) Pressure relief valve d) Vacuum port for pumping out system e) Clamp to set depth in dewar f) Flange to mate with top of dewar g) Grounding (and retention) strap for can h) sample location i) Removable sample mount j) Shielding cap for sample mount k) Vacuum can l) Vacuum-can remover m) Another sample mount, mounted on stick n) Attachment point for sample mount o) Taper fit for vacuum can.

out at 77 K by submerging the sample (in the vacuum can assembly, with a small amount of helium exchange gas) in liquid nitrogen. Lower temperatures (i.e. a liquid helium bath, etc.) were not used because the conductance of the samples would change. At liquid helium temperatures, coulomb blockade becomes the dominate feature of the conductance as a function of gate voltage [79]. We use the conductance of our device, described in section 4.4, as the final tool to isolate the nanotubes capacitance from any remaining system capacitance (section 4.5).

4.4 Conductance measurements of top-gated devices

We use a two-gate device geometry to facilitate the capacitance measurement. (The extra fabrication steps for these devices was discussed in section 3.6.) This dual gate geometry causes a more complicated relationship between current and gate voltage, which we will use in section 4.5 as part of the capacitance measurement. We will look at the conductance as a function of both gates in this section, but we'll start by looking at the conductance as a function of just one gate voltage.

Figure 4.7 shows conductance as a function of top gate voltage for a constant back gate voltage of -7 V. The nanotube conducts for top gate voltages less than -2 V. The nanotube does not conduct in the top gate range of -2 V to -1V. The figure looks similar to figure 3.4. We've averaged each point 60 times and only measured the current for one direction of gate voltage sweep, so there is little noise and no visible hysteresis. The measurements were taken at 77 K using the liquid nitrogen cryostat described in figure 4.6. The current in figure 4.7 is being carried by holes.

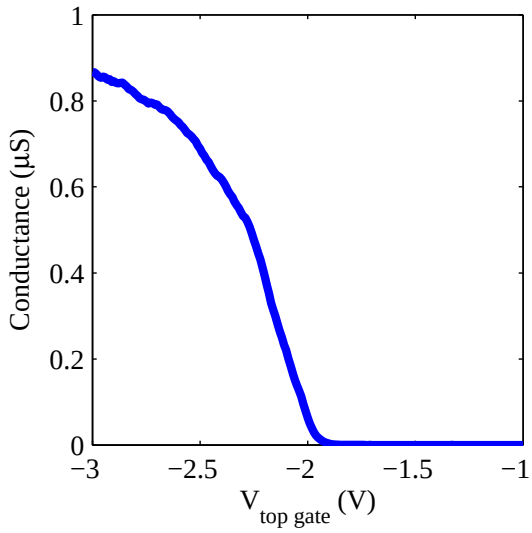

Figure 4.7: Nanotube conductance (in μS) versus top gate voltage (in V) for a constant back gate voltage of -7 V.

We now look at conductance versus top gate voltage for a constant back gate voltage of +7 V in figure 4.8. Here, the device conducts for top gate voltages larger than -1.2 V, but the maximum conductance is orders of magnitude smaller than the best conductance for negative back gate voltage. We've again measured the current in only one direction of gate voltage sweep. This time 100 points were averaged. The temperature was still 77 K. The current in figure 4.8 is being carried by electrons. The electron carried current in figure 4.8 has begun to turn on at top gate voltages where the hole carried current of figure 4.7 is still off. We now look at a two dimensional plot of conductance versus both gate voltages to explain this.

Figure 4.9 shows conductance plotted as a function of top-gate and back-gate voltage. The immediately apparent features are that there are two regions of conductivity, dependent on both gate voltage values, and a large area with very poor conductance. At back gate -7 V, the device conducts for top-gate volt-

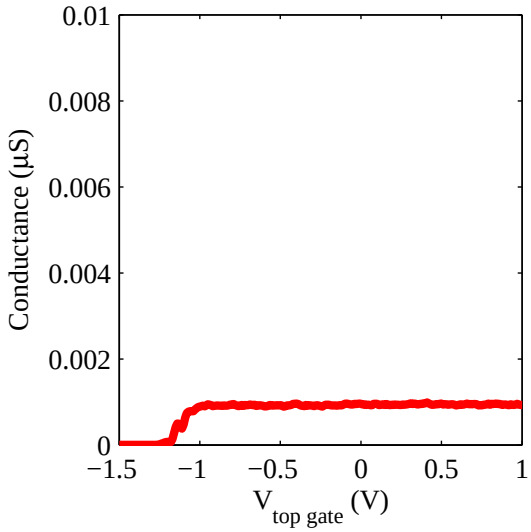

Figure 4.8: Nanotube conductance (in μS) versus top gate voltage (in V) for a constant back gate voltage of +7 V. Note the vertical axis covers a smaller range than in figure 4.7.

ages less than -2 V (the region labeled ppp in figure 4.9). The white dashed line on the figure marks the line trace corresponding to figure 4.7. The negative voltages on the gates creates an incompletely filled valence band in the nanotube, and the current is carried by holes. At +7 V back gate, the current flows for top-gate voltages larger than -1.5 V (the region labeled nnn in figure 4.9). The black dotted line marks the line trace for figure 4.8. Here the gates have filled the valence band and partially populated the conduction band. The current is carried by the electrons in the conduction band.

Each of the gates has the ability to impose a carrier type on part of the nanotube. Figure 4.10 shows the grid of the carrier types for the different gate voltages from figure 4.9. In the upper right corner of figures 4.9 and 4.10, the section of nanotube under the top gate is electron (n) doped by the top gate. The sections between the contacts and the top gate are n-doped by the back gate. We

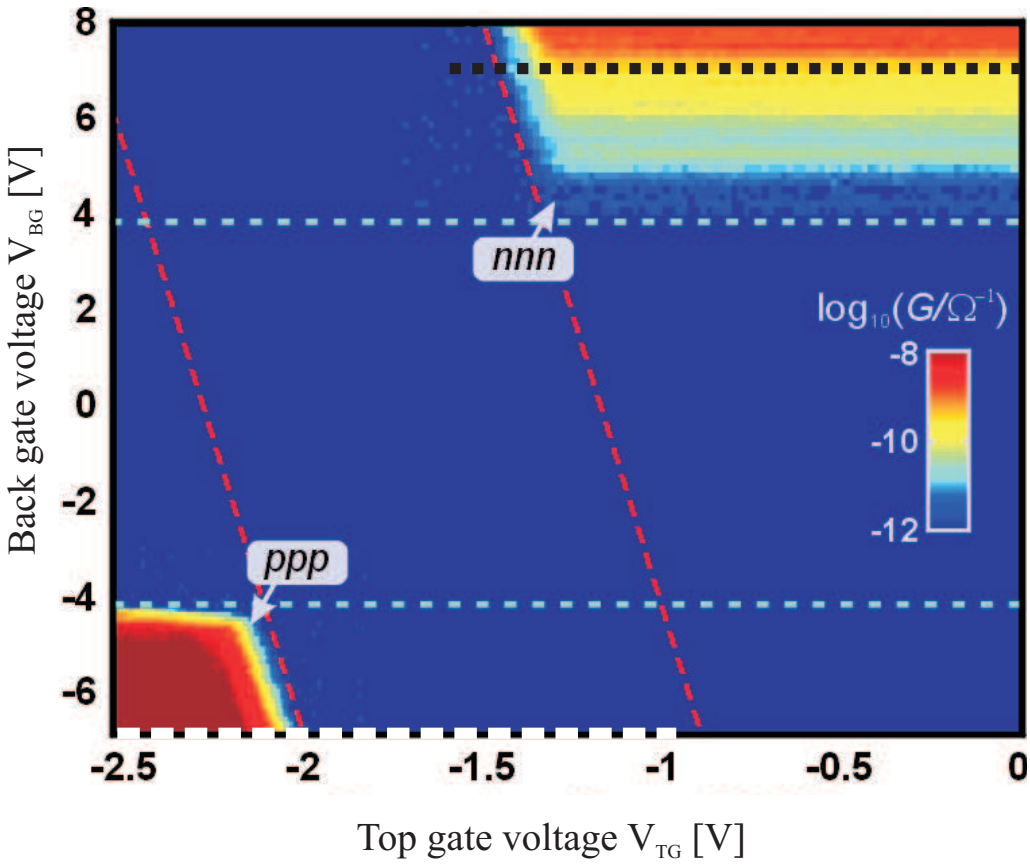

Figure 4.9: Nanotube conductance as a function of back gate (vertical axis) and top gate (horizontal axis). The conductive regions are labels nnn and ppp for the charge carriers responsible for conduction in that region. The dashed blue and red lines are the borders of the bandgap.

refer to this as the nnn region in the conductance plot. In the lower left corner of figures 4.9 and 4.10, the tube is hole (p) doped in all sections by the two gates, and labeled ppp. The upper left and lower right corners have excessively large resistance, because the tube forms an npn or pnp junction, respectively. In the center of the graph, all the sections of the nanotube are in the bandgap, and thus the tube doesn't conduct. Above and below (right and left of) the center, the section under the top gate (between the top gate and the contacts) is in the

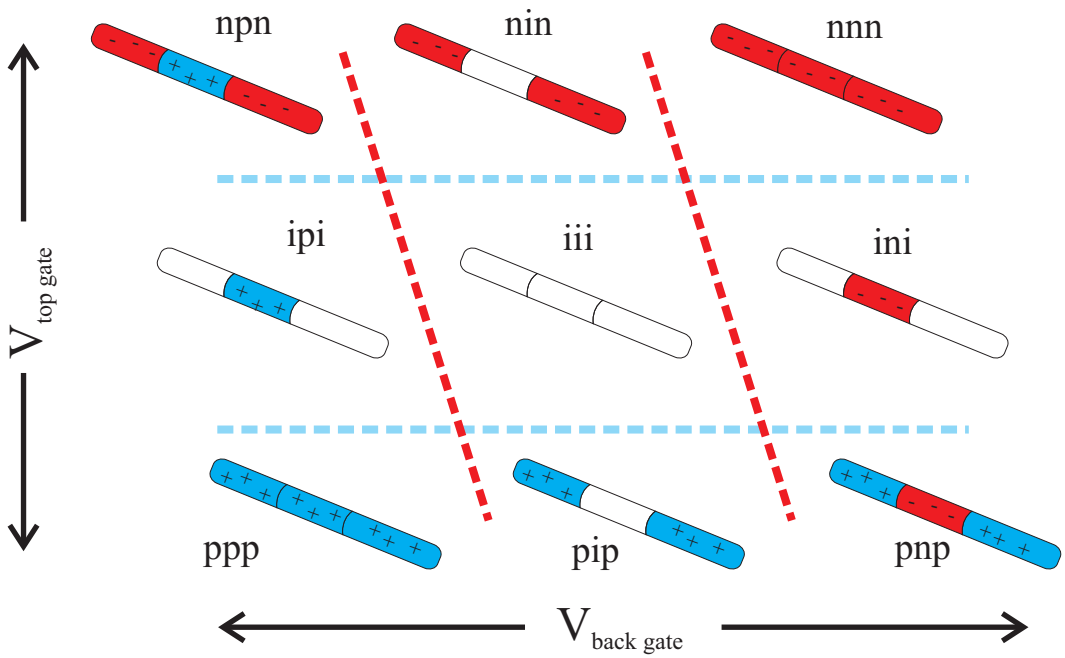

Figure 4.10: Carrier type versus gate voltage for the two gates of figure 4.9. The back gate voltage (on the vertical axis) controls the carrier type of the outer segments of the nanotube. The top gate voltage (horizontal axis) controls the carrier type of inner segment. The gates can vary the segments from hole doped (p for positive) through the band gap (i for insulating) to electron doped (n for negative).

bandgap, and thus the tube doesn't conduct. The device only conducts when both gates dope the nanotube in the same way.

The top gate's influence on the nanotube is limited to the section of nanotube under the top gate. The back gate affects the nanotube in the sections between the top gate and the contacts, and the section under the top gate. The top gate has an oxide thickness of only 10 nm, so the section of nanotube under it couples to the top gate much better than to the back gate with its 200 nm of oxide. We quantify this by further analysis of figure 4.9. When the center section of the nanotube is in a conducting state, the borders between the matching con-

ducting and non-conducting states for back-gate voltage (horizontal blue lines) are independent of top-gate voltage. For example, the same back-gate voltage turns the tube conducting at top-gate voltages of -1 V and 0 V. However, the gate voltage where the top gate creates conductance does depend on the back-gate voltage (beyond ppp or nnn requirement). The nanotube begins to conduct at a different top-gate voltage when the back gate is at 6 V or 8 V. The slope of the bounding mostly-vertical red line is 0.04, and gives us the relative strengths of the top gate's and back gate's effect on the center part of the nanotube. We expect the gate's relative strengths to be set by the ratio of their oxide thicknesses. The ratio for the top gate oxide to back gate oxide is $\frac{10\,\text{nm}}{200\,\text{nm}} = 0.05$, which agrees well with our gating ratio of 0.04.

In between the top gate and the contacts, the nanotube is coupled to the back gate, and not well-coupled to the top gate. We'll refer to this part of the nanotube as the nanotube leads, nanotube wires that lead to the section of nanotube under the top gate. The zero slope of the horizontal blue lines marking the back gate transition between conducting and non-conducting demonstrate that the top gate has no effect on the nanotube leads.

The two-dimension conductance plot we've mapped out here gives us information about the bandgap and where to look for capacitive contributions. The back-gate's ability to make the nanotube leads not conduct is important, because we will use it to isolate the nanotubes contribution to the capacitance signal in section 4.5.

4.5 Isolating the nanotube's capacitance

We now look at how the nanotube's conductivity as a function of back-gate voltage helps us measure the nanotube's capacitance. Figure 4.11 shows the results of a capacitance measurement of the system after all the above precautions and minimizations of stray capacitance have taken place. The capacitance is being measured between the top gate and both electrical contacts (the source and drain for conductance measurements are both connected to one side of the capacitance bridge). It is measured as a function of back-gate voltage. As the back-gate voltage reaches -4 V, there is a change in the measured capacitance.

The most important number in figure 4.11 is the difference between the two flat regions of capacitance. The capacitance on the left is when the entire nanotube is conductive. The capacitance on the right is when the nanotube leads are not conducting. By making the nanotube's leads non-conductive, we've removed its capacitance and isolated the tube's contribution from the background capacitance of the system.

The following is a more in-depth discussion of the analysis, including the numerical values involved. The upper left corner of figure 4.11 shows a capacitance of 520 aF. The measured 520 aF is at gate voltages of -6 V on the back gate and -2.5 V on the top gate. The nanotube is solidly in the bottom left corner of figure 4.9, in the ppp region. The nanotube leads and the section under the top gate are p-doped and the entire tube conducts. As we move to the right in figure 4.11, the capacitance drops when the back gate is at -4 V, settling on a value of 330 aF. This is the same back-gate voltage we expect the tube to stop conducting at from figure 4.9. The top gate is still at -2.5 V, and thus the sec-

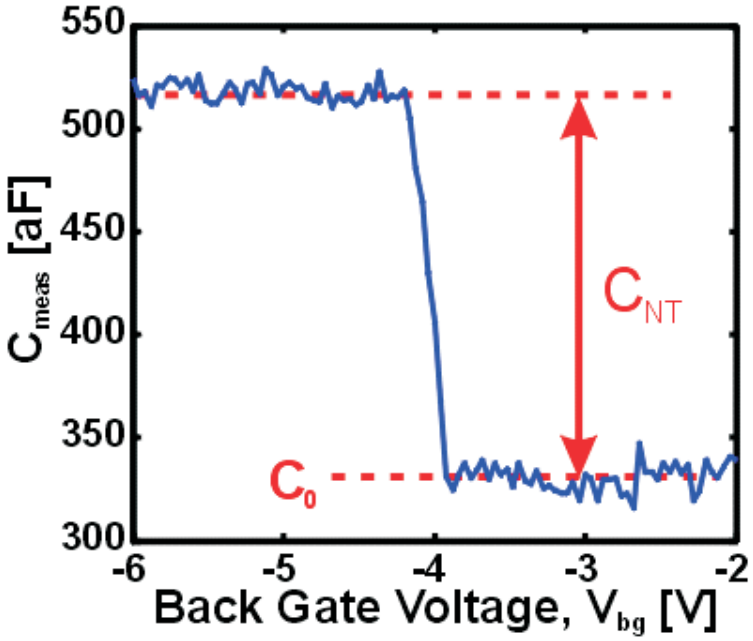

Figure 4.11: Capacitance plotted versus back-gate voltage. The decrease in capacitance as the nanotube leads go non-conducting highlights the nanotubes contribution to the capacitance. Measurements made at 77 Kelvin, top-gate voltage -2.5 V.

tion of nanotube under the top gate could still conduct; but the center section of the nanotube under the top gate has been isolated from the source and drain electrical contacts by non-conducting nanotube leads. The Fermi energy of the nanotube leads is inside the bandgap. Charge can no longer move onto the nanotube. Since charge can't move onto the nanotube, the capacitance of the nanotube has been removed. The 330 aF capacitance value at the bottom right is the background capacitance of the system (like the metal to metal capacitance not completely shielded). The 190 aF difference between the 520 aF capacitance when the nanotube conducts and the 330 aF capacitance when it does not conduct is the capacitance of the nanotube to the top gate.[6]

[6]Nominally the capacitance between the top gate and the nanotube will include the capacitance between not just the top gate and the section of nanotube underneath the top gate, but

We have thus demonstrated that with shielding, cryogenics, a capacitance bridge, and back-gate isolation, we can determine the capacitance of an individual carbon nanotube. The measured capacitance is as expected from our simple model. We performed this measurement on multiple samples. The results are below, showing the expected correlation between capacitance and length of nanotube.

4.6 Capacitance as a function of length

We expect the capacitance of a carbon nanotube to scale linearly with its length. The previous section showed how we measure the capacitance between a nanotube and a top gate. As seen in figure 4.1, we can measure the length of the nanotube underneath the top gate. We thus have a capacitance and its corresponding length value for a nanotube.

We repeat the capacitance measurement described in section 4.5 for several different nanotube devices of different lengths. We then plot the capacitance of the nanotubes versus their length, as seen in figure 4.12. Each point represents a difference measurement between capacitances with the tube conducting or not conducting and the length of nanotube under its top gate.

The red lines are the theoretical values, for different diameters, predicted by the model discussed in section 4.3, figure 4.2. This simple model neglects the contributions from the density of states, a small correction we'll examine

also the nanotube sections in between the top gate and the electrical contacts. However, the zero slope in top-gate voltage of the transition between conducting and non-conducting as a function of back-gate voltage demonstrates the top gate has very little coupling to the parts of the nanotube not directly underneath it.

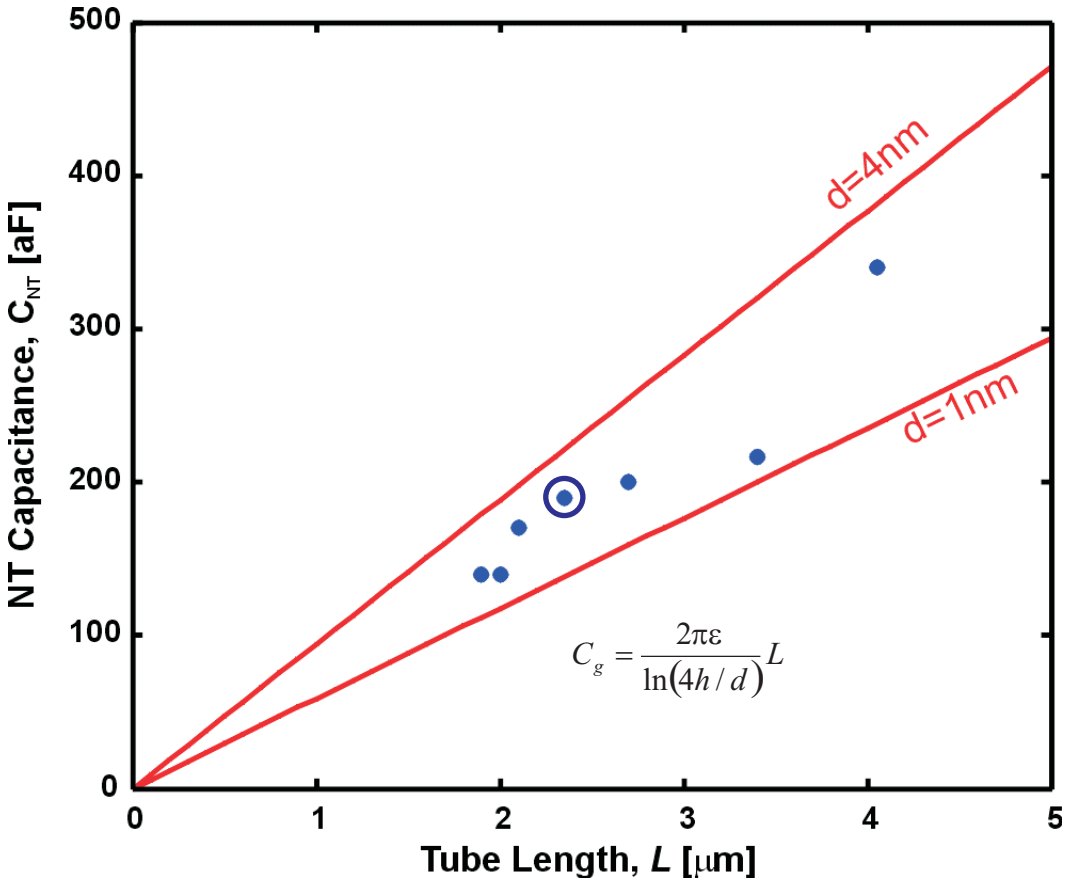

Figure 4.12: Capacitance of carbon nanotubes as a function of length. Each point is a capacitance measurement like figure 4.11. The lines are from the simple model of a conductor imbedded in a dielectric. Measurements made at 77 K. The circled point is the 2.5 nm tube that the previous conductance figures came from.

in the next section. As expected, the measured capacitances for the nanotubes increases as the top-gated length increases. Our values are bounded by the theoretical values for our expected nanotube diameter ranges.

The circled data point in figure 4.12 is the 2.5 nm diameter tube the conductance measurements of section 4.4 and the capacitance measurements of section 4.5 came from. Because the capacitance of a wire depends on the diameter of the wire, ideally we would have the diameter measurements of all the samples

shown in figure 4.12. Unfortunately, the photoresist residue on some of the tubes prevents accurate diameter measurements. AFM of other tubes grown from the same catalyst using the same recipe were between 1 and 4 nm, as were the tubes for this experiment that we were able to directly measure. The measured capacitance per unit length for these samples is as predicted by our basic theory. In the next section we will look more closely at the capacitance of the highlighted sample to see the structure from the density of states.

We have shown that the capacitance of the nanotube matches what we expect from basic electrostatic theory. We can also see that the noise floor on our measurement is small enough to discern changes on the order of 10 aF, so we can look for density of states induced structure in the capacitance.

4.7 Capacitance as a function of top-gate voltage

We've successfully measured the capacitance of a carbon nanotube, using the back gate to isolate the nanotube's contribution. We are now going to look at the nanotube's capacitance as a function of top-gate voltage as a way of investigating the band structure of the nanotube.

Figure 4.13 shows the capacitance of the nanotube as a function of top-gate voltage. The curve in red is at back-gate voltage of +7 V. The curve in green is at back-gate voltage of 0 V. The green curve is from when the nanotube leads are in their bandgap, and the capacitance of the nanotube has been shut off, as in section 4.5. For the red curve, the back-gate voltage of +7 V means the nanotube leads are n-type and conductive.

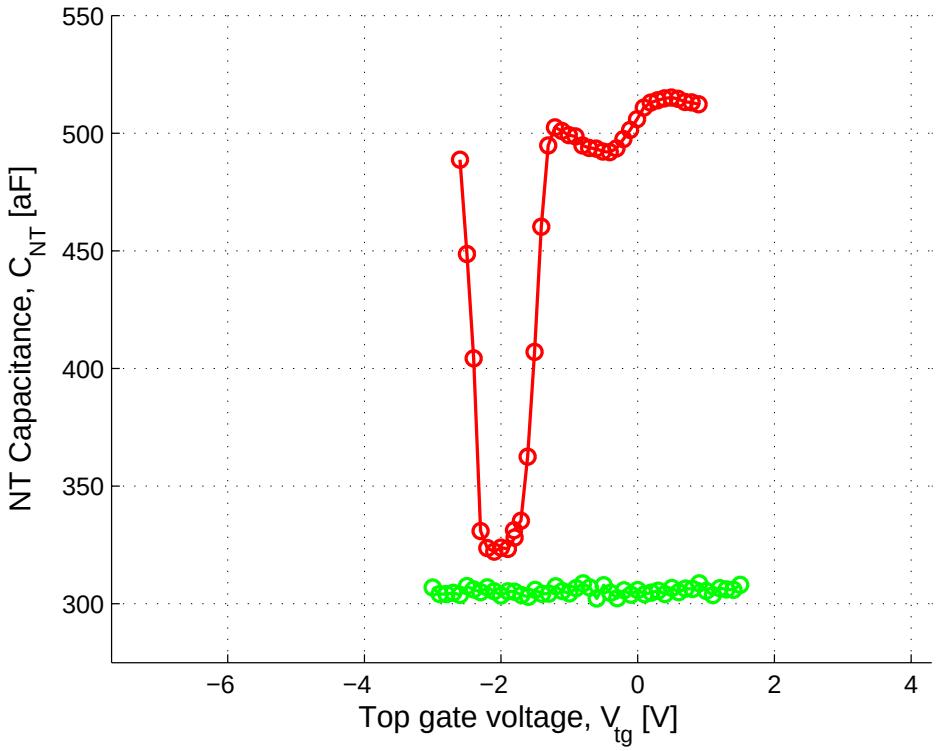

Figure 4.13: The capacitance of a tube versus top-gate voltage with back gate at +7 V (red) and 0V (green).

The dip in the red curve, around $V_{TG} \sim -1.5$ V, occurs when the nanotube segment under the top gate goes through the bandgap. The total change in capacitance of the dip is almost the same as the total capacitance from when the leads are taken through the bandgap, as in section 4.5. The left side of the red curve, $V_{TG} < -2$ V, occurs when the top-gated section is p-type, and the tube is npn. The right side of the curve, for $V_{TG} > 1$ V, occurs when the nanotube leads and the center section are all n-type, for an nnn tube.

In the nnn region ($V_{TG} > -1$ V), we see two peaks in the capacitance. The left side of each peak has a larger slope than the right side of each peak. The capacitance rises quickly, and then slowly decreases as the voltage is increased.

The second peak on the right has a height of 15 aF, rising in half a volt. It only drops 5 aF in the half volt after the peak. The first peak height is difficult to determine because it convolutes with the bandgap, but its right side drops 10 aF over 1 V, a similar rate to the drop of the second peak. The asymmetric structure of these peaks is what we expect to see from the van Hove singularities, as discussed in section 4.2. In section 4.9, we'll explicitly compare our data with the theoretical predictions.

In the npn region at a back-gate voltage of +7 V, and a top-gate voltage less than -2 V, the capacitance of the nanotube starts to turn back on from the dip. It is worth noting that the device has a very low conductance at these combined gate voltage values (see figure 4.9), lower than the threshold of the Ithaca pre-amp measuring current. The sensitivity of the capacitance bridge is such that it can measure the charge movement on and off the central segment of the nanotube, through np junctions between the leads and the top-gated section. The ability of the capacitance bridge to extend measurements past where the conductance has become incredibly low is part of the utility of the capacitance measurement.

Although we see the dip in the capacitance of the nanotube as the central section is moved through the bandgap, the data we've presented shows peaks on only one side. Leakage between the gates prevents us from taking the top-gate voltage far enough into the p region to see the other peaks when the back gate is n doping the nanotube leads at +7 V. We can, however, measure the capacitance as a function of top-gate voltage with the back gate at -7 V, where the nanotube leads are n-doped.

Figure 4.14 shows the capacitance as a function of top-gate voltage for back

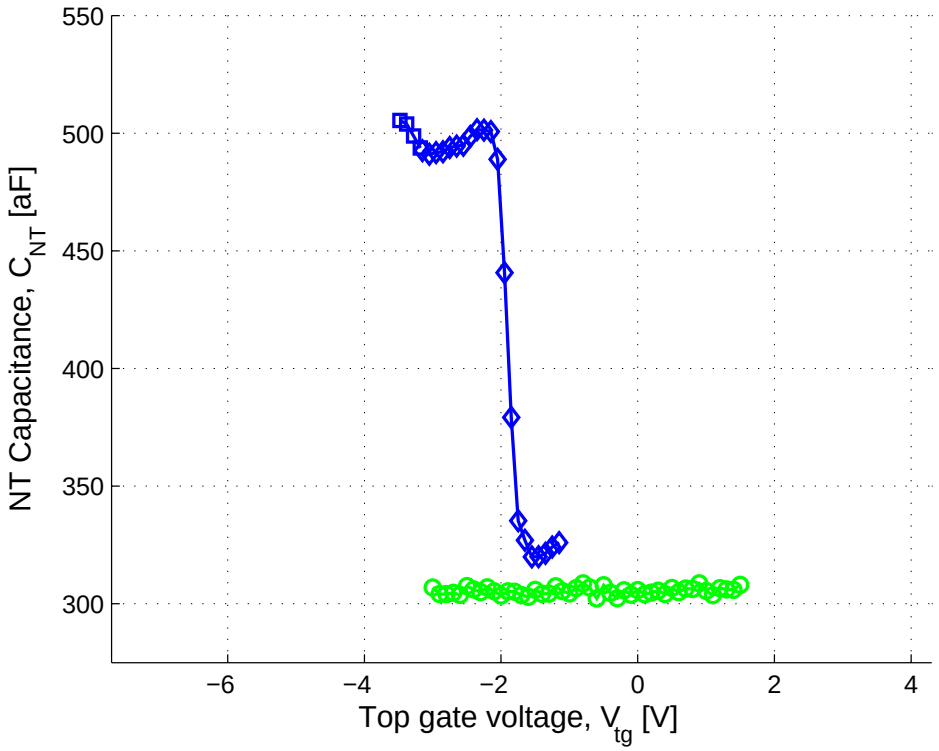

Figure 4.14: The capacitance of a tube versus top-gate voltage with back gate at -7 V (blue) and 0V (green).

gate at -7 V (blue), and the reference back gate 0 V curve (green). The nanotube leads are p-doped, and the central section of the tube goes from p to n. We again see the dip in capacitance as the tube enters the bandgap. The peak as the tube's conductance turns off is asymmetric. At top-gate voltage of -3.5 V, we see the start of another asymmetric peak that looks like the second peak we saw in figure 4.13. The structure of the capacitance for a p-doped tube is a mirror image of the structure for an n-doped tube, except our data doesn't extend as far out on the p-side.

We have less data for the tube when the leads are p-doped. The full shape of the second asymmetric peak (V_{TG} < -4V) is not measured because it exceeds

the voltage we can take our top gate to without driving a leakage current from the top gate to the nanotube. The blue curve in figure 4.14 stops at V_{TG} = -0.5 V. In this region, the tube is now pnp and the pn junction resistance is so large the nanotube can't completely charge on the time scale of the oscillating AC voltage.

The bottom of the dips in figures 4.13 and 4.14 do not have the same capacitance value as the green curve. In the green curve, the back-gate voltage of 0 V places the Fermi energy of the nanotube leads into the bandgap, and so the leads do not conduct. In the dip in the red and blue curves, the top gate moves the Fermi energy of the center section through the bandgap, so the center doesn't conduct, but the leads are still conductive. With figure 4.9, we discussed that the top-gate voltages where the tube conducts depend on the back-gate voltage; whereas the back-gate voltages the tubes turn on do not depend the top-gate voltages (beyond requiring the same type of doping). This means that when we attempt to move the center section of the nanotube into its bandgap while having the leads remain conductive, a small section of nanotube near the edge of the top gate still conducts and capacitively couples to the top gate. The 17 aF difference between the bottom of the dip and the green curve comes from both edges of the top gate coupling to a section of the nanotube not completely turned off. The measured 61.5 aF/um for this device tells us there is roughly a 130 nm interface region on both sides of the top gate where the back gate dominates the Fermi energy, but the top gate still capacitively couples to the nanotube.

Having looked at the separate features of figures 4.13 and 4.14, we can create an aggregate image of the capacitance on both sides of the bandgap by joining these curves into figure 4.15. Here we see a symmetric set of features around

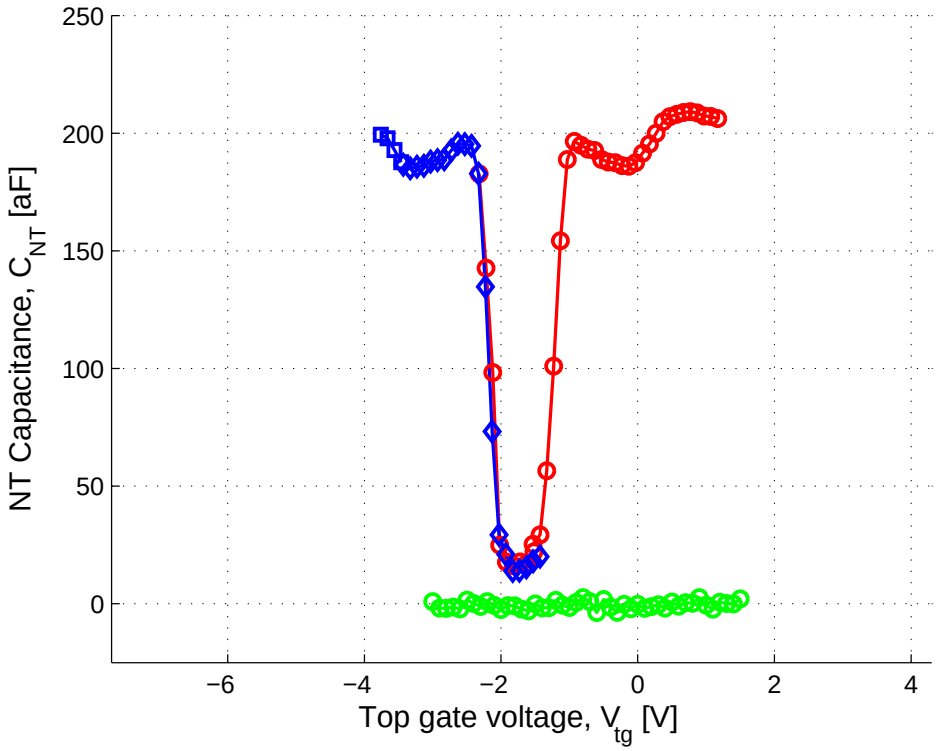

Figure 4.15: The capacitance of a tube versus top-gate voltage, combining the previous curves. Back gate at +7V (red), -7V (blue), and 0V (green). The background capacitance has been subtracted off to place the green curve at zero. The top-gate voltage values have been shifted to account for differences in back-gate voltage (see text).

the bandgap for capacitance as a function of top-gate voltage. The dip in the capacitance corresponds to the bandgap of the nanotube, and correlates with where the conductance of the tube turns off. The offset background capacitance has been subtracted off for this curve, such that the green curve is at zero, to see how the fine structure compares to just the electrostatic capacitance of the nanotube. The nanotube's capacitance to the top gate is 200 aF, and has 20 aF structure corresponding to the van Hove peaks in the density of states.

An important note for figure 4.15: when combining our capacitance curves,

shifts were applied to the top-gate voltage values. The top-gate voltages do not directly align because the curves were taken at different back-gate voltages. In the conductance graph in figure 4.9, we saw that the slope of the near-vertical lines was 0.04, implying a 0.04:1 ratio in the coupling of the back gate to top gate for the section of nanotube under the top gate. To properly plot the two capacitance versus top gate curves on the same graph, the values need to be corrected for the applied back-gate voltages of ±7 V. This ±0.28 V shift was applied when the curves were plotted together in figure 4.15.

4.8 Prediction of theory

Here we further develop the theory put forth in section 4.2 to compare it with our experiment. We derived that the capacitance of a carbon nanotube should reflect the band structure of the nanotube. The turning off of the nanotube's capacitance is a large scale result of the band structure. Figure 4.16b shows a prediction for what the fine structure from the density of states would look like. However, the horizontal axis of that graph is in Fermi energy, not gate voltage. To compare the theory with our data, we need to convert Fermi energy into gate voltage. We also need to take into account the finite temperature of the experiment.

To relate the Fermi energy to top-gate voltage, we look at how a change in one affects the other, which is to say the derivative of the Fermi energy with respect to the top-gate voltage, $d(E_F/e)/dV_{TG}$. We use equations 4.4 through 4.6 to show:

$$\frac{d(E_F/e)}{dV_{TG}} = \frac{d(E_F/e)}{d(\mu_{ec}/e)} \cong \frac{d(\mu_c/e)}{d(\mu_{ec}/e)} = \frac{d(\mu_c/e)/dq}{d(\mu_{ec}/e)/dq} = \frac{C_{DoS}^{-1}}{C_{Total}^{-1}} = \frac{C_{Total}}{C_{DoS}} = \alpha. \tag{4.9}$$

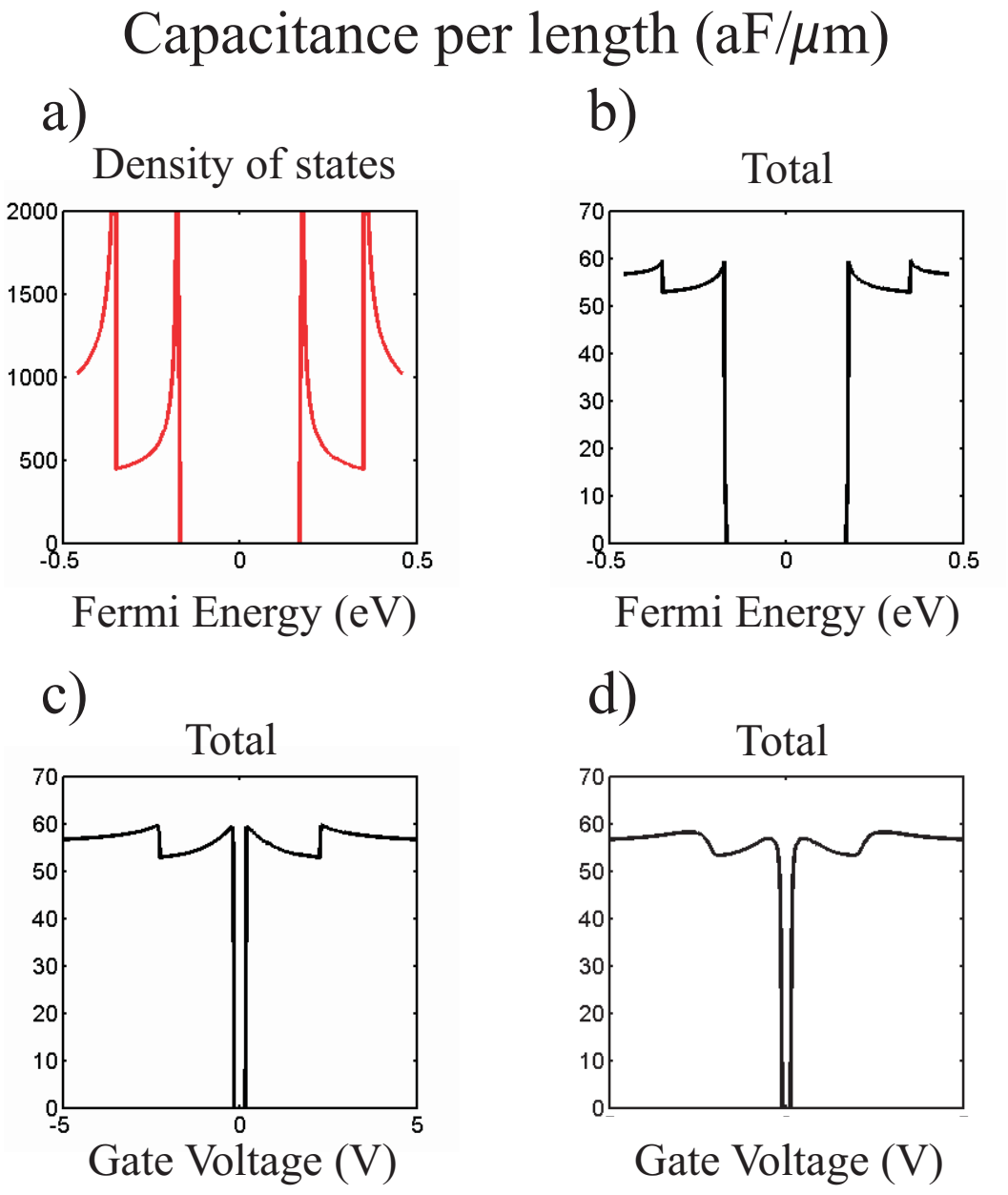

Figure 4.16: Capacitance per length (aF/μm) as a function of Fermi energy (eV) and gate voltage (V) for a tube embedded in silicon oxide. a) Density of states capacitance versus Fermi energy. b) Total (density of states plus geometric) capacitance versus Fermi energy. c) Total capacitance versus gate voltage. d) Total capacitance versus gate voltage, smeared with temperature (77 K).

This depends only on the capacitances of the system. Since the capacitance characterizes the charge movement in response to voltages, it makes sense that ratios of capacitances would be a succinct way of writing relationships between the voltage of the system and the energy of the system of charges. We'll call $d(E_F/e)/dV_{TG} = C_{Total}/C_{DoS} = \alpha$, and look at how α lets us convert between E_F and V_{TG}.

The change in the Fermi energy is the change in voltage times α. Inside the bandgap, the total capacitance of the system and the capacitance from the density of states are zero. α, the ratio between them, is one (they go to zero at the same rate, defined by C_{DoS}). $\alpha = 1$ means the Fermi energy exactly tracks the voltage inside the bandgap, a change of 0.01 V in voltage maps to a change in 0.01 eV in the Fermi energy.

The edge of the bandgap has a van Hove singularity. At that singularity, $\alpha = 0$ because C_{DoS} is infinite and C_{Total} is finite. A change in gate voltage has no effect on the Fermi energy at that point, it only affects the charge population. Continuing through the van Hove singularity into the long tail, α goes from zero to around one tenth. Changing the electrochemical potential again affects the Fermi energy, but not as much as inside the bandgap.

At the edge of every band $\alpha = 0$. As more and more bands add in, the total capacitance gets closer and closer to the electrostatic capacitance because the C_{DoS} gets larger and larger. α has a decreasing maximum as each new band is added in. As more electrons are added to the system, changing the voltage of the system has a smaller and smaller effect on moving the Fermi energy.

The capacitance will have a dip in voltage space corresponding to the

bandgap. Outside the bandgap, the features plotted versus gate voltage are spread out compared to the features plotted versus Fermi energy. Figure 4.16b is a plot of C_{Total} versus Fermi energy and 4.16c is versus gate voltage.

Our experiments were conducted at 77 K, so the electrons in the system had thermal energy to smear out features. The temperature smearing of C_{DoS} at chemical potential μ_c and temperature T is given by

$$C_{DoS}(\mu_c, T) = \int d\mu_c' f'(\frac{\mu_c - \mu_c'}{k_B T}) C_{DoS}^o \sum_{j=-2}^{2} \frac{1}{\sqrt{1 - (E_j/\mu_c')^2}}, \tag{4.10}$$

where $E_j = \hbar v_F \frac{2j}{3d}$ is the energy of the van Hove singularities, $C_{DoS}^o = \frac{4e^2}{\pi \hbar v_F}$ is the capacitance quanta, $v_F = 8 * 10^5$ m/s is the Fermi velocity in nanotubes, f' is the derivative of the Fermi function, and d is, as usual, the diameter[46]. Just the theoretical curve is plotted in figure 4.16d. We use $C_{Electrostatic}$ = 61.5 aF/μm and d = 2.35 nm, for our theory curve to fit the data. The fit and comparison are discussed in the next section.

4.9 Comparison of model to experiment

Figure 4.17 shows our experimental capacitance data and the theoretical model's predictions. Both our experiment and the model have a dip in the capacitance caused by the bandgap of the nanotube, and undulations on the sides of the bandgap from the density of states.

Our theoretical model is applicable to any semiconducting tube. To make quantitative comparisons between our data and the theory's predictions, we fit the theory to the data. The alignment of the bandgap for the data and the theory is made by setting the voltage of the minimum capacitance from the data as the

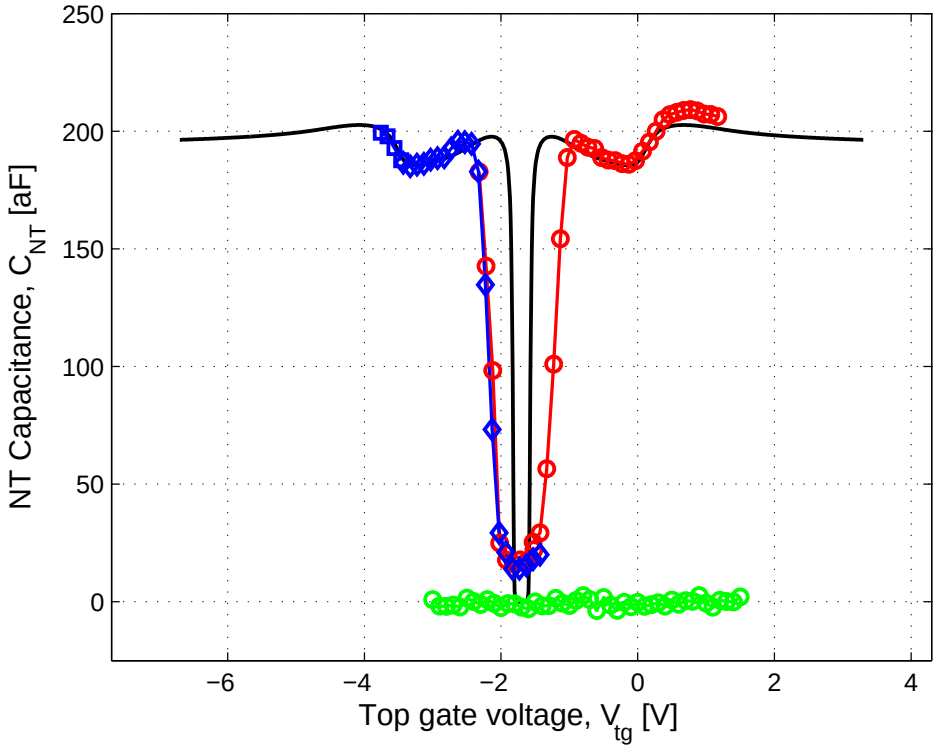

Figure 4.17: Capacitance of nanotube as a function of top-gate voltage. Red is back-gate voltage of +7 V. Blue is back-gate voltage of -7 V. Green is back-gate voltage at 0 V. Black is the theory curve. With the nanotube disconnected (V_{BG}=0V, green), the tube doesn't contribute to the capacitance, and the background capacitance is subtracted off. The red and blue curves are adjusted by +/-0.28 V to account for the back gates +/- 7 V * 0.04 shift described earlier. Measurements made at 77 K.

center of the bandgap. C_{DoS} is a function of gate voltage and the diameter of the nanotube (we showed in section 2.2.4 that the bandgap is a function of nanotube diameter). Matching the model to the data at any point thus specifies $C_{electrostatic}$ that has to be in series with C_{DoS}. We use the geometric capacitance and the diameter of the nanotube as our fit parameters.

We chose to match the model to the experiment at the bottom of the second sub-band. At that point, we're most sensitive to C_{DoS} because it is smallest there,

and C_{DoS} and $C_{Electrostatic}$ are capacitors in series. We choose fit parameters d = 2.35 nm and $C_{Electrostatic}$ = 61.5 aF/μm to line the model up with the data. This compares well with AFM measurements of $d = 2.5 \pm 0.5$ nm and $C_{Electrostatic}$ = 76.5 aF/μm from our simple model of a conductor in oxide.

Having explained our fitting process, we return to comparing the theory's predictions to the experimental data. In between the first and second van Hove singularity, the theory fit lies within the measurement's noise. The location in gate voltage of the second band step predicted by theory lines up with the data. The total change in capacitance as a function of top-gate voltage is in close agreement with the theory prediction, the 17 aF difference between the bottom of the theory curve and the bottom of the data curve was explained in section 4.7. The diameter inferred from the capacitance measurement is within the noise of the AFM measurement.

In figure 4.18, the capacitance data for the holes is mirror-reflected, and not surprisingly[48] seen to match very the data for the electrons very well. Despite the very different conductance seen in figures 4.7 and 4.8, the capacitance measurements for electrons and holes are remarkably symmetrical. The curves have the same height for the first step in capacitance, and the same distance between the edge of the first and second steps in capacitance at band edges. Both curves even have a slight kink in the capacitance between their fourth and fifth points after the first peak. The slight disagreement between theory and experiment between those points may be explained by the same phenomenon that accounts for the discrepancy in the height of the capacitance step at the second sub-band, which is postulated below.

Figure 4.18 shows that our model under-predicts the height of the capaci-

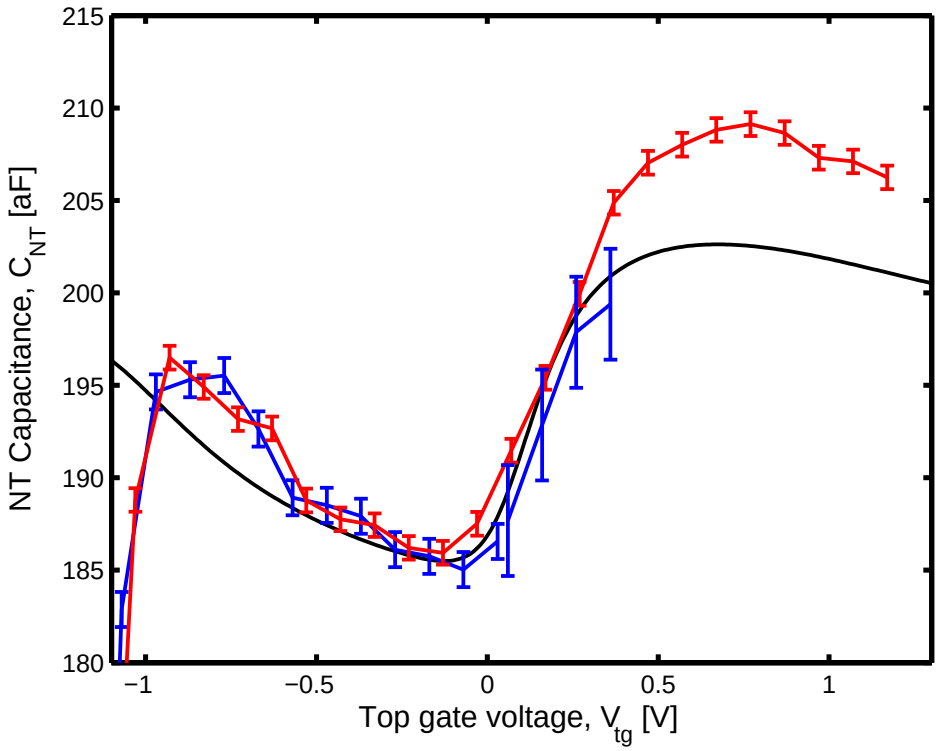

Figure 4.18: The fine structure of the capacitance of electrons (red) and holes (blue), reflected to overlap and compared with theory (black).

tance step at the second sub-band. At the second peak, the black theory curve is 8 aF below the red experimental curve. The black theory curve is also 2 aF below the peak height of the red (electron) and blue (hole) curves in the first sub-band. A possible explanation of the larger than expected step size in our data is another capacitance intrinsic to the nanotube. For instance, the exchange interaction between electrons can be modeled as a capacitance [37], [8]:

$$\frac{1}{C_{Total}} = \frac{1}{C_{Electrostatic}} + \frac{1}{C_{DoS}} + \frac{1}{C_{Exchange}}. \tag{4.11}$$

To create a larger capacitance step in total capacitance, this exchange capacitance would have to decrease the right side of the equation when a new band was added to the system. That means the capacitance $C_{Exchange}$ would be negative,

at least right at the van Hove singularity. References [32], [30], and [64] predict an exchange interaction that provides a negative capacitance at low electron densities (i.e. at the opening of a new band), and that the exchange capacitance decreases with increasing carrier density, and crosses over to positive at high carrier density. Further research into this system would allow fine-tuning of theoretical exchange-interaction modeling.

The other disagreement between our theoretical predictions and experimental data is more obvious but contains less potential for new research. The theoretical model predicts a narrower width for the bandgap. In figure 4.9 we see the conductance of the nanotube. The highly resistive region correlates with the suppressed capacitance in the bandgap. Our capacitance measurements were performed at 1 KHz, which gives us a time constant of 1 ms. The capacitance of the system is order 500 aF (see figure 4.13). A resistance of 2 TΩ and a capacitance of 500 aF gives an RC time constant of 1 ms.[7] For resistance of order TΩ, the capacitance bridge operating at 1 KHz cannot completely charge the nanotube's capacitance, and thus under-reports the capacitance of the tube. This capacitive roll-off could be investigated using a slower frequency measurement. The Andeen Hagerling 2700A capacitance bridge has the capability to investigate capacitance at different frequencies. Unfortunately, the noise floor of the bridge increases away from 1 KHz, so longer times would be required. The system was not stable on the time scales required to accurately measure the wide of the gap unhindered by time constants, but we understand this deviation.

An interesting number we can extract from the difference in widths of our experiment's and model's band gaps is the carrier density at which the tube

[7]The 2 TΩ resistance is the resistance to the nanotube's capacitance, or half the total series resistance through the nanotube.

starts to conduct. The 0.2 V difference between the edge of the first band in the theoretical model and the experimental data, times the expected capacitance of order 200 aF, is roughly 200 electrons (Q=CV implies number=CV/e). The length of the top gated section is 2.1 μm, which means there are roughly 100 electrons (or holes) per micrometer of tube when it starts conducting.

4.10 Conclusions and future directions

We've successfully measured the capacitance of a carbon nanotube. The novel application of a top gate/back gate technique to isolate the capacitance of the nanotube was explained and explored. We have shown that the capacitance per unit length of a carbon nanotube in a dielectric is functionally described by

$$\frac{C_{electrostatic}}{L} = \frac{2\pi\epsilon_o\epsilon}{ln|\frac{4h}{d}|}, \tag{4.12}$$

but that there is more detailed structure.

The capacitance of the nanotube can be used to probe the band structure. The bandgap and van Hove singularities in the density of states show up as features in the capacitance. Our model correctly predicted the overall height of the steps in capacitance from the density of states, as well as the spacing of the steps. We showed that the capacitance and band structure are symmetric for electrons and holes, even in the face of large asymmetries in the conductances for electrons and holes.

Our model under-predicts steps in capacitance at van Hove singularities, indicating the possible existence of exchange-based terms providing negative capacitance. These electron-electron interactions could shed new light on the

physics of one-dimensional systems. To further investigate this, changes could be made to the system or the measurement apparatus.

On the system side, one could look at a number of similar systems with different oxide thicknesses or dielectrics. The top gate provides a screening length for electrons in the tube of order oxide thickness divided by the dielectric constant. Changing the dielectric constant and thickness of the insulating oxide would be a way to manipulate the screening length of electrons in the tube, giving future investigators the ability to look at electron-electron interactions over a range of parameters. New recipes for ultralong tubes [145] raise the possibility of creating several top gates with different oxide-parameters on the same tube, allowing a systematic study of electron-electron interactions. Long tubes also offer the possibility of increasing the size of the signal with wider top gates. On the measurement apparatus side, the sensitivity can be increased in various ways. Low- temperature electronics that allow single electron detection[1] would give a better measure of charge moving in and out of the nanotube.

This technique has already been applied to similar systems like semiconducting nanowires to measure the capacitance [124]. Semiconducting nanowires offer some of the same interesting electronic properties and nanoscale applications as carbon nanotubes, and capacitance measurements will be important for their characterization and utilization.

From an applications standpoint, carbon nanotubes have been proposed as chemical sensors based on capacitance measurements of the tube [112], [111]. We hope that this work proves useful to the realization of these devices and their potential applications.

Another promising area for nanoscale electronics is graphene sheets and ribbons. Research involving graphene sheets has exploded in the past few years [31] thanks to novel fabrications techniques [84]. This capacitance technique can be useful to compare theory [29] [34] and experiment [56] [31] for the capacitance, conductance, and mobility of graphene ribbons. This provides an exciting tool to investigate graphene and how the electron's behavior in similar 1D and 2D systems compare, including the gradual increase of a 1D system to the 2D regime.

CHAPTER 5

LOCALIZED PLASMA DAMAGE OF CARBON NANOTUBES

5.1 Introduction

This chapter describes the quest to create a carbon nanotube with controlled, localized damage. Our eventual goal is to create the structure seen in figure 5.1, where a hole has been cut into a carbon nanotube. The ability to create the structure in 5.1 would open up several interesting possibilities that we'll discuss briefly (section 5.2) before moving on to how we've approached doing so (section 5.3) and the success we've had (sections 5.4-5.7).

Previous groups have used oxygen plasma to completely cut through tubes [35], and gas-phase etching has been used to selectively destroy nanotubes based on diameter [142], and conductivity [141]. It's also possible to create very small defects in nanotubes with current pulses from an atomic force microscope [91] (which will be discussed more in chapter 6). The process we present uses an oxygen plasma and a semi-protective layer to partially cut into the nanotube. The conductance of the tube is changed, but not completely destroyed,

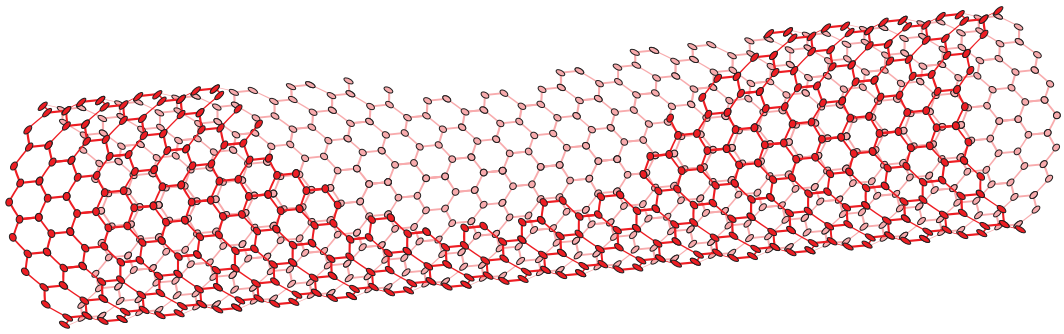

Figure 5.1: A hole cut into a nanotube

and holes on the order of 10s of nanometers long are opened. This damage is visible in atomic force microscopy, and affects the nanotube's sensitivity to local electric perturbation.

5.2 Motivation

It is roughly four orders of magnitude more difficult to split nanotubes than it is to split hairs, but there are some very interesting applications that could make the effort worthwhile.

Cutting a large scale controllable hole into a carbon nanotube could allow the fabrication of graphene nanoribbons prewired with nanotube contacts. There has been a great deal of interest in graphene nanoribbons, both theoretically [29], [34], [136], [127], [113], [126], [125]; and experimentally [56], [56], [39], [16]. Forming a nanoribbon from a nanotube would allow for the study of interfaces between quasi one-dimensional systems, edge effects on the conductance of nanoribbons, and undoubtedly more. While there has been some work converting nanotubes to graphitic ribbons [36], this work is another pathway to possible device fabrication.

A potential application of a hole in the tube is that it heightens the tube's electrical potential sensitivity, making a better detector. Various work has been done using a nanotube as a chemical detector for gases [101], [58], [62], [117] and biologically relevant in-fluid detection [115], [9], [14], [12], [66], [129], [135] . Deliberate, localized damage leaves dangling bonds and defects that could provide more sensitivity to changes in the local environment, making controllably damaged tubes better sensors.

Another possible application is targeting the dangling bonds created by the damage to the nanotube for bonding of external molecules. The regular, closed repeating cell structure of the honeycomb carbon lattice would be interrupted with bonding sites at controlled locations. Functionalized chemical groups could be attached at these sites, avoiding the problem of nonspecific binding current nanotube sensors have [15]. Controllable damage could lead to a tailor-made active chemical group in a predefined location on a one-dimensional conducting wire. For instance, if a DNA base pair were attached to the damage section of the carbon nanotube, the conductance of the tube could be monitored while flowing complementary DNA base pairs past the nanotube (similar to [116] but with better coupling). Bonding between the base pairs would cause the tube's conductance change because the new molecule would change the tube's local electrostatic environment. The functionalized damaged nanotube would be both a detector and an investigative tool into the bonding between groups.

One promising application of carbon nanotubes is for arrays of them to be used as a storage for hydrogen [25], [148], [21], [41], [82]. Hydrogen adsorbs inside of CNTs and along their surfaces. Small perforations in the tubes could allow for faster loading and unloading of hydrogen, as well as a larger filling fraction for the interior of the tube. This would come at a fractional loss of space along the outer surface.

Previous research work has looked at molecules ([60], [70]) and liquids ([13], [131]) inside of carbon nanotubes. It has been established that these molecules and liquids can move inside of nanotubes. A long nanotube with holes cut into it at different locations could serve as a nanopipeline. Figure 5.2 is a schematic

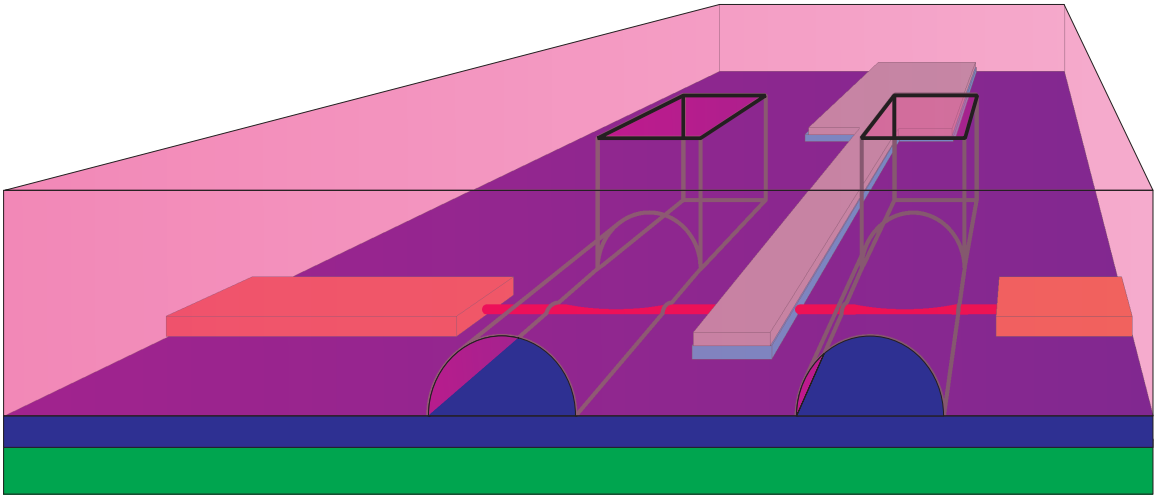

Figure 5.2: Schematic for a potential nanofluidic system. The damaged nanotube is shown in red. It has two electrical contacts (orange) and runs under a local top gate with metal (grey) on oxide (light blue). The transistor sits on top of silicon dioxide (blue) and a back gate (green). The system is embedded in a polymer with microfluidic channels (magenta). The damaged carbon nanotube creates a controllable nanopipe with electrical probes that links the microfluidic channels.

representation of an ambitious future device. A damaged tube is depicted connecting two different microfluidic reservoirs and passing under a region that could gate the tube (as in chapter 4). The holes in the tube would allow entry and egress of molecules to and through the tube. Electrical contacts outside the cut area would allow conductance measurements and application of an electric field along the tube. A local top gate would provide an additional knob for investigating the tube, possibly affecting the flow of molecules through the tube. Pressure differentials in the reservoirs and/or the electrical potential across the tube would also affect flow. The electrical aspects would not be available if the tube were completely cut, and were just a simple straw between reservoirs.[1]

[1]Its conceivably beneficial to have the openings in the tube between the electrical contacts, as shown in figure 5.2, rather than having electrical contacts between the holes. The second scenario would be possible by putting contacts midway along a tube and then cutting the ends

The partially damaged nanotube could serve as a pipe, wire, flow control, and sensor rolled into one. While the throughput flow of a single nanotube would be very, very small; recent work has described how to make arrays of aligned nanotubes [55] with a narrow range of diameters and electrical properties [26]. These arrays could be used to form parallel channels of nanotube pipelines to increase throughput in the above proposal. The desired throughput of the system could then just be scaled by the number of tubes in running in parallel, giving a knob for a nanofluidic system.

5.3 Fabrication

We want to enlarge the toolbox of nanotube manipulation [61] to create the structure of figure 5.1. The initial fabrication for the devices in this chapter is mostly as described in chapter 3. That process gives us nanotube transistors with two electrical contacts. We use the space between the electrical contacts for the lithographic steps to damage the tube.

We begin by outlining the additional fabrication steps, and then provide additional detail in the following subsections. We'll use a layer of aluminum oxide to protect part of the tube, and damage part of the tube with an oxygen plasma, leaving a opened conducting nanotube. Figure 5.3 steps through the process: Fabrication for this experiment begins with a regular nanotube transistor, 5.3a. Photoresist is put down and a trench over the tube is opened, 5.3b. A thin pro-

open. This would be a simpler fabrication technique, and would be worth investigating if one was solely interested in nanofluidics. Possible benefits of figure 5.2 are having the electrical contacts outside the damage allows for field gradients across the openings to attract molecules, and it removes the complication of moving molecules through a tube covered with metal, which may change the flow properties.

tective layer of aluminum oxide is deposited at an angle (5.3d), such that the nanotube's shadow prevents part of the tube from being covered (5.3e). The device is put in an oxygen plasma, 5.3f, which etches away some of the exposed section of tube. The aluminum and photoresist is removed (5.3g) leaving a conducting nanotube transistor with holes, 5.3h.

5.3.1 Angle deposition of aluminum oxide

This section describes figure 5.3b-e in greater detail. While nanotubes have been used to shadow mask nanogaps [94], we're seeking here to have the nanotube shadow mask itself. The desired mask to partially protect our nanotube is shown in figure 5.4. This is an axial view of the nanotube that shows a partial covering of a protective layer, and a small amount of exposed tube that can be damaged by an oxygen plasma. The contacts and photoresist of 5.3 are not shown here.

P20 and Shipley 1805 were spun onto the wafer pieces. The 5x g-line stepper at the CNF was used to open a window in the resist, see figure 5.3b. This lithographic step is not image reversed. The photoresist profile does not have an overhang, but instead slopes down from full thickness to no resist.

After exposing and developing the window in the resist, we deposited a very thin layer of aluminum at an angle onto the device. The wafer was put onto a rotating stage such that the axis of rotation was parallel to the axis of the carbon nanotube. The chip's surface-normal was at 85° to 88° to the angle of evaporation, a very high grazing angle for deposition. This is so that one side of the nanotube would shield the other side in the deposition, creating a self

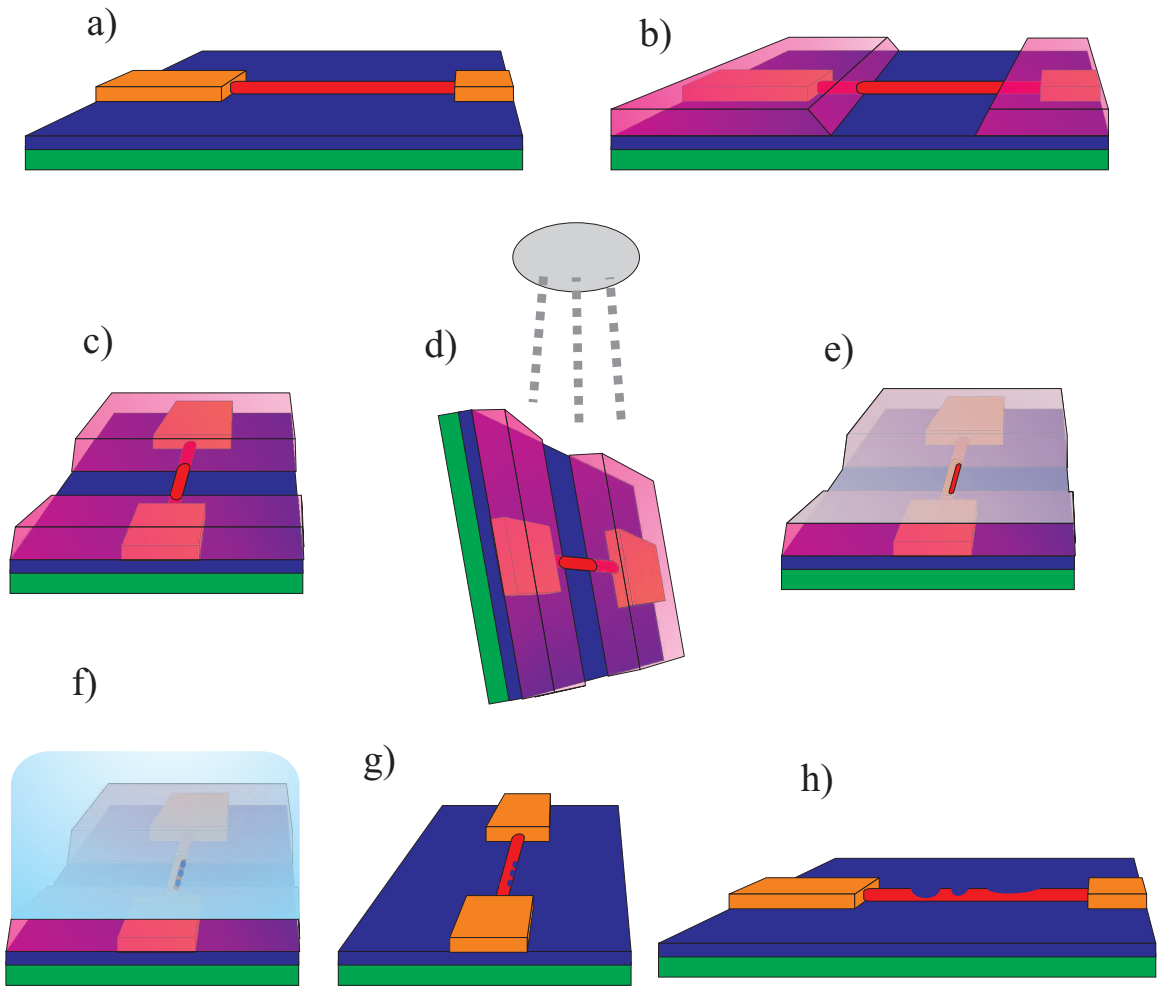

Figure 5.3: Outline of the fabrications steps for localized plasma damage of a carbon nanotube. a) A nanotube transistor, as in chapter 3. b) An opened trench in a photoresist layer. c) Rotated view of b). d) Angle deposition of aluminum protective layer. e) A thin layer of aluminum covers everything but part of the tube. f) Plasma (blue) burns exposed part of nanotube. g) Aluminum and photoresist are removed, leaving a CNT transistor with holes cut into it. h) Initial viewpoint of device after fabrication.

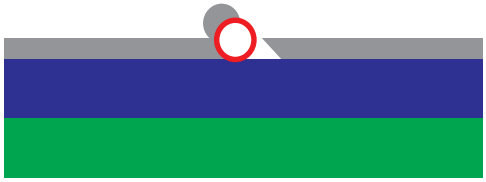

Figure 5.4: Tube-axial view of desired self shadow mask of nanotube (red) with aluminum oxide (grey), on the standard wafer with silicon dioxide (blue) on doped silicon (green). Contacts and photoresist have been left off for clarity.

shadow mask as in figure 5.4.[2]

Before (and during) deposition, the stage and chip were cooled to below 100 K by running liquid nitrogen through a reservoir in the back of the stage. Cooling took about an hour, and required a constant feed of liquid nitrogen. After cooling down, 1 to 2 nm of aluminum was deposited at 0.3 Å/s. The cooling ensured that the thin layer of aluminum would not have the mobility to transition from a thin film to isolated clumps. After deposition, the sample was left to warm for a few minutes, then the chamber was filled with 50 mT of O_2. Since aluminum forms a native surface oxide over 2 nm thick, the aluminum layer converts completely to aluminum oxide (checked by measuring that there was no conductivity through that layer).

5.3.2 Nanotube catalyst

The size of the opening in figure 5.4 is dependent on the angle of deposition and on the diameter of the nanotube. We deliberately chose a catalyst that gave

[2]The deposition was performed with the same rotatable stage, figure 3.8, used in fabricating the self-aligned top gate in 3.6.

larger nanotubes to make it easier to create this geometry. Larger tubes give a larger opening for the oxygen plasma to attack. Larger tubes also allow for a thicker layer of deposited oxide without being completely buried. Completely buried tubes are less likely to be asymmetrically affected by the plasma.

The catalyst used here was chemically synthesized iron nanoparticles suspended in hexane. This is different from the general fabrication described in chapter 3 where we used evaporated iron. These slightly larger catalyst particles produced, on average, slightly larger nanotubes, including a larger percentage of double or small multi-wall tubes. The same gas flow parameters were used for growth. Slightly larger catalyst pads (4 μm by 8 μm) offset the lower yield of this catalyst.

5.3.3 Plasma damage of carbon nanotubes

We use an oxygen plasma to damage the partially-protected nanotubes. The plasma attack on the tube happens while the chip is still covered with aluminum oxide and photoresist, see figure 5.3f. The electrical contacts and parts of the nanotube near the contacts are protected by photoresist and aluminum oxide, whereas the middle of the nanotube is only partially protected by aluminum oxide.

The plasma used is an oxygen plasma generated by the Applied Materials 72 etcher in the CNF. The etcher creates charged oxygen radicals, and then accelerates them with a large electric field to drive them into the surface. The machine has a high aspect ratio for etching, implying largely vertical trajectories for the radicals. The delivered power at the surface of the wafer was varied from 0.02

to 0.3 W/cm^2. The oxygen pressure was 60 mT, and the gas flow rate was 25 SCCM. The angle of incidence of the plasma on the chip was varied by placing the chips in the plasma cleaner at different angles[3], with incidence from 90° to 75°. The duration of the plasma attack varied from two seconds to two minutes. All of this permuted with the deposition angle and deposition thickness of the aluminum oxide creates a very large phase space. However, a critical factor is the nanotubes themselves. Different tubes on the same chip (which have the same parameters except nanotube diameter) were affected by the plasma differently.

After the plasma attack, the surface coverings were removed. The oxide would be removed in an etch of Aluminum Etch A at 50°C. This viscous liquid etch is a mixture of phosphoric acid, nitric acid, and acetic acid [133][4]. Vigorous water rinsing is required to completely remove the aluminum etchant from the surface. After removing the oxide, the photoresist was removed with a standard bath in 1165. With the surface covering layers removed, we can investigate the damage to the nanotubes.

5.4 Probing the results

The effects of the oxygen plasma on the nanotubes were measured in different ways. The most conclusive evidence of damage is seeing a physical change along the length of the tube. We look directly at height changes along the tube's

[3]Different angles achieved by resting one end of the chip on a small piece of fused quartz to tip it in the plasma cleaner.

[4]The etch rates papers put out by the Institute of Electrical and Electronics Engineers were incredibly useful and occasionally inspiring. I recommend having a printed out copy to keep with any lithography fabrication notebook.

length in section 5.4.1. The fastest way to check for damage to the tube is to compare the conductance before and after the plasma, which we do in section 5.4.2. We use electric force microscopy to measure the resistance along the tube in section 5.4.3. The plasma changes the nanotube's sensitivity to a local gate, which we explore in section 5.4.4.

5.4.1 Height measurements

Height measurements along the tube give a clear indication of sections of tube being removed. We use an atomic force microscope to measure the height along the length of the tube. Figure 5.5 shows an AFM image of a sample that was plasma attacked. On top is the standard bird's eye view. The bottom image is a profile view of the nanotube. The height of the undamaged sections is 6.7 nm. The center section goes down to 2.5 nm high. The uniform height sections on the sides indicate where the photoresist and aluminum oxide protected the tube from damage. The center section of this carbon nanotube was damaged by an oxygen plasma. The 6.7 nm initial diameter of this tube means it is a multi-wall tube. The height-reduced sections are 10s of nanometers long or longer, implying large holes into the interior of this multi-wall nanotube.

5.4.2 Conductance

Figure 5.6 shows the conductance of the nanotube from figure 5.5 before and after plasma etching. The conductance of the tube is plotted versus gate voltage. The initial conductance (in blue) is around 30 μS with a ~5% change in

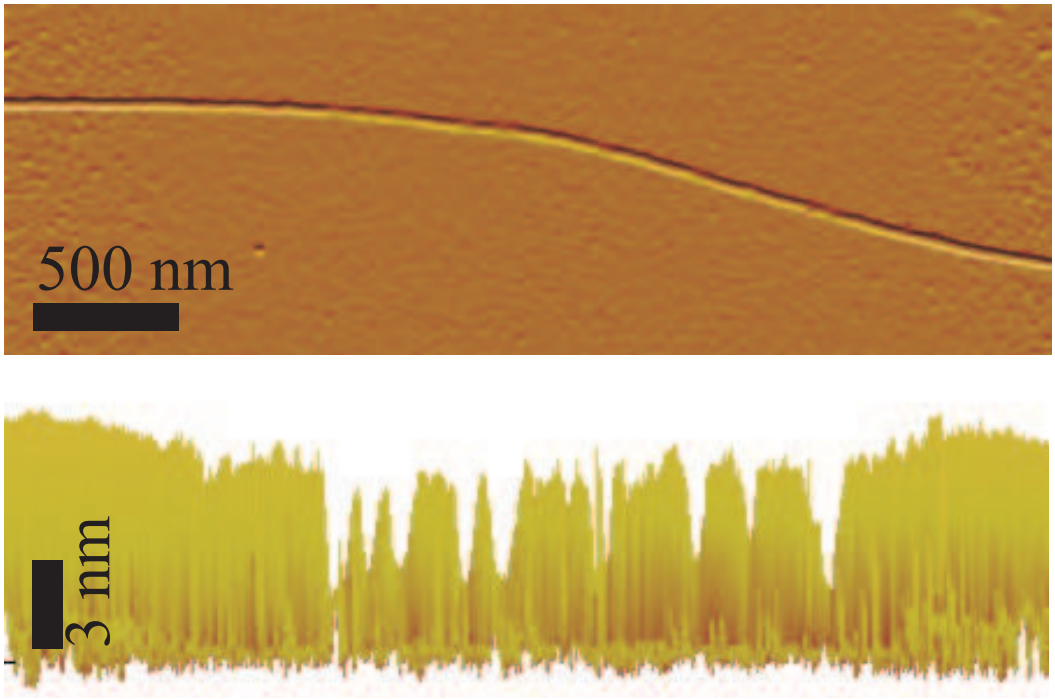

Figure 5.5: AFMmeasurements of a tube damaged by plasma. The top image is a standard bird's eye view of the nanotube. The bottom image shows the nanotube in profile. The height of the nanotube is noisily decreased in the middle of the tube where the oxygen attacked the tube. The fully protected ends of the tube show nearly uniform height.

conductance modulated by the gate. The conductance after plasma in shown in red. The conductance is only ~1μS. The gate can now change the conductance by ~50%. The plasma etch decreases the conductance by a factor of thirty, and increases the gate sensitivity (as a percentage). The structure of the conductance as a function of gate voltage also changes.

In general, measuring the conductance of the nanotube transistors before and after the plasma damage was the fastest way to see which tubes had been affected by the plasma. Permutations of deposition and etch parameters were varied from almost no effect on the tubes' conductance to complete destruc-

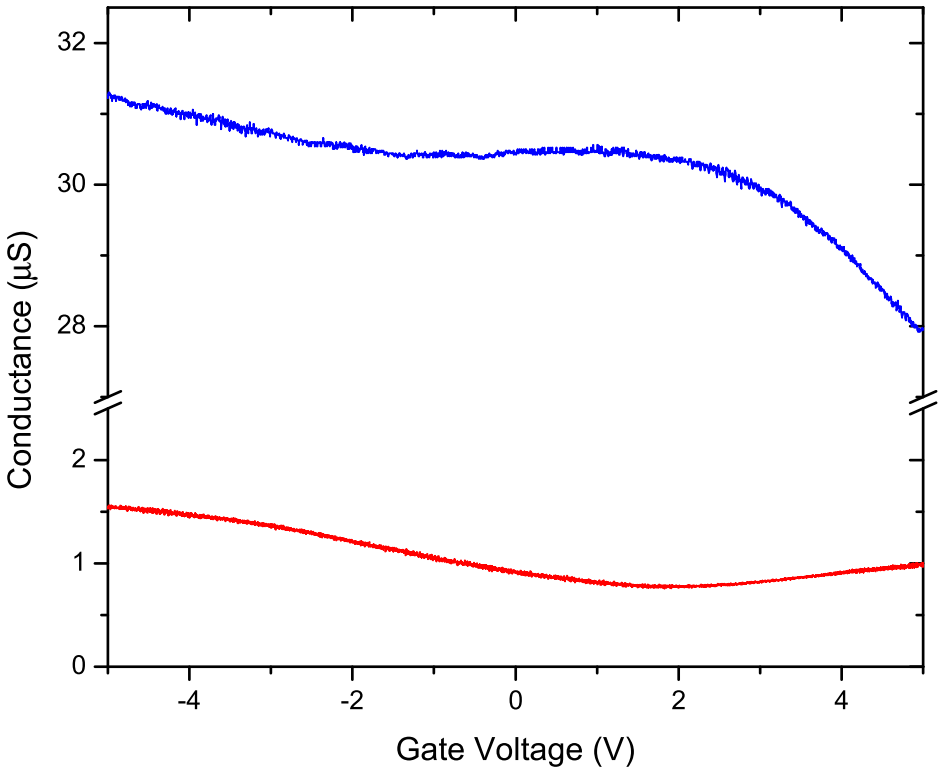

Figure 5.6: Conductance before (blue) and after (red) plasma damage to the nanotube. The initial conductance was ~30 μS. After plasma damage, the conductance was only ~1 μS. The percentage increase the gate voltage has on the conductance increased after plasma damage.

tion of all tubes on a chip. In general, high power and longer times resulted in larger decreases in conductance and more tubes being destroyed. However, differences between tubes created a large variation in the results of the oxygen etch. On a single chip with the same deposition and etch parameters, we saw different results for different nanotubes. One device might stop conducting altogether, whereas another would be only slightly affected, or one device might not be affected at all while another's conductance was significantly decreased.

5.4.3 Electric force microscopy measurements

We've shown that the cross-section of the nanotube was changed by the oxygen plasma. We've shown that the plasma changed the conductance of a nanotube. We now show the correlation between these changes. Electric Force Microscopy (EFM) is a way of measuring the potential as a function of position ([105], [4], [75], [119], [107]). We use that correlation to investigate the damage to the tube. We give a brief description of EFM, followed by EFM measurements from this device.

In EFM, a standard tapping mode image of a surface is compared to a scan with voltages applied to the sample on the surface. A conductive AFM tip is used to take both scans. The tapping mode image is taken first to create a reference which allows the tip to be held at a constant distance from the surface during the EFM scan.[5] The tip is re-scanned over the surface at a fixed height without the AFM applying an oscillation to the tip. During this scan a voltage is applied to the sample (for us, the nanotube), which covers only part of the surface. When the tip is over the sample, the voltage difference causes a force on the AFM tip [75],

$$f = \frac{1}{2}\Delta V^2 \frac{\partial C}{\partial z}, \tag{5.1}$$

where ΔV is the voltage difference between the tip and its environment and $\frac{\partial C}{\partial z}$ is the change in the tip-surface capacitance as a function of height. By making the voltage on the sample oscillate at the resonant frequency of the AFM cantilever, we efficiently induce an oscillation in the AFM tip [11]. The amplitude of that oscillation is read by the AFM, and correlated with the xy-position. This gives a

[5] In practice, the tapping mode and EFM scans are interleaved line by line, rather than whole image scan by whole image scan. This minimizes drift and provides information faster.

voltage map of the surface.[6]

By applying a DC voltage to the AFM tip, $V_{tip,DC}$, we increase the sensitivity of our scan for the same AC voltage on the nanotube, $V_{NT,AC}$. The difference in voltage between the tip and the tube is $\Delta V = V_{tip,DC} + V_{NT,AC}$, so the force goes as

$$f = \frac{1}{2}\frac{\partial C}{\partial z}(V_{tip,DC} + V_{NT,AC})^2 = \frac{1}{2}\frac{\partial C}{\partial z}\left(V_{tip,DC}^2 + 2V_{tip,DC}V_{NT,AC} + V_{NT,AC}^2\right). \quad (5.2)$$

The $V_{tip,DC}^2$ term gives an offset to the EFM scan. Since $\cos^2 \omega t = \frac{1}{2}(1+\cos 2\omega t)$, the $V_{NT,AC}^2$ term gives an offset and a driving force at twice the resonant frequency, which will average out. The interesting force is thus the $\frac{\partial C}{\partial z}V_{tip,DC}V_{NT,AC}$ term, which goes linearly with the AC voltage on the sample and the DC voltage on the tip. In our experiments, tip voltages were usually a few volts. Sample voltages in our experiment were order 100 mV. Applying a large DC voltage to the tip saves us from having to apply a large voltage to our sample.

We've talked about applying a uniform voltage to our sample, but we can get additional information by creating a voltage profile along our sample. $V_{NT,AC}$ is applied to one contact of the nanotube transistor, and the other end is grounded. Since EFM scans read the local voltage, we'll measure the voltage profile along the nanotube, which gives us information about the resistance along the tube [4]. Areas of high resistance in the tube cause voltage drops. Areas of low resistance do not have much effect on the voltage. Point resistances (e.g. at contacts) are steps in voltage, whereas uniform resistance per length values give steadily decreasing voltages.

Figure 5.7 shows EFM scans from the previously displayed device. The top

[6] All the EFM measurements and discussion in this thesis will be of AC-EFM, where the voltage on the sample oscillates at the resonant frequency of the AFM tip. It is possible to take DC-EFM scans without an oscillating voltage (see review in [105]), but we will not discuss that technique here.

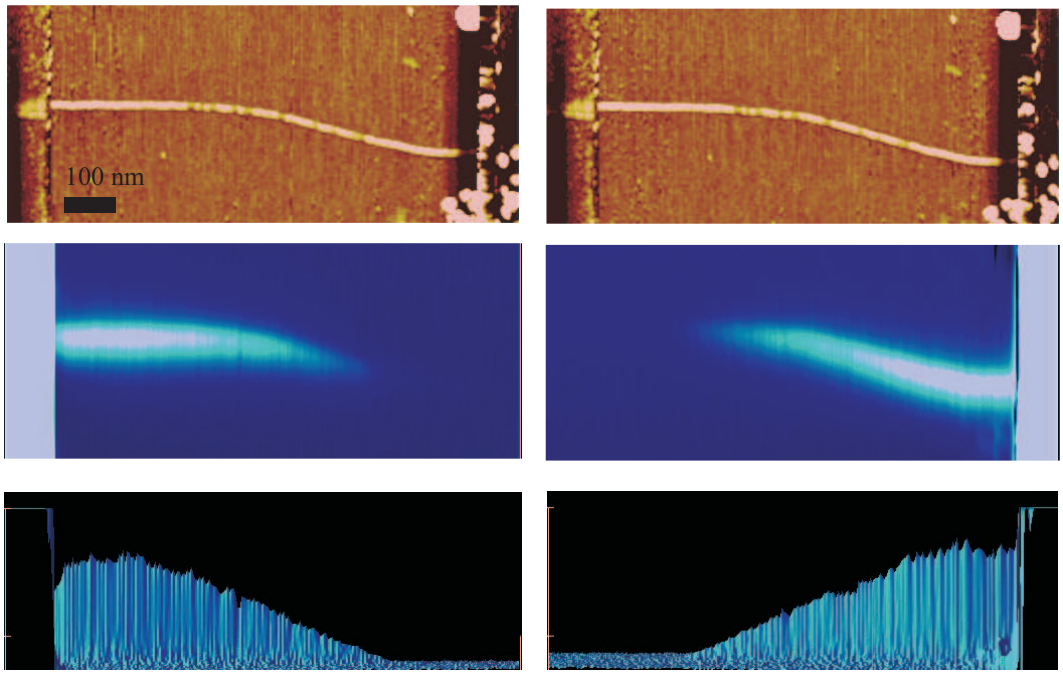

Figure 5.7: EFM scan of plasma damaged tube. In the left column: standard tapping mode, EFM with voltage on left contact and right contact grounded, profile of EFM scan. In right column: standard tapping mode, EFM with voltage on right contact and left contact grounded, profile of EFM scan.

pair of images are the regular height images from each scan. The damage in the middle of the tube is visible. The middle pair of images are EFM scans. The left image has an AC voltage of 100 mV on the left contact, and the right contact is grounded. The image on the right is another scan with the voltages reversed. The right contact is at 100 mV, and the left is grounded. The tip is scanned 5 nm above the surface at 2 μm/s lateral velocity, with a voltage of 2 V. The bottom pair of images are the middle pair viewed in profile.

In the middle image, we can see the voltage signal from the nanotube gradually decrease as it goes from the contact with a voltage to the grounded contact. The decrease mostly happens in the center region where the nanotube is dam-

aged. [7]

It is easier to see the structure of the nanotubes EFM scans looking at the amplitude in profile, as seen in the bottom pair of images. The amplitude of the EFM signal remains constant (flat horizontal line in profile) for the nanotube in the region next to the contact. This flat area means there is a constant voltage, which means that the resistance in this section of the nanotube is very small compared to the overall resistance. In the center section of the nanotube, we see the EFM signal decrease along the length of the tube. The voltage is dropping in this area, which means the plasma-damaged area corresponds to the region of large resistance. The EFM signal goes to zero for both the undamaged section of tube connected to the grounded contact and the grounded contact. There is more analysis that we can do on the EFM images, but we'll first discuss our other investigative techniques, and then make a composite from all the information.

5.4.4 Scan gate microscopy measurements

We can use scan gate measurements (SGM) to investigate the damaged tube. In scan gate measurements, a conductive AFM tip is used as a local gate. A voltage is applied across the nanotube to generate a current. The AFM tip is scanned over the device with a voltage on the tip. The tip voltage locally gates the nan-

[7] The voltages involved in getting a clean signal from the nanotube create difficulties imaging near the contact, which has a different $\frac{\partial C}{\partial z}$ term. The contact with an applied voltage gives an excessively strong EFM signal that has been flattened out. There is a step down in signal crossing from the contact with applied voltage to the nanotube. This voltage drop is caused by the contact-resistance to the nanotube. We know the grounded contact has a contact resistance to the nanotube, because there is a step when the applied voltage/ground are reversed. The V=0 of the grounded contact in equation 5.2 makes the induced force from the grounded contact zero.

otube and changes the current passing through the tube. By correlating the current through the tube with the tip's position, a map is made of the device's sensitivity to local voltage. The technique highlight differences and changes in the electrical properties along the nanotube, such as defects or chirality shifts [95]. In our experiment we anticipate the defects from the plasma damage will change the electrical characteristics of the tubes as a function of position.

Figure 5.8 shows a scan gate image of the same tube we've been discussing. The standard AFM image is on top, and the SGM image on the bottom. The intensity of the SGM image reflects the change in current as a function of tip position. The brighter areas occur where the current changed the most. The scan was taken at a back-gate voltage of -5 V, creating a p-type nanotube. There was a 100 mV bias between the contacts driving a current of 160 nA. The tip was at +10V, and was scanned 5 nm above the surface. The positive voltage on the tip decreased the current through the nanotube. The maximum change (brightest area in image) was a decrease of 10 nA, or -6%. The largest change in current occurs when the tip is gating the damaged section of the tube. The plasma damage has increased the tubes sensitivity to local electric gating.

Although the scan gate measurement shows the tube has heightened local gate sensitivity in the damaged region, there should be some care in the interpretation of the results. It is possible that the chemical processing steps such as the acid etch might influence the wafer and create or destroy charge traps on the surface in the region correlated with the plasma damage (only that part of the surface saw that acid etch to remove the aluminum oxide). We thus do not consider scan gate measurements on their own to be a good indication of successfully locally damaging the carbon nanotube. The chemical steps taken

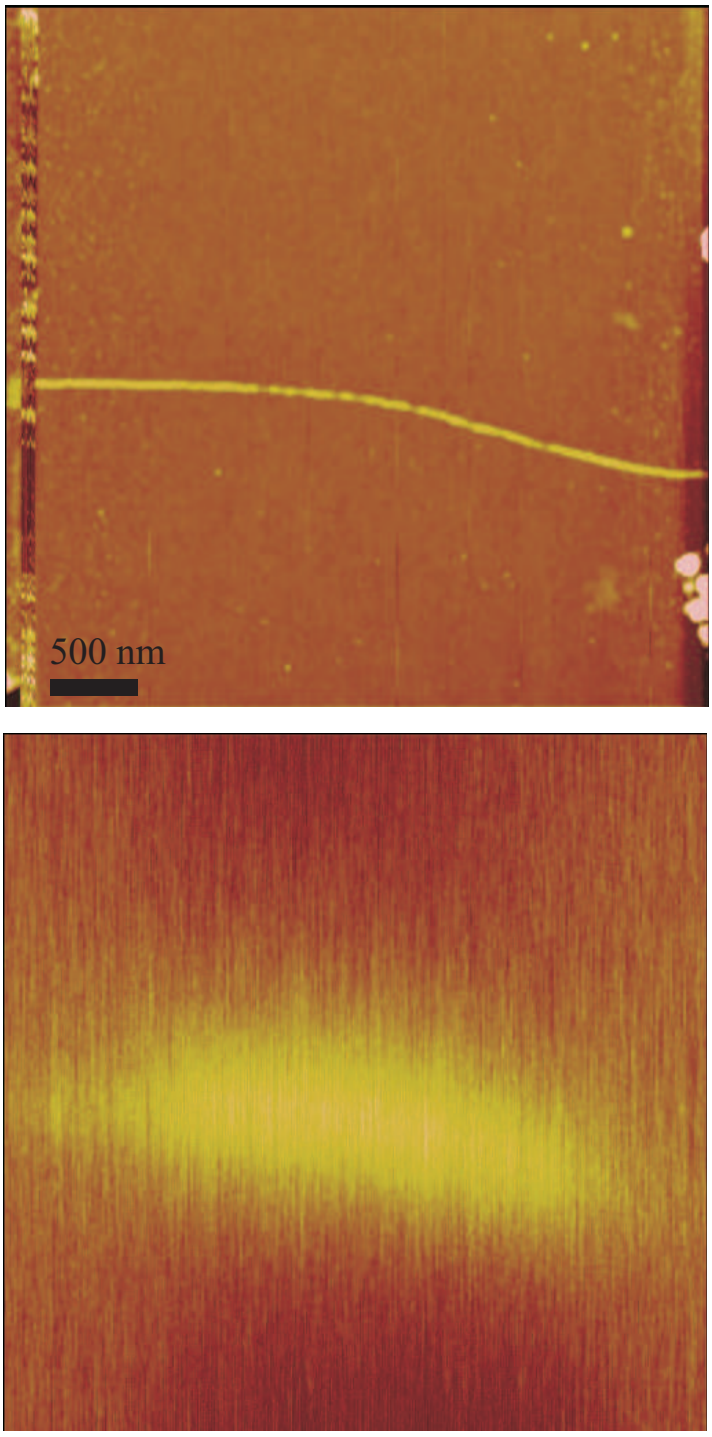

Figure 5.8: Scan gate image of plasma damaged carbon nanotube. The bright areas indicate sensitivity to a local gate voltage. The positive voltage on the tip caused a maximum decrease of 6% of the current through the p-doped tube. The largest shifts correlate with the damaged region in the center of the tube.

have irrefutably changed the local gate sensitivity, independent of actually creating damage. For the device shown here, we also see effects in height and EFM scans that all correlate with the region of oxygen plasma. This lets us say with confidence that the plasma has etched away part of the nanotube in that area. We now investigate what happens to that etched tube when it is heated.

5.5 Annealing the damage

Intact carbon nanotubes are relatively inert. They are energetically favorable enough to form at temperatures over 900°C (without oxygen). Research into purification shows that some nanotubes will burn in atmospheric gases at 350°C [110]. Studies of graphite indicate that edge states are more susceptible to oxidation [52]. We thus expect that damaged nanotubes, with openings in the tube's lattice, would be less stable to heating in an oxygen atmosphere than regular nanotubes. We can thus further investigate the damage to the carbon nanotube by heating it in atmosphere.

This chapter's workhorse device was heated in atmosphere to see how it changed, using the same furnace we grew the the carbon nanotubes in (figure 3.3), with the ends of the furnace tube open to atmosphere. The device was heated to 200°C for various lengths of time, with cool-downs to allow imaging in the AFM and conductance measurements.[8]

Figure 5.9 shows how the nanotube changed after being heated. Each scan

[8]The devices used in the experiment were fabricated with gold and palladium on top of silicon dioxide, with a doped silicon back gate. Elevated temperatures can cause the gold to ball up, move around, and/or diffuse through the silicon dioxide, shorting out the back gate. This puts an upper limit on the annealing temperature.

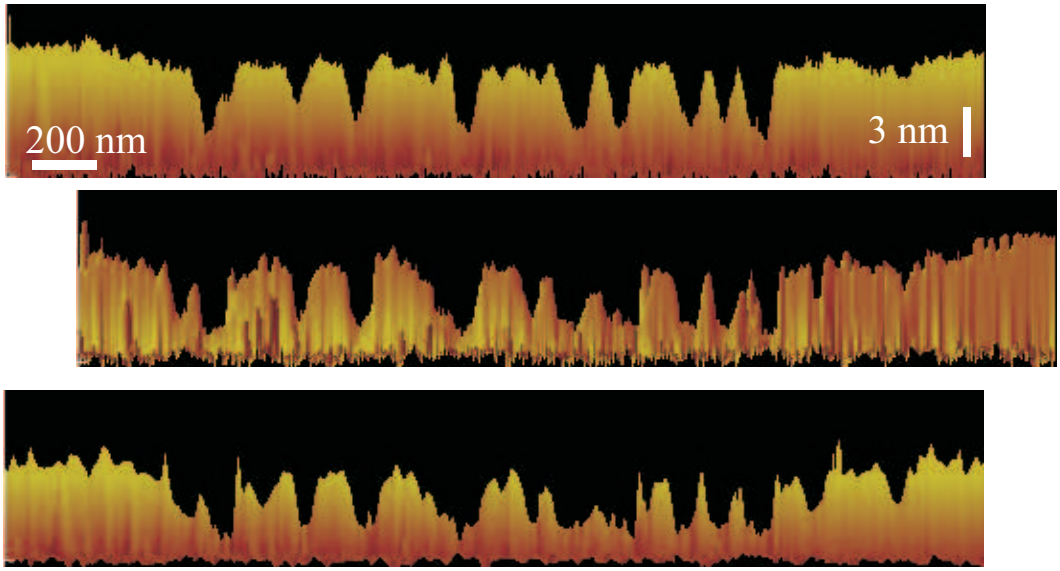

Figure 5.9: Top image: profile of nanotube before any heating. Middle image: profile of nanotube after 10 minutes at 200°C. Bottom image: profile of nanotube after 9 hours at 200°C. Pictures are aligned by inspection of features.

image is a profile view of a 3 μm scan of the nanotube. The scale bars are 200 nm for length and 3 nm for height. The three images are aligned by matching features.

The top image comes from before any heating of the tube took place. The ends of the tube are 6.7 nm high, and the low spots in the middle of the tube are at 2.5 nm. The second image is after 10 minutes at 200°C in atmosphere. The center of the tube show a significant increase in damage. The lowest points are now down to 2 nm. The low sections are also now wider. The high sections inside the damaged region are narrower and lower. Near the ends, the effect is not nearly as dramatic. There is not much change to sections that weren't already damaged. The bottom image is after a total of 9 hours in the furnace at 200°C. While there is an increase in the damage from the previous image, the

vast majority of the change happened in the first few minutes of heating.

The conductance of the nanotube increased as a result of the heating in the furnace, shown in figure 5.10. After heating, the conductance of the sample increased by about a factor of 2, from 1 μS to 2 μS. The gate dependence was simplified, showing monotonic decrease with higher gate voltages after heating, compared to a minimum conductance at 2 V prior to heating. The majority of the change came after the initial heating. Repeated heating in the furnace caused a slight increase in the highest conductance. It is interesting to note that heating caused the average cross-section of the nanotube decreased, but the maximum conductance increased.

In addition to heating in a furnace, it would also be possible to heat the sample with resistive heating by passing a large current through the nanotube. This has the advantage of directly heating the sample at the places where the resistance is highest. It also becomes possible to AFM the tube while heating without requiring an AFM inside a furnace. A drawback to Joule heating is that large currents have to be driven through the sample to deliver heat to the system, and these large currents can completely burn up the nanotube. The tube also has to be thermally well-isolated to reach high enough temperatures. Time and system constraints have terminally delayed this line of inquiry, but it remains a promising avenue for future investigation.

Annealing the damaged nanotube spread the damage. The plasma attacked section shows dramatic loss of material. The initial 6.7 nm tube was a multi-wall nanotube that suffered a massive decrease in conductance after the plasma. The fact that continuing to remove material is not detrimental to the conductance leads us to believe the material burning off in the furnace are pieces of the outer

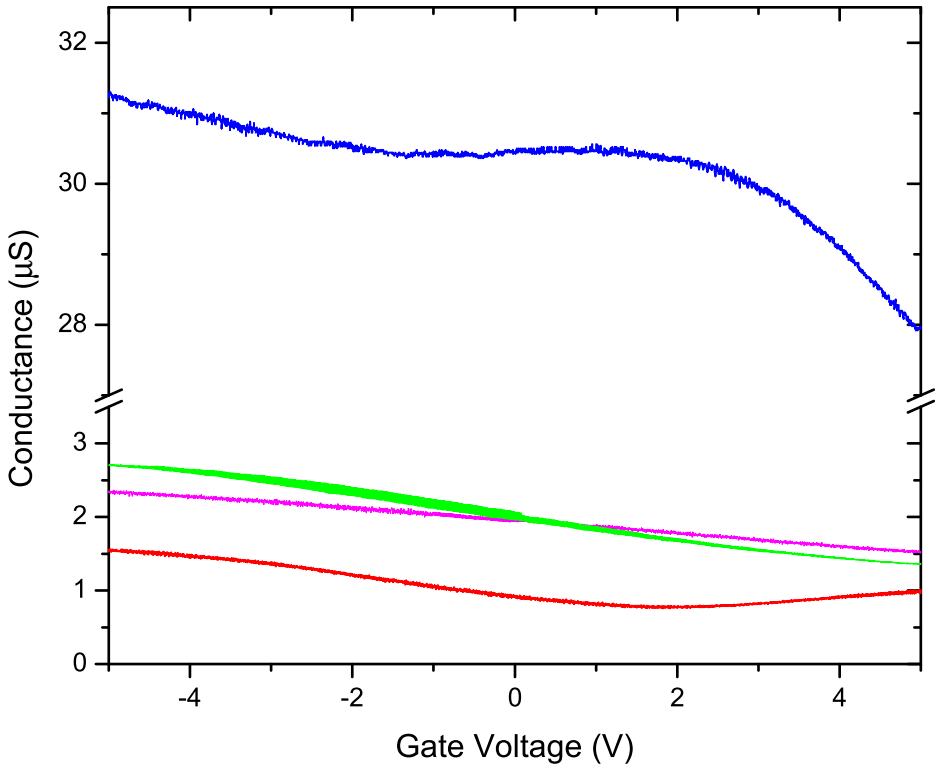

Figure 5.10: Conductance before (blue) and after (red) plasma damage to the nanotube. Conductance after first heating (magenta) at 200 °C for 10 minutes. Conductance after more heating (green) at 200°C for a total of 9 hours.

shells of the nanotube that are no longer connected across the tube, and thus no longer contribute to the conductance. There seems to be a stable core shell inside the multiwall tube. The slight decrease in minimum height from 2.5 nm to 2 nm could be from pieces of carbon under the inner shell burning off and allowing the tube to rest on the surface, or from restructuring of the tube as it switches around bonds to remove defects. Restructuring of the tube may be what caused the conductance increase after annealing. It may also be from p-type doping of the surface, or changing the contact resistance ([23], [73]). Different annealing

recipes for future samples, local heating, different gases, different temperatures, etc. may help track down what exactly is responsible for the conductance increase. Whatever the cause of the increase, the tube conducts better and has less material after being annealed.

5.6 Analysis of the damaged tube

We've now seen all the evidence for localized damage. This section will put it together to construct a more complete microscopic picture of what happened to the specific nanotube shown. We'll step through how we use the above information to infer that the inner conducting shell was severely damaged along it's length, not just in isolated spots.

After the plasma, the 6.7 nm shell does not exist in all parts of the damaged section, so it can not carry current all the way across the tube. If the electrical contacts are just to the outer shell the current must transitions from the outer shell to the remaining inner 2.5 nm shell of the nanotube to pass through the damaged region. If the electrical contacts couple to the remaining inner shell, the current could being carried by the inner shell of the nanotube across all 4 μm of the device. The EFM images tell us there is a contact resistance between the metal and the nanotube. However, we know from the existence of structure in the nanotube's voltage profile (figure 5.7) that the contact resistance of the metal to the tube is not the dominant resistance of the system. If it were, all the voltage drop would be across the two contacts. We use this information to rule out the drastic increase in resistance after plasma damage coming from increased contact resistance to a different conducting shell of the multi-wall nanotube.

The horizontal profile in the undamaged region in the EFM scan then tells us that either the metal is making good electrical contact to the inner shell directly, or it is making good electrical contact to the outer shell which is making good electrical contact to the inner shell.

The initial conductance of the multi-wall carbon nanotube was 30 uS. Both the initial and final conductance have weak gate voltage dependence, indicating a small bandgap tubes where the incoherent transmission model of conduction may prove a fruitful analysis tool. If we assume that initially the current was carried through only the outer shell of the tube [19], the mean free path for charge carriers in this 4 μm tube is, from equation 2.47, about 0.8 μm.

After the oxygen plasma, sections of the tube are reduced to 2.5 nm in height. When we annealed the tube, these sections reduced to 2 nm but no further. We thus expect the 2.5 nm height was initially an inner shell of the larger multi-wall nanotube with pieces of the outer shell. The anneal removed the outer shell pieces, leaving an inner core. The stable inner core after annealing indicates that there was an inner shell nanotube to conduct after the plasma damage. We don't expect the pieces of outer shell inside the damaged region to contribute to the conductance after the plasma damage.

We use this information to look at the conductance after the plasma damage, but before the anneal. We've argued that there is a conducting inner shell. If the increase in the resistance comes only from increased scattering in the 2 μm damaged section, and only one shell conducts, we arrive at a mean free path for charge carriers of roughly 0.01 μm. This is significantly shorter than sections of the nanotube in the damaged region that still have a height of 6.7 nm (before anneal, see figure 5.5). Either the scattering length along the entire

damaged section has been significantly reduced, or there are regions in the damaged section where the scattering length is much less than 10 nm to make up for other regions in the damaged section with mostly unaffected mean free paths. We see from the scan gate image 5.8 that there are not highly localized defects, but instead an overall increase in local gate voltage sensitivity throughout the damaged area. We conclude that the increase resistance is not a result of a few intense defects in the inner core, but of damage to the inner core throughout the length of the damaged section. That means that even though there are regions inside the damaged section where the height is still 6.7 nm in figure 5.5, there is damage to even the inner core in these regions. This collaborates well with the EFM images showing a linear voltage drop in the damaged section.

5.7 Conclusion and future directions

We've made significant progress towards the goal we set out for in the introduction. We have shown that it is possible to use oxygen plasma to partially damage a carbon nanotube in a confined area. This damage opens large holes into the interior of the tube. The damage is interesting because it did not completely destroy the nanotube. The damage is visible in height measurements. The damaged tube was able to pass a current, although the conductance was decreased. The damage correlated with increased sensitivity to local gating. Electric force microscopy showed a linear decrease in potential in the damaged region, implying high resistance per unit length in that area. Heating after the plasma damage was seen to continue to remove material but increase the conductance of the damaged tube.

We've shown how the battery of investigative techniques allow us to form a detailed picture of the damage to the carbon nanotube. These tools will hopefully be useful in continuing this work towards the applications described in the motivation section 5.2.

A logical next step for this research would be to continue on larger multi-wall tubes. Similar work has been preformed on multi-wall carbon nanotubes without a partially shielded layer, with the intent of creating rotational bearings [140]. For electrical work, larger tubes make it easier to controlled local damage and are less sensitive to minor variations. A bonus to larger multi-shell systems would be studying tube-to-tube transport, especially if an additional electrical contact was made in the central damaged region after plasmaing and AFMing that area. The presence of many tubes may complicate the electrical characterization, which is part of why we initially focused on smaller tubes, but it may also offer new insights into tube-to-tube transport. Systems where inter-tube transport can be studied offer interesting comparison cases to inter-layer transport in graphite, a system that is becoming much more promising [31]. We believe that this work is different than similar work burning the outer shells off of multi-wall nanotubes with electrical current [19] because here we can damage a nanotube shell without it undergoing catastrophic failure.

We believe the initial results and possibility for advancement with this research warrant further investigation. This research lays the groundwork and can determine fabrication parameters for the applications described in the motivation section.

CHAPTER 6

CARBON NANOTUBES AS SCAFFOLDING FOR GOLD

6.1 Introduction

This chapter describes several experiments that study the interplay between gold and carbon nanotubes.

Graphitic carbon provides a clean and regular surface for interacting with gold, and researchers have been studying gold on graphite for decades [20], [130]. After carbon nanotubes were discovered [45], people quickly became interested in putting gold and other metals on nanotubes. Gold nanoparticles on carbon nanotubes have promise as gas sensors([118], [138],) and single-electron transistors ([122], [33]). Previous work shows gold can move along suspended nanotubes ([143], [98], [13], [106], [5]). This has been used to make nanospot-welders [27] and nanomotors [97]. Small gold balls can be used to grow semiconducting [65] or gold [77] nanowires. When the gold is on the nanotube the grown wire can creation a nanowire/nanotube junction. The nanowire could be used as an antenna to couple electromagnetic radiation into the nanotube [3], studies of the junctions of 1D systems, or a new twist on photothermal imaging ([144], [10], [123]).

The first set of experiments in this chapter explore just some of the possibilities of nanometer-sized gold balls on carbon nanotubes. In section 6.2 we use an atomic force microscope to create the gold-on-tube system. We show the growth of a nanowire off the deposited gold in section 6.3. We then look at melting the deposited gold in section 6.4. Melting small gold deposits and

looking at how they interact with carbon nanotubes leads us to looking at what happens when larger gold wires melt near carbon nanotubes (section 6.5). We shift over to macroscopic (μm sized) gold wires for the remaining experiments in this chapter.

Melting gold wires have been used in electromigration[1] experiments to create nanometer sized gaps ([88], [89], [68], [139], [114], [43], [40], [81], ([121]). These gaps are then bridged by molecules, and the current carrying characteristics of the wire-molecule-wire system gives information about the molecule. Although many research groups use these electromigrated gaps, the creation and characteristics of them are still very difficult to make reproducibly. We will show in section 6.6 that a carbon nanotube can influence the location of these gaps. The creation of a gap in a wire around the nanotube means that the tube could serve as an additional electrode in studies of molecules in that gap. The nanotube itself could also be the study subject. The broken wire could also be used to generate large electric fields transverse to the nanotube, a subject that has received much theoretical discussion ([146], [86], [67]) because it may allow the manipulation of the bandstructure of the nanotube.

6.2 Localized gold deposition with an atomic force microscope

We use an Atomic Force Microscope (AFM) to deposit gold onto a nanotube. Figure 6.1 shows a schematic representation of deposition. We have our standard nanotube transistor and an AFM tip with a metallic coating. We bring the

[1]Electromigration is where atoms in a system move because of a current. The movement can be large enough to create a break in the current-carrying path. A fuse is a simple example of an electromigrated break. For a review of electromigration see [42], [92]

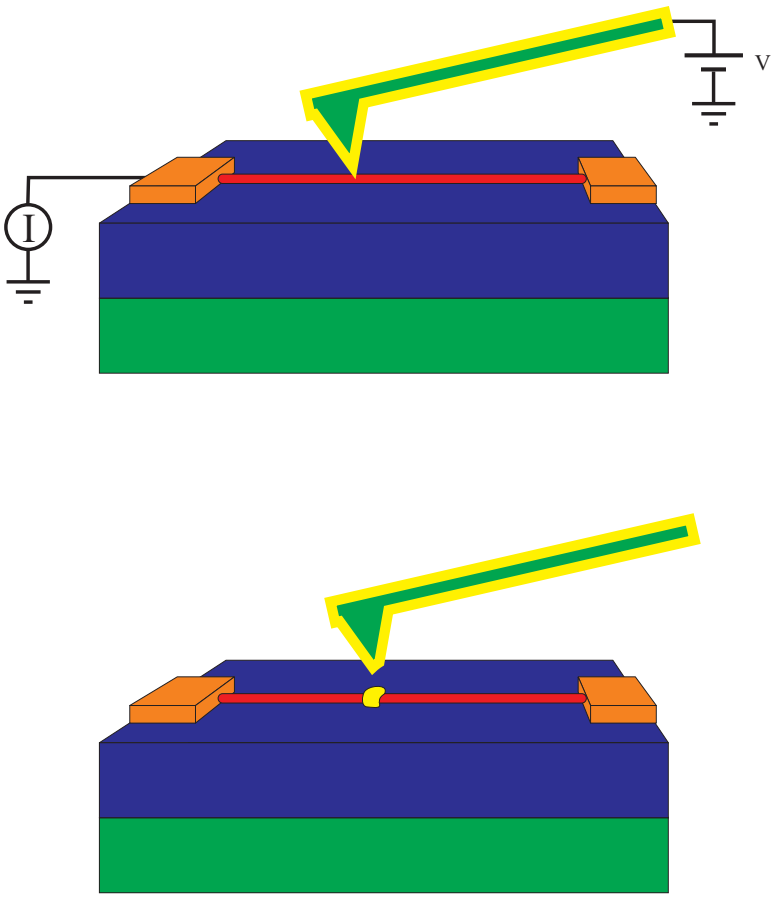

Figure 6.1: Schematic of using AFM to deposit gold on nanotube. We begin with the nanotube transistor described in chapter 3. Using a gold coated AFM tip (gold on green), we electromigrate gold onto a nanotube (red) by passing current from the tip to the nanotube and its electrical contacts (orange). The nanotube is on top of silicon dioxide (blue) on top of a doped silicon back gate.

AFM tip into electrical contact with the nanotube and apply a voltage difference between the tip and tube. Metal moves from the tip to the nanotube, depositing a blob of metal. Ideally, the conductance of the tube is unaffected by the deposition, leaving the nanotube transistor intact. The ability of an AFM to be positioned with nanometer accuracy gives us the power to locally define where on the nanotube we want the deposited gold. This deposition technique is simi-

lar to previous work cutting nanotubes with pulsed currents from an AFM [91]. It is also akin to nanopen lithography ([49], [93], [17]).

Figure 6.2 shows before and after pictures of gold deposition onto two different nanotubes. In the top pair of images, the tube is 6 nm in diameter, and the deposited gold blob is 22 nm high. The gold was deposited with a voltage of +5 V on the tip held for 30 seconds. The nanotube was at -5 V, and the back gate was at +4 V. The conductance of the tube was unaffected by the deposition. The tip changes shape as a result of the deposition, which can change how the nanotube appears afterward.

In the bottom pair of images, the tube is 1.6 nm in diameter, and the deposited gold blob is 13 nm high. The gold was deposited with a voltage of +5 V on the tip held for 60 seconds. The nanotube was at -5 V, and the back gate was at -4 V. After deposition, the tube no longer conducted, even though there is no visible evidence of a break in the tube. We successfully deposited metal onto many tubes without changing the conductance, and many more with small changes in conductance, but some of the tubes stop conducting after deposition.

This deposition technique is easily applied multiple times to create several depositions onto the same nanotube with controlled spacing between balls. Figure 6.3 shows several blobs deposited onto a 2.3 nm nanotube. In the top image, the 11 nm ball was deposited with +5 V on the tube and -5 V on the tip. The voltage difference was held for 6 seconds. The back gate was at -4 V and the tube's conductance of 1 μS was unchanged. In the second image, the 11 nm second ball on the right was deposited with the same parameters and also did not affect the conductance. The third image is a different section of tube, where we made a 11 nm high and 26 nm high deposit with the same parameters. Four balls of gold

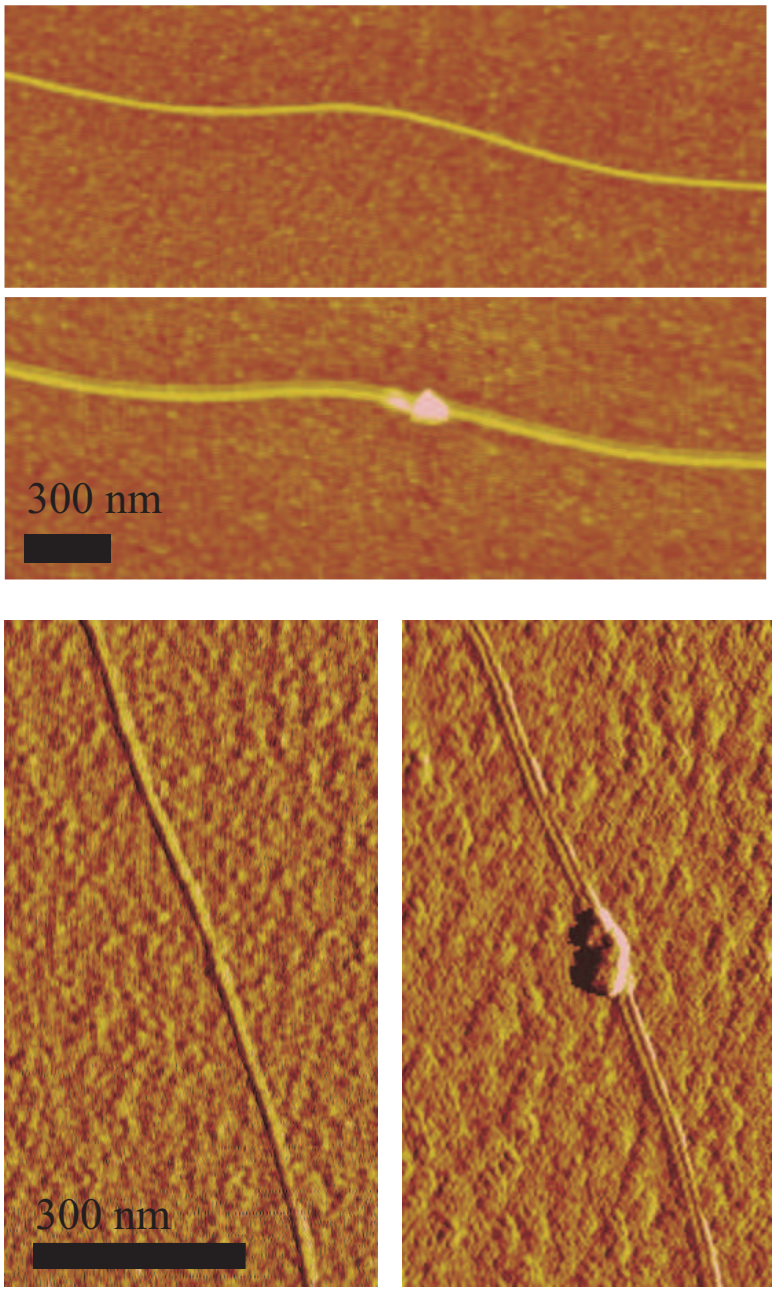

Figure 6.2: Two different examples of gold deposited onto a nanotube with an AFM tip. The deposition changes the morphology of the tip, and thus affects the image. Scale bars are 300 nm.

were successfully deposited onto this tube with the same parameters. Three of those deposits were of similiar size, and the fourth was significantly larger. While going for a fifth deposition at the same parameters, the tip not deposit and the tube's conductance went to zero. We've demonstrated this technique can be used for localized deposition with controlled spacing, but is not yet fully controlled.

The ability to deposit gold where we want to allows us to deposit gold at nanotube junctions. Figure 6.4 is an example of this. We selected a device with several tubes between the contacts. Two of the tubes crossed. An 8 nm high gold deposit was put on the junction of two tubes. The deposition had no effect on the overall conductance.[2]

Since performing these experiments, we learned of another group's recent work using AFM nanopen lithography to deposit gold onto carbon nanotubes [17]. The techniques are very similar, with different sets of limitations. Their paper did look at the conductance of the nanotubes after deposition, as they had only one electrical contact per tube. The size of their gold deposits are smaller, and they have some limitations requiring very thin back gate oxides ($\sim$ 10 nm). The two techniques may prove complementary for different systems. Anyone thinking of using an AFM for gold deposition on nanotubes is highly encouraged to read their paper. If the methods and results described here are a better match to requirements or available equipment, a next generation improvement

[2]Another straightforward use of nanowelding is depositing gold onto a cut in a nanotube. We succeeded in doing so, but the results were less than we hoped for. We cut a tube [91] and reduced it's conductance to zero. We then buried both sides of the cut in a gold ball and there was still no conductance through the tube. We infer from this that the deposited gold does not always make good electrical contact with the nanotube. Several efforts were made to improve electrical contact between the the tube and the deposited metal. Annealing cuts tubes with gold over the cuts in a furnace at 200°C did not restore conductivity. We attempted metal deposition with palladium-coated AFM tips, because palladium is known to make good electrical contact with nanotubes, but were not successful in depositing palladium from the AFM tip.

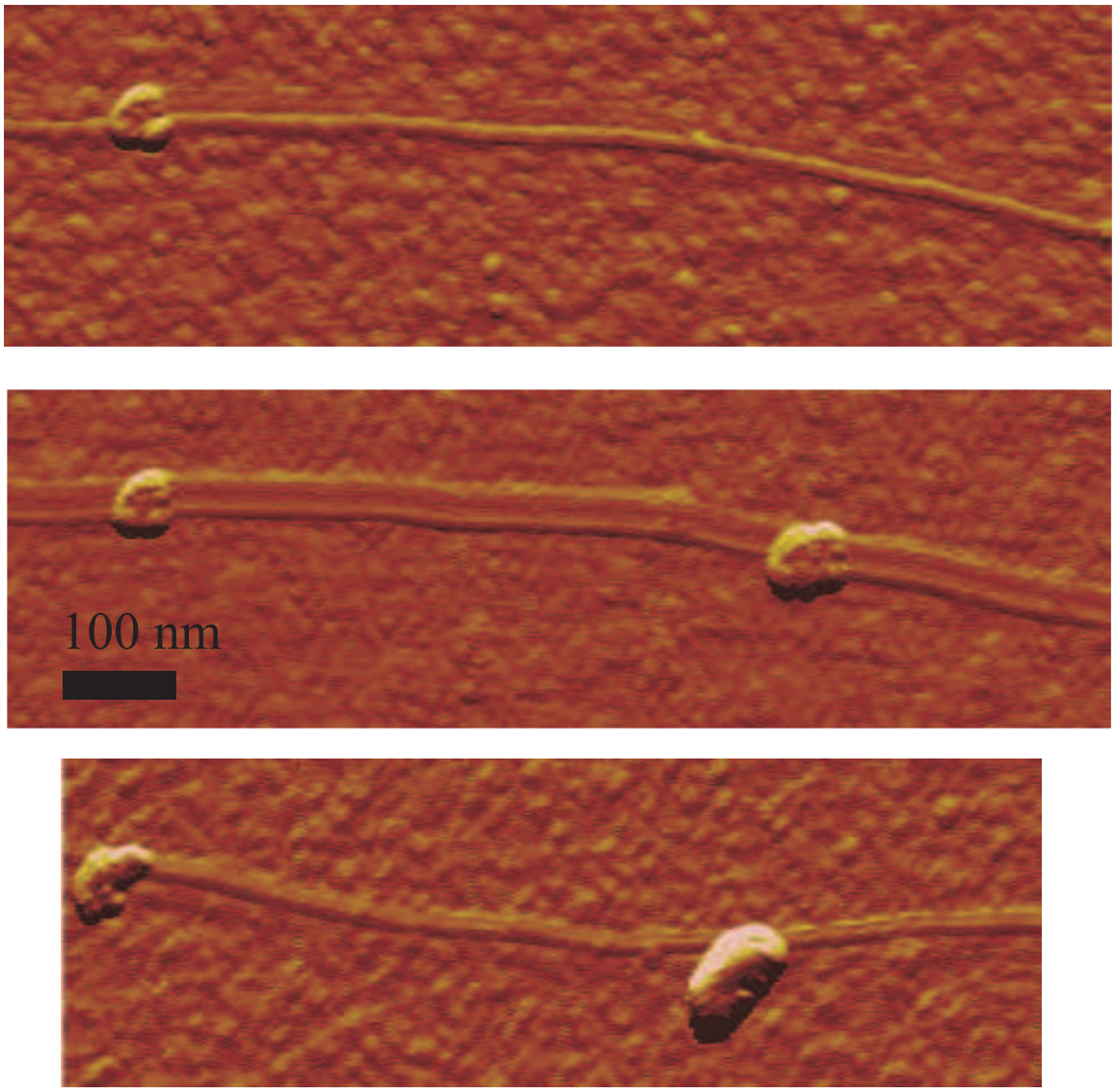

Figure 6.3: Before and after image of gold deposited onto a nanotube. The top image shows a nanotube after a deposit (11 nm high). The second image shows a new deposit (also 11 nm high) deposited on the same tube. The tip changed slightly after deposition. In the third image (shifted along the length of the tube) we show two more deposits on this tube (11 nm and 26 nm high) made with the same parameters. Scale bar is 100 nm. Tube is 2.3 nm in diameter.

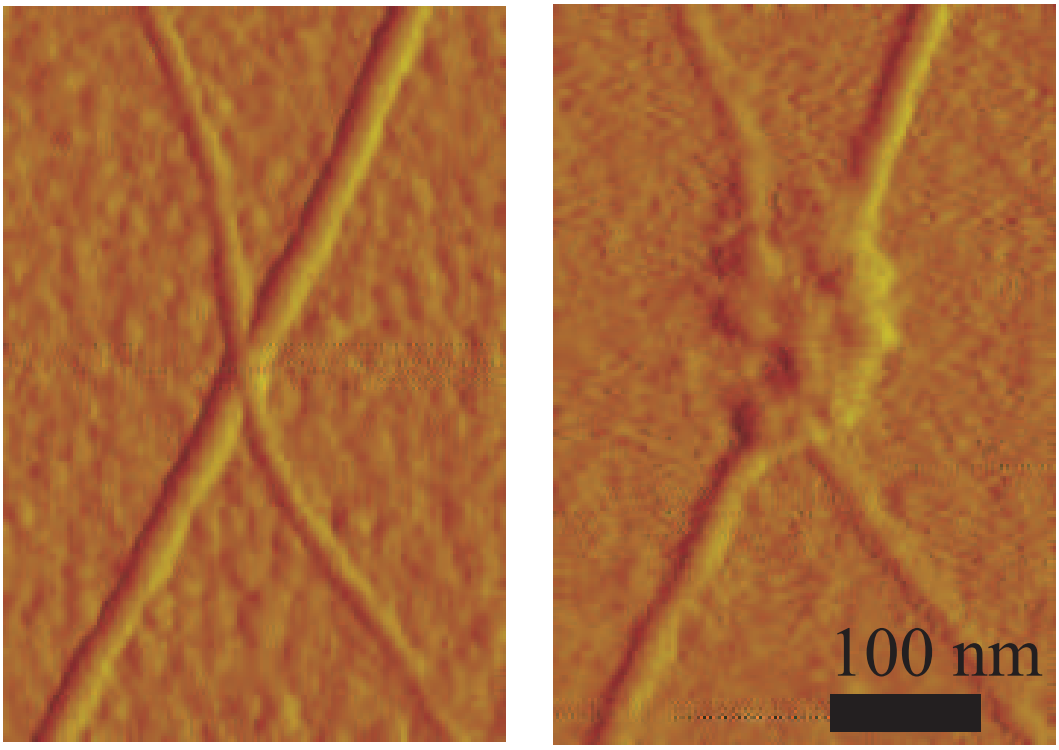

Figure 6.4: Before and after images of gold deposited on two crossed nanotubes. The tube running NE-SW is 3.2 nm in diameter, the tube running NW-SE is 1.3 nm. The bump is 8 nm high. The scale bar is 100 nm.

for this technique would be a current meter to monitor the resistance of the tip-tube interface during deposition.

We've demonstrated that with an AFM we can deposit gold onto nanotubes at controlled locations. We can do this with carbon nanotube transistors and not affect the conduction of the transistor. This is a positive result for using this or similar techniques to create the gold-bedecked nanotubes for the applications discussed in the introduction.

6.3 Nanowires on nanotubes

This section shows the growth of nanowires from the gold on our carbon nanotubes. Nanowires of germanium and of silicon can be grown from small metal catalyst particles [65]. We use the deposited gold as the catalyst particles for the growth of germanium nanowires.[3] Figure 6.5 shows an AFM image of a carbon nanotube with deposited gold before nanowire growth, and a Scanning Electron Microscope (SEM) image of a germanium nanowire grown off the deposited gold. In the AFM image on the left, one of the electrical contacts is visible at the bottom of the figure, and the nanotube runs vertically. The largest gold blob in the AFM image is 160 nm high. There are smaller amounts of gold from other deposits on the nanotube on the other side of the large bump from the visible contact. In the SEM image on the right, the contact is visible at the bottom. A nanowire is visible at the location of the deposited gold.

This demonstrates it is possible to grow nanowires from gold deposited on nanotubes. The nanowire growth deposited amorphous germanium on the surface of the wafer. Large amounts of growth also nucleated from the gold in the contact pads. Future efforts can use devices with contacts inert to nanowire growth (palladium, platinum, etc.) and fine tuning growth parameters for less amorphous surface deposition. We've demonstrated this technique has promise for the creation of nanowire junctions with carbon nanotubes.

[3]Growth consisted of flowing germane gas (GeH_4 1.46% in H2) at 25 SCCM and H_2 at 25 SCCM in a 360°C furnace for 15 minutes at 100 Torr. This was followed by a H_2 anneal of 20 SCCM H_2 at 30 Torr and 360°C for 10 minutes.

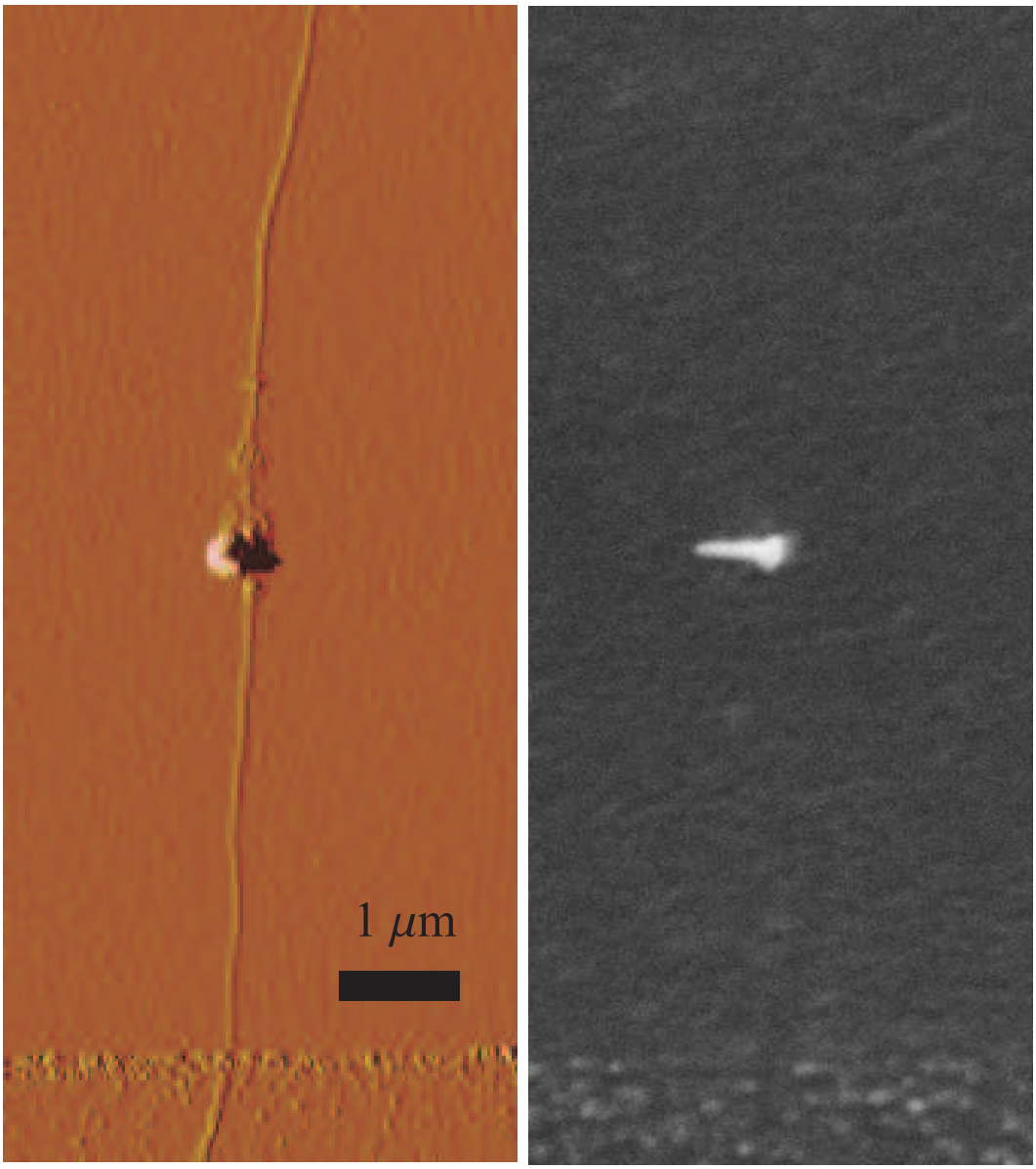

Figure 6.5: Nanowire grown off gold deposited on carbon nanotube. Image on left is an AFM image of the nanotube after deposition of gold but before growth. One electrical contact is visible, as is a large gold blob and several smaller deposits. On the right is an SEM image of the same spot after nanowire growth. The contact is still visible, as is the Ge nanowire that grew from the gold ball. Amorphous germanium on the surface prevents imaging of the nanotube after nanowire growth.

6.4 Melting of gold deposits on nanotubes

Carbon nanotubes can be used as conveyer belts for metal atoms. Previous work has used Transmission Electron Microscopes (TEMs) to image metal moving on suspended nanotubes in vacuum ([143], [98], [5]). Metal was evaporated onto suspended CNTs, which were electrically contacted with a micromanipulator and the TEM grid. A current was passed through the nanotube. The metal heated up and moved across the surface of the tube.

We performed similar experiments with the AFM deposited gold on CNTs. The primary differences are that we have CNTs on a surface instead of being suspended, we use an AFM to image instead of a TEM, and our tubes are not in vacuum. These extensions of the work thus make the nanotube mass conveyor belts something that can be used in solid state devices and ambient conditions. Possible applications include surface mounted nanomotors [97] or attogram-scale mass adjustments. The AFM deposition of the gold being melted instead of evaporation gives us greater control over the starting configuration of the gold being moved.

Figure 6.6 shows a gold ball on a nanotube melting and shrinking. The bias across the 2.4 nm tube was 8 V, which drove 43 μA of current. The power dissipated in the tube is thus $\sim$ 300 μW. The deposited gold can be seen to change shape as it melts, going from an asymmetrical blob to more of a uniform disk 90 nm across. With further heating the ball shrinks in size; the initial height is 30 nm and the final height is 24 nm. The final width is 60 nm. Small gold balls can be seen that either nucleated and grew off the main ball, or were left behind as the ball shrank. We believe the ball is shrinking because gold is moving from the

ball out along the tube. The volume of gold in the deposit changes from roughly 190,000 nm^3 initially to 68,000 nm^3 in the final image.[4] The total change of mass of the central ball is $\sim$ 2 fg. We've thus demonstrated the ability to change the mass of a gold particle continuously from 4 fg to 2 fg. While we do not see the gold atoms on the nanotube, results from the next section indicate molten gold prefers to move on nanotubes more than silicon oxide.

Gold melts at 1060°C[69].[5] The gold ball in figure 6.6 was melted with roughly 300 μW of power. The nanotube transistor is sitting on silicon dioxide that has a thickness of 200 nm. The back gate of the transistor is the thermal ground for the system. The nanotube and gold ball shed heat to the back gate through the oxide. The gold ball's thermal resistance to the back gate is going to depend on the cross-section of the ball, which in figure 6.6 is initially a 90 nm diameter disk. The thermal resistance through the oxide for the gold ball is thus roughly $\frac{t}{kA} \approx \frac{200nm}{(1W/°Cm)\pi(45nm)^2} \approx 3 * 10^7\ °C/W$, where t is the thickness of the oxide, k is the thermal conductivity of silicon dioxide, and A is the area.[6]. The energy dissipated near the contacts will be thermally shunted by the contacts low thermal resistance to the back gate. A system with thermal resistance $3 * 10^7\ °C/W$ requires 30 μW of power to reach 1060°C. Since the gold melted, we conclude of the 300 μW of power being dumped into the system, at least 30 μW were being shed by the gold.

We've shown that it is possible to melt small gold deposits on nanotubes with resistive heating. During the melting of the deposits, some of the gold

[4]The exaggerated height scale of AFM makes the deposits look like balls. In actuality, they are more like hockey-puck patties of gold. We thus model them as simple cylinders.

[5]Although nanosized particles have a suppressed melting point compared to the bulk, this effect for metal does not become relevant factor until sizes are less than 10 nm[96].

[6]This is orders of magnitude smaller than the thermal resistance for the gold ball through the tube, the tube's resistance through the oxide, and thermal resistances through the air

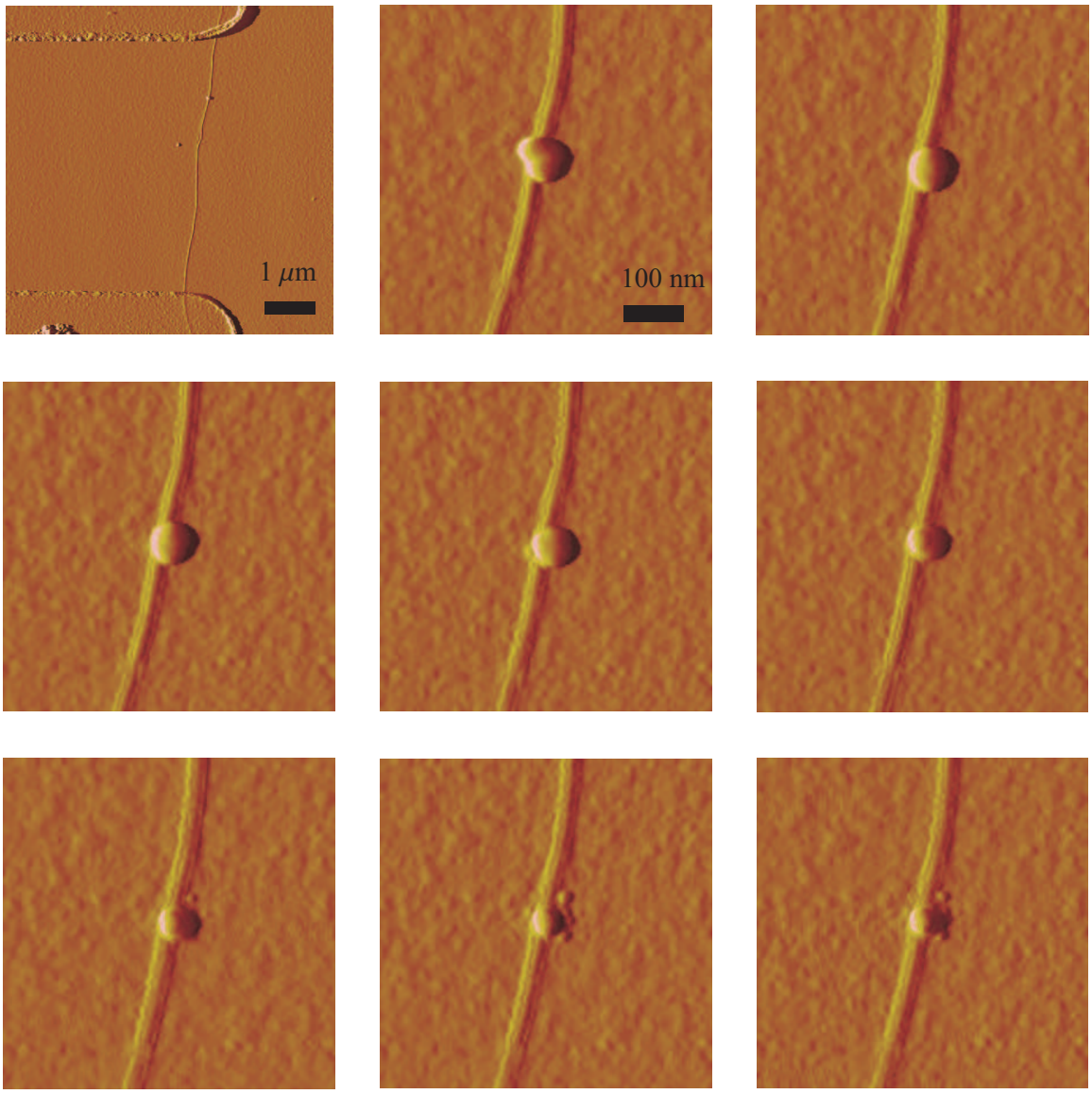

Figure 6.6: Sequence of images showing gold melting and moving on a 2.4 nm nanotube. Upper left shows a nanotube bridging two electrical contacts with a blob of deposited gold, scale bar 1 μm. The rest of the images (all scale bar 100 nm) show the structure of the gold ball changing as it is heated. First the asymmetrical blob becomes more round, then it shrinks and kicks off small balls of gold. The large voltages involved in melting the gold interfere with clean AFM imaging, but pausing the heating allowed images that show clear changes to be acquired.

moved away from the deposit, alloying us to change the mass of the deposit smoothly over femtograms. This extends previous work on suspended carbon nanotube atomic conveyer belts to tubes on non-suspended tubes. We now look at melting larger amounts of gold, and how that interacts with a nanotube.

6.5 Coating a nanotube with gold

We turn now from melting small amounts of gold on a nanotube to melting large amounts of gold on a nanotube. The larger gold reservoir will require additional heating, but gives us the opportunity to see the gold moving along the nanotube. By flowing gold along a tube, we can create gold nanowire sheaths along the tube. An eventual application might be extruding and retracting a cover over a nanotube in a sensor, or a surface mounted nanomotor without requiring AFM deposition. This section lays the groundwork for those applications, and looks at coating a nanotube with a nanometer-scale sheath of gold.

Figure 6.7 shows a schematic of the devices used in this (and the next) section. It's our standard nanotube transistor, with an added gold wire. The gold wire with large pads for electrical contact is deposited across the nanotube device using standard lithographic techniques. The wires here are 1 nm chrome adhesion layer and 20 nm gold.

We make electrical contact to the wire, and flow enough current through the wire to make it melt (~ 10 mA, ~ 20 mW). The nanotube passes under the melting wire. The ends of the nanotube are thermally grounded by the electrical contacts. The thermal gradient along the tube from the melting wire to the electrical contacts can cause gold in the wire to move out along the tube ([106],

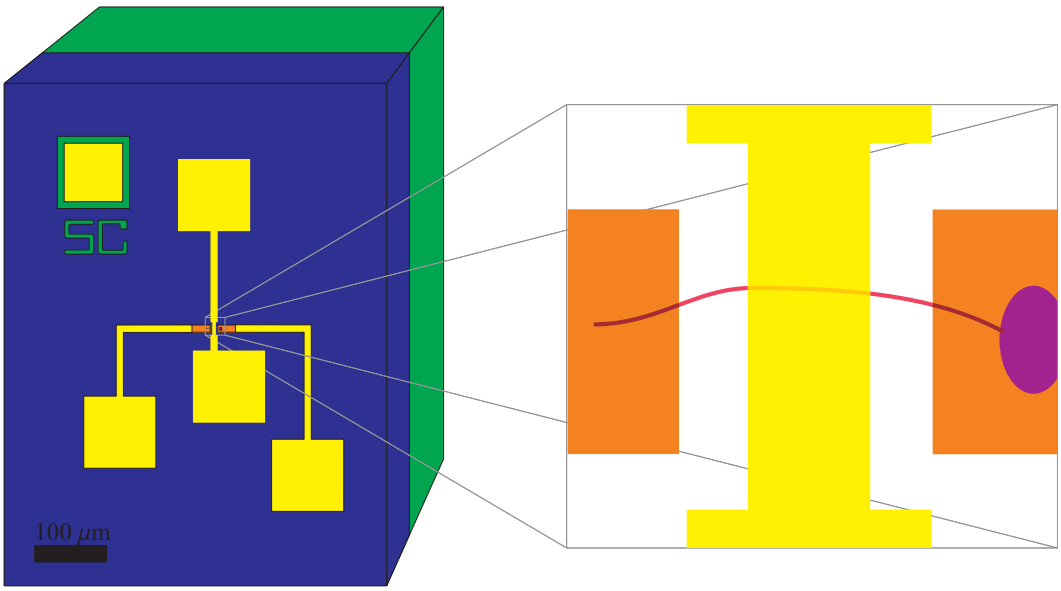

Figure 6.7: Schematic of a nanotube transistor crossed by a gold wire. Green is degenerately doped silicon back gate, also visible in back gate contact and device label. Blue is 200 nm layer of silicon dioxide. Gold is contact pads for nanotube and the break junction wire and pads. Orange is palladium for electrical contact to nanotube. Purple is catalyst. Nanotube shown in red. Expanded area shows a closer look at the nanotube section.

[5]).

Figure 6.8 shows the before and after images of a nanotube under a melted wire. The wire runs vertically, with the wider part visible at the top of the image. The nanotube crosses the wire and is connected to two electrical contacts, one of which is visible in the bottom right corner. Both ends of the nanotube were ramped to -5 V. The wire was ramped to 2.5 V, and broke at a current of 8.5 mA. When the wire broke, gold in the wire melted, and some of it moved from the wire to the nanotube. It is not clear why gold flowed out onto the nanotube on only one side of the wire. In this sample, the gold flowed onto the side with a longer distance of nanotube between wire and contact (10 μm compared to 5

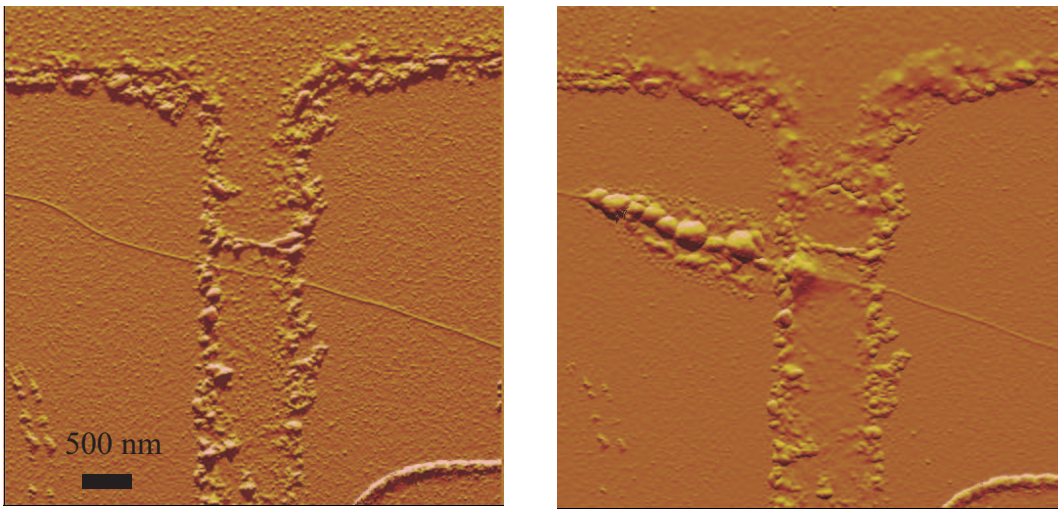

Figure 6.8: Gold that moved onto a nanotube from a melted wire. On the left, an AFM image before passing a current through the wire. The wire runs vertically (visible at the top is where the wire widens, refer to figure 6.7). The nanotube spans two electrical contacts (one visible at bottom right) and crosses the wire. On the right, AFM image after passing a current the wire. Gold has moved onto the nanotube to the left of the wire. The gold in the wire has also melted and smoothed. Scale bar 500 nm.

μm, total tube length not shown).

Figure 6.9 shows the after image of a melted wire with a nanotube under it. The wire runs vertically, and the nanotube runs horizontally between two electrical contacts. We drove 12 mA of current through the wire for 450 seconds before it broke. The gold in the wire melted over the length of the wire, and piled up near the nanotube. The pile-up of gold is more visible in the height image on the left, but the smooth structure of the melted wire is more visible on the amplitude image on the right. To the left of the wire, the nanotube is 4 nm high. To the right of the wire, the nanotube is 6 nm high. Gold has flowed from the wire and coated the right side of the nanotube. The nanotube provided a

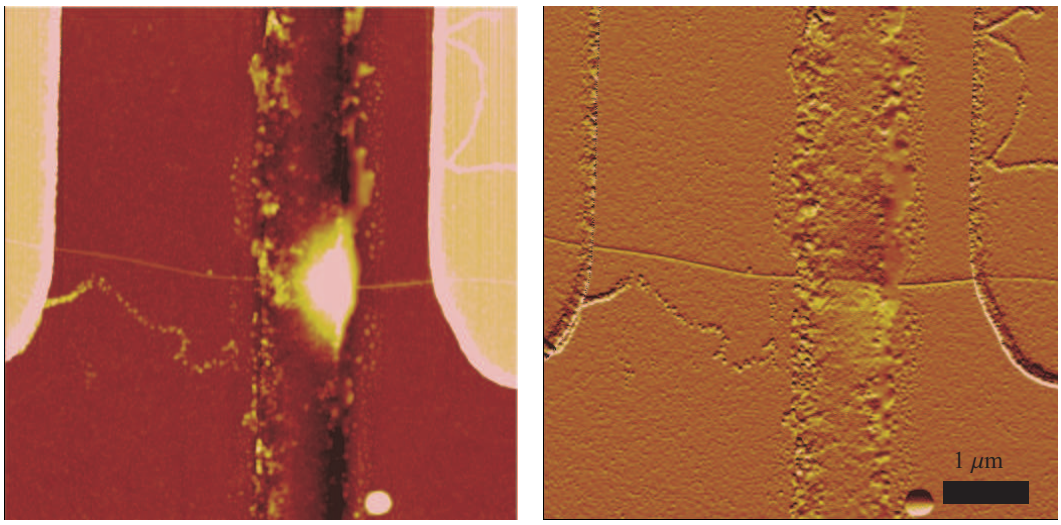

Figure 6.9: Gold from a melted wire coating a nanotube. The wire runs vertically. The nanotube crosses horizontally, and bridges two electrodes. The image on the left is height. The piled up gold on the wire is 70 nm high. The image on the right is amplitude, showing the smoother surface of the melted gold. The chain of dots between the wire and left contact are photoresist residue and do not conduct. Scale bar 1 μm.

scaffolding for the gold to move away from the wire.[7] The pile-up of gold near the nanotube indicates that there was a thermal gradient in the melting wire that drove gold to near the tube. The small gold balls off the side of the wire are all within a few hundred nanometers of the wire. The gold on the right side of the nanotube has traveled a micron to completely coat that section of nanotube. We've thus shown that melting a gold wire can be used to create a gold nanowire along a nanotube.

[7] In all of the cases where gold moved from the wire onto the nanotube, it only moved off one side of the wire.

6.6 Nanogaps in wires around nanotubes

In addition to being coated in gold when a wire melts, a nanotube can also influence the formation of the break in the wire when it fails. Researchers deliberately make wires fail to generate small gaps in those wires [88] as an investigative tool for molecules that put into those gaps [81]. The gaps in these wires often vary significantly from sample to sample and are difficult to control [121]. There is often little control over where along the length of the wire the gap will form. We want additional control over the location and character of the break in the wire. We show that we can form the break in the wire at the nanotube. This creates the opportunity of having the nanotube inside a small gap between two metal wires (a theoretical system that's attracted interest [146], [86], [67]), or provides a nanotube wire in a gap where other molecules are being studied. This section uses the same device geometry as the previous section, see figure 6.7.

Figure 6.10 shows an example of a gap in a wire that formed where the nanotube crosses the wire. The AFM image on the left shows the wire running vertically between two electrical contacts to the nanotube. The 1 nm diameter tube links the two electrical contacts and passes under the wire. To break the wire, the nanotube potential was set to -6 V and the back gate was set to -5 V, one end of the wire was grounded, and the voltage on the other end was ramped to -5 V. (The critical current was 14 mA). The initial 26 μS conductance of the nanotube decreased to 18 μS, but the tube did conduct after breaking the wire.

The break in the wire is difficult to see, but we can highlight the break using electric force microscopy (refer to section 5.4.3 for a discussion of EFM). In the

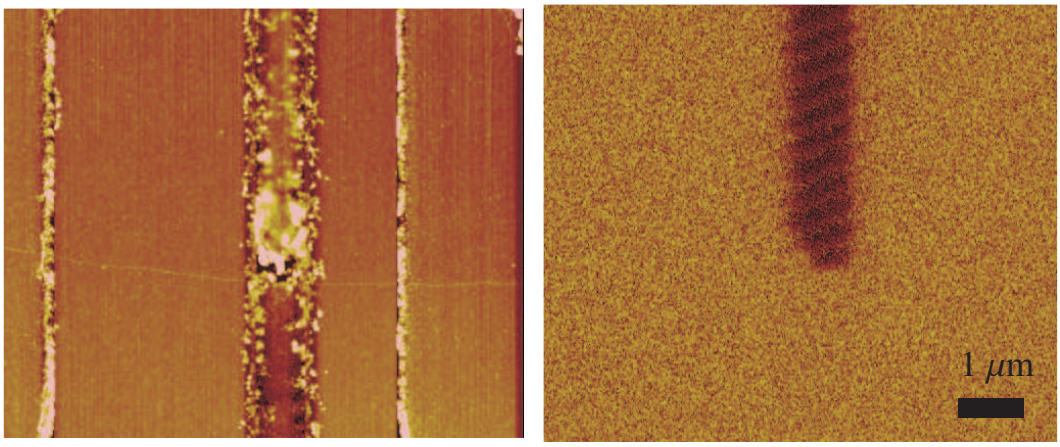

Figure 6.10: Nanogap in wire at nanotube. The image on the left is an AFM tapping mode image. The image on the right is an EFM image. In the AFM image, the broken wire runs top to bottom, crossed by a nanotube. The electrical contacts to the nanotube are visible at the sides of the image. In the right EFM image, an AC voltage was applied to the top contact of the break junction wire. The EFM tip measures the local potential, highlighting the break in the wire at the nanotube.

right EFM image, a voltage was applied to the top contact of the broken wire. The EFM tip measures the local potential. The section of wire on the bottom visible in the tapping mode image but not the EFM image is not electrically connected to the section of wire at the top, which highlights were the break in the wire occurred. This break overlaps the nanotube that crosses under the wire.

We found that the best way to have the gap form at the nanotube was to pass a current from the wire to the tube while running enough current through the wire to break the wire. A rapid ramp in the voltage across the wire made clean breaks more likely. A slow ramp of the voltage, or holding the voltage slightly below the critical voltage, gave a slow melt of the wire that was more likely to create a gold-coated nanotube and have the break in the wire be away from the tube (as in section 6.5). Sudden changes in voltage can damage or

destroy nanotubes, and the voltage profile of the wire when it breaks changes quite rapidly. We found that the best way to not destroy tubes while breaking the wire was to set both ends of the nanotube at the same voltage, and have that voltage be the midpoint voltage of the expected break voltage of the wire. Doing so makes the unbroken wire passes a current to the nanotube while minimizing the total change of voltage across the tube when the wire breaks.

We've shown that the we can break a wire where it crosses a nanotube, creating a nanotube-in-a-gap geometry. Now that a proof-of-principle has been established, implementation of this technique to study nanotubes in the gap or use the nanotube to study other molecules in the gap can be carried out. Future iterations of this research may benefit from using thinner gold wires that break at lower currents (so that the currents that can be driven through the nanotube are a larger fraction of the total currents).

6.7 Conclusions

This chapter showed that it is possible to locally deposit gold onto a carbon nanotube with an AFM tip. The conductance of the nanotube can be left unchanged, but we do not have complete control of the process. Multiple depositions per nanotube are possible, as is depositing at the junction of multiple tubes. This work is similar to work recently published by another group [17], but this chapter utilized the deposited gold balls in ways not reported in that paper.

The gold balls were melted and gold moved by Joule heating, a previously accomplished result ([98], [5]) that we extended to nanotubes on a surface. We also looked at melting macroscopic amounts of gold near nanotubes, which re-

sulted in coating the tube with a sheath of gold. The applications of atomic conveyor belts[143] and nanomotors [97] are thus more promising as they no longer require suspended systems.

We demonstrated that we can correlate the location of nanometer-sized gaps in a wire with the position of a nanotube crossing the wire. This offers the exciting possibility of having a nanotube inside of a nanometer-sized gap ([146], [86], [67], [81]).

CHAPTER 7

SUMMARY

This thesis comprised several experiments carried out on carbon nanotube transistors. We sketched the basic theory of carbon nanotubes, their structure and electronic properties, in chapter 2. We gave extra attention to the band structure of the nanotube, as the first experiment gave us the opportunity to experimentally probe that structure.

Our fabrication for carbon nanotube transistors was described in chapter 3. We discussed nanotube growth and the lithographic steps required for electrical contact. We gave a detailed description of the fabrication of self-aligned top gates from one lithographic step.

Chapter 4 discussed capacitance measurements of carbon nanotubes. These measurements showed that to first order, the nanotube can be modeled as a simple conductor embedded in a dielectric. Our experiment went further, and had enough accuracy to see rich structure in capacitance of a carbon nanotube. This provided a probe of the tube's density of states. We compared the measured and expected structure, and saw deviations that could come from electron-electron correlations. Capacitance measurements of nanotube systems with different parameters thus offer an interesting testing ground to investigate electron-electron correlations and the resulting negative capacitance. The techniques developed can also be used in the growing fields of semiconducting nanowires and graphene nanoribbons, providing a myriad of opportunities in both fundamental physics and future applications for all these classes of devices.

The remaining experiments were more about interactions with nanotubes than fundamental physics. In chapter 5 we looked at locally damaging a carbon nanotube with an oxygen plasma. We showed it is possible to burn large (for a nanotube) holes into the tube, but still have the tube conduct. The dangling bonds at the edges of the hole offer interesting possibilities for attaching functionalized chemical groups or heightening sensitivity of a carbon-nanotube-based sensor. Cutting holes into nanotubes without completely destroying the electrical conductivity also gives a pathway to nanopipes that, while carrying molecules, can sustain electrical currents or fields to drive or probe the passenger molecules. This is particularly exciting in parallel with recent advancements in aligned arrays of long tubes [55], which could allow nanopipelines in parallel for increased throughput.

Chapter 6 covered several experiments using carbon nanotubes as a scaffold for mobile gold. Gold was deposited onto tubes from an atomic force microscope using electromigration. We showed preliminary results of the small gold balls being used as a catalyst for semiconducting nanowires. We showed it was possible to melt the gold balls with Joule heating. We made molten gold flow along the nanotube, extending previous work on nanotubes as atomic conveyors [98] to systems where the tube is on a surface. We used the movement of molten gold along a tube create a gold sheath around the nanotube. We also showed that carbon nanotubes can have an influence on gap formation in micron-sized wires broken with electromigration. The additional control of gap formation could have potentially useful applications involving carbon nanotubes in nanometer-sized gaps. The tubes could either be the subject of study under transverse electric fields, or serve as an additional wire or sensor to study other molecules inside the gap.

BIBLIOGRAPHY

[1] Haroon Ahmed. Single electron electronics: Challenge for nanofabrication. volume 15, pages 2101–2108. AVS, 1997.

[2] Hiroshi Ajiki and Tsuneya Ando. Electronic states of carbon nanotubes. *Journal of the Physical Society of Japan*, 62(4):1255–1266, 1993.

[3] Phaedon Avouris, Marcus Freitag, and Vasili Perebeinos. Carbon-nanotube photonics and optoelectronics. *Nat Photon*, 2(6):341–350, June 2008.

[4] A. Bachtold, M. S. Fuhrer, S. Plyasunov, M. Forero, Erik H. Anderson, A. Zettl, and Paul L. McEuen. Scanned probe microscopy of electronic transport in carbon nanotubes. *Phys. Rev. Lett.*, 84(26):6082–6085, Jun 2000.

[5] Amelia Barreiro, Riccardo Rurali, Eduardo R. Hernandez, Joel Moser, Thomas Pichler, Laszlo Forro, and Adrian Bachtold. Subnanometer Motion of Cargoes Driven by Thermal Gradients Along Carbon Nanotubes. *Science*, 320(5877):775–778, 2008.

[6] M. S. Bello, E. I. Levin, B. I. Shklovskii, and A. L. Efros. Density of localized states in the surface impurity band of a metal-dielectric-semiconductor structure. *Journal of experimental and theoretical physics*, 53(822), 1981.

[7] M. Bockrath, D. H. Cobden, A. G. Rinzler, R. E. Smalley, L. Balents, and P. L. McEuen. Luttinger liquid behavior in carbon nanotubes. *Nature*, 397:598, 1999.

[8] M. W. Bockrath. *Carbon Nanotubes: Electrons in One Dimension*. PhD thesis, University of California, Berkeley, 1999.

[9] S. Boussaad, N. J. Tao, R. Zhang, T. Hopson, and L. A. Nagahara. *In situ* detection of cytochrome c adsorption with single walled carbon nanotube device. *Chem. Commun.*, 13:1502, 2003.

[10] David Boyer, Philippe Tamarat, Abdelhamid Maali, Brahim Lounis, and Michel Orrit. Photothermal Imaging of Nanometer-Sized Metal Particles Among Scatterers. *Science*, 297(5584):1160–1163, 2002.

[11] Markus Brink. *Imaging Single-Electron Charging in Nanostructures*. PhD thesis, Cornell University, 2007.

[12] Hong Cai, Xuni Cao, Ying Jiang, Pingang He, and Yuzhi Fang. Carbon nanotube-enhanced electrochemical DNA biosensor for DNA hybridization detection. *Anal. Bioanal. Chem.*, 375:287, 2003.

[13] J. Y. Chen, A. Kutana, C. P. Collier, and K. P. Giapis. Electrowetting in Carbon Nanotubes. *Science*, 310(5753):1480–1483, 2005.

[14] R. J. Chen, H. C. Choi, S. Bangasaruntip, E. Yenilmez, X. Tang, Q. Wang, Y.-L. Chang, and H. Dai. An investigation of the mechanisms of electronic sensing of protein adsorption on carbon nanotube devices. *J. Am. Chem. Soc.*, 126:1563, 2004.

[15] Robert J. Chen, Sarunya Bangsaruntip, Katerina A. Drouvalakis, Nadine Wong Shi Kam, Moonsub Shim, Yiming Li, Woong Kim, Paul J. Utz, and Hongjie Dai. Noncovalent functionalization of carbon nanotubes for highly specific electronic biosensors. *Proc. Natl. Acad. Sci. U.S.A.*, 100:4984, 2003.

[16] Zhihong Chen, Yu-Ming Lin, Michael J. Rooks, and Phaedon Avouris. Graphene nano-ribbon electronics. *Physica E: Low-dimensional Systems and Nanostructures*, 40(2):228 – 232, 2007. International Symposium on Nanometer-Scale Quantum Physics.

[17] Haibin Chu, Zhong Jin, Yan Zhang, Weiwei Zhou, Lei Ding, and Yan Li. Site-specific deposition of gold nanoparticles on swnts. *The Journal of Physical Chemistry C*, 112(35):13437–13441, 2008.

[18] David H. Cobden, Marc Bockrath, Paul L. McEuen, Andrew G. Rinzler, and Richard E. Smalley. Spin splitting and even-odd effects in carbon nanotubes. *Phys. Rev. Lett.*, 81(3):681–684, Jul 1998.

[19] Philip G. Collins, Michael S. Arnold, and Phaedon Avouris. Engineering Carbon Nanotubes and Nanotube Circuits Using Electrical Breakdown. *Science*, 292(5517):706–709, 2001.

[20] T. P. Darby and C. M. Wayman. Nucleation and growth of gold films on graphite : I. effects of substrate condition and evaporation rate. *Journal of Crystal Growth*, 28(1):41 – 52, 1975.

[21] F. Lamari Darkrim, P. Malbrunot, and G. P. Tartaglia. Review of hydrogen storage by adsorption in carbon nanotubes. *International Journal of Hydrogen Energy*, 27(2):193 – 202, 2002.

[22] S. Datta. *Electron Transport in Mesoscopic Systems*. Cambridge University Press, New York, NY, 1995.

[23] V. Derycke, R. Martel, J. Appenzeller, and Ph. Avouris. Carbon nanotube inter- and intramolecular logic gates. *Nano Letters*, 1(9):453–456, 2001.

[24] Vikram V. Deshpande, Bhupesh Chandra, Robert Caldwell, Dmitry S. Novikov, James Hone, and Marc Bockrath. Mott Insulating State in Ultraclean Carbon Nanotubes. *Science*, 323(5910):106–110, 2009.

[25] A. C. Dillon, K. M. Jones, T. A. Bekkedahl, C. H. Kiang, D. S. Bethune, and M. J. Heben. Storage of hydrogen in single-walled carbon nanotubes. *Nature*, 386(6623):377–379, March 1997.

[26] Lei Ding, Alexander Tselev, Jinyong Wang, Dongning Yuan, Haibin Chu, Thomas P. McNicholas, Yan Li, and Jie Liu. Selective growth of well-aligned semiconducting single-walled carbon nanotubes. *Nano Letters*, preprint(ASAP), 2009.

[27] Lixin Dong, Xinyong Tao, Li Zhang, Xiaobin Zhang, and Bradley J. Nelson. Nanorobotic spot welding: Controlled metal deposition with attogram precision from copper-filled carbon nanotubes. *Nano Letters*, 7(1):58–63, 2007.

[28] A. L. Efros. Density of states of 2d electron gas and width of the plateau of iqhe. *Solid State Communications*, 65(11):1281–1284, March 1988.

[29] J. Fernandez-Rossier, J. J. Palacios, and L. Brey. Electronic structure of gated graphene and graphene ribbons. *Physical Review B (Condensed Matter and Materials Physics)*, 75(20):205441, 2007.

[30] Michael M. Fogler. Ground-state energy of the electron liquid in ultrathin wires. *Phys. Rev. Lett.*, 94(5):056405–4, February 2005.

[31] A. K. Geim and K. S. Novoselov. The rise of graphene. *Nat Mater*, 6(3):183–191, March 2007.

[32] L. I. Glazman, I. M. Ruzin, and B. I. Shklovskii. Quantum transport and

pinning of a one-dimensional wigner crystal. *Phys. Rev. B*, 45(15):8454–8463, Apr 1992.

[33] Andreas Gruneis, Maria J. Esplandiu, Daniel Garcia-Sanchez, and Adrian Bachtold. Detecting individual electrons using a carbon nanotube field-effect transistor. *Nano Letters*, 7(12):3766–3769, 2007.

[34] Jing Guo, Youngki Yoon, and Yijian Ouyang. Gate electrostatics and quantum capacitance of graphene nanoribbons. *Nano Letters*, 7(7):1935–1940, 2007.

[35] X. Guo, J. Small, J. E.Klare, Y. Wang, M. S. Purewal, I. W. Tam, B. H. Hong, R. Caldwell, L. Huang, S. O'Brien, J. Yan, R. Breslow, S. J. Wind, J. Hone, P. Kim, and C. Nuckolls. Covalently Bridging Gaps in Single-Walled Carbon Nanotubes with Conducting Molecules. *Science*, 311(5759):356–359, 2006.

[36] H. R. Gutierrez, U. J. Kim, J. P. Kim, and P. C. Eklund. Thermal conversion of bundled carbon nanotubes into graphitic ribbons. *Nano Letters*, 5(11):2195–2201, 2005.

[37] F. D. M. Haldane. Effective harmonic-fluid approach to low-energy properties of one-dimensional quantum fluids. *Phys. Rev. Lett.*, 47(25):1840.

[38] Noriaki Hamada, Shin-ichi Sawada, and Atsushi Oshiyama. New one-dimensional conductors: Graphitic microtubules. *Phys. Rev. Lett.*, 68(10):1579–1581, Mar 1992.

[39] Melinda Y. Han, Barbaros Özyilmaz, Yuanbo Zhang, and Philip Kim. Energy band-gap engineering of graphene nanoribbons. *Phys. Rev. Lett.*, 98(20):206805, 2007.

[40] H. B. Heersche, Z. de Groot, J. A. Folk, L. P. Kouwenhoven, and H. S. J. van der Zant. Kondo effect in the presence of magnetic impurities. *Phys. Rev. Lett.*, 96:017205, 2006.

[41] Michael Hirscher, Marion Becher, Miroslav Haluska, Frank von Zeppelin, Xiahong Chen, Urszula Dettlaff-Weglikowska, and Siegmar Roth. Are carbon nanostructures an efficient hydrogen storage medium? *Journal of Alloys and Compounds*, 356-357:433 – 437, 2003. Proceedings of the Eighth International Symposium on Metal-Hydrogen Systems, Fundamentals and Applications (MH2002).

[42] P. S. Ho and T. Kwok. Electromigration in metals. *Reports on Progress in Physics*, 52(3):301–348, 1989.

[43] A. A. Houck, J. Labaziewicz, E. K. Chan, J. A. Folk, and I. L. Chuang. Kondo effect in electromigrated gold break junctions. *Nano Lett.*, 5:1685, 2005.

[44] S. Huang, M. Woodson, R. Smalley, and J. Liu. Growth mechanism of oriented long single walled carbon nanotubes using "fast-heating" chemical vapor deposition process. *Nano Lett.*, 4:1025, 2004.

[45] Sumio Iijima. Helical microtubules of graphitic carbon. *Nature*, 354:56, 1991.

[46] S. Ilani, L. A. K. Donev, M. Kindermann, and P. L. McEuen. Measurement of the quantum capacitance of interacting electrons in carbon nanotubes. *Nature Physics*, 2(10):687–691, October 2006.

[47] P. Jarillo-Herrero, J. Kong, H. S. J. van der Zant, C. Dekker, L. P. Kouwenhoven, and S. De Franceschi. Electronic transport spectroscopy of carbon nanotubes in a magnetic field. *Phys. Rev. Lett.*, 94(15):156802, Apr 2005.

[48] Pablo Jarillo-Herrero, Sami Sapmaz, Cees Dekker, Leo P. Kouwenhoven, and Herre S. J. van der Zant. Electron-hole symmetry in a semiconducting carbon nanotube quantum dot. *Nature*, 429(6990):389–392, May 2004.

[49] Manfred Jaschke and Hans-Juergen Butt. Deposition of organic material by the tip of a scanning force microscope. *Langmuir*, 11(4):1061–1064, 1995.

[50] Ali Javey, Jing Guo, Damon B. Farmer, Qian Wang, Erhan Yenilmez, Roy G. Gordon, Mark Lundstrom, and Hongjie Dai. Self-aligned ballistic molecular transistors and electrically parallel nanotube arrays. *Nano Letters*, 4(7):1319–1322, 2004.

[51] Ali Javey, Jing Guo, Qian Wang, Mark Lundstrom, and Hongjie Dai. Ballistic carbon nanotube field-effect transistors. *Nature*, 424:654, 2003.

[52] W. Jiang, G. Nadeau, K. Zaghib, and K. Kinoshita. Thermal analysis of the oxidation of natural graphite – effect of particle size. *Thermochimica Acta*, 351(1-2):85 – 93, 2000.

[53] Ado Jorio, Gene Dresselhaus, and Mildred S. Dresselhaus. *Carbon Nanotubes: Advanced Topics in the Synthesis, Structure, Properties and Applications (Topics in Applied Physics)*. Springer, 1 edition, March 2008.

[54] C. L. Kane and E. J. Mele. Size, shape, and low energy electronic structure of carbon nanotubes. *Phys. Rev. Lett.*, 78:1932, 1997.

[55] Seong Jun Kang, Coskun Kocabas, Taner Ozel, Moonsub Shim, Ninad Pimparkar, Muhammad A. Alam, Slava V. Rotkin, and John A. Rogers. High-performance electronics using dense, perfectly aligned arrays of single-walled carbon nanotubes. *Nat Nano*, 2(4):230–236, April 2007.

[56] Kanghyun Kim, Hyung Ju Park, Byung-Chill Woo, Kook Jin Kim, Gyu Tae Kim, and Wan Soo Yun. Electric property evolution of structurally defected multilayer graphene. *Nano Letters*, 8(10):3092–3096, 2008.

[57] J. Kong, A. M. Cassell, and H. Dai. Chemical vapor deposition of methane for single-walled carbon nanotubes. *Chem. Phys. Lett.*, 292:567, 1998.

[58] J. Kong, N. R. Franklin, C. Zhou, M. G. Chapline, S. Peng, K. Cho, and H. Dai. Nanotube molecular wires as chemical sensors. *Science*, 287:622, 2000.

[59] J. Kong, E. Yenilmez, T. W. Tombler, W. Kim, H. Dai, R. B. Laughlin, L. Liu, C. S. Jayanthi, and S. Y. Wu. Quantum interference and ballistic transport in nanotube electron waveguides. *Phys. Rev. Lett.*, 87:106801, 2001.

[60] Masanori Koshino, Takatsugu Tanaka, Niclas Solin, Kazutomo Suenaga, Hiroyuki Isobe, and Eiichi Nakamura. Imaging of Single Organic Molecules in Motion. *Science*, 316(5826):853–, 2007.

[61] A. V. Krasheninnikov and F. Banhart. Engineering of nanostructured carbon materials with electron or ion beams. *Nat Mater*, 6(10):723–733, October 2007.

[62] M. Krüger, I. Widmer, T. Nussbaumer, M. Buitelaar, and C. Schönenberger. Sensitivity of single multiwalled carbon nanotubes to the environment. *New J. Phys.*, 5:138, 2003.

[63] Lisa Larrimore. *Chemical and Biological Sensing with Carbon Nanotubes in Solution*. PhD thesis, 2008.

[64] L. Latessa, A. Pecchia, A. Di Carlo, and P. Lugli. Negative quantum capacitance of gated carbon nanotubes. *Physical Review B (Condensed Matter and Materials Physics)*, 72(3):035455–5, July 2005.

[65] Matt Law, Joshua Goldberger, and Peidong Yang. Semiconductor nanowires and nanotubes. *Annual Review of Materials Research*, 34(1):p83 – C–2, 20040801.

[66] Jun Li, Hou Tee Ng, Alan Cassell, Wendy Fan, Hua Chen, Qi Ye, Jessica Koehne, Jie Han, and M. Meyyappan. Carbon nanotube nanoelectrode array for ultrasensitive DNA detection. *Nano Lett.*, 3:597, 2003.

[67] Yan Li, Slava V. Rotkin, and Umberto Ravaioli. Electronic response and bandstructure modulation of carbon nanotubes in a transverse electrical field. *Nano Letters*, 3(2):183–187, 2003.

[68] W. J. Liang, M. P. Shores, M. Bockrath, J. R. Long, and H. Park. Kondo resonance in a single-molecule transistor. *Nature*, 417:725, 2002.

[69] David R. Lide, editor. *CRC Handbook of Chemistry and Physics*. CRC Press, Cleveland, OH, 87th edition, 2006.

[70] Zheng Liu, Masanori Koshino, Kazu Suenaga, Aleš Mrzel, Hiromichi Kataura, and Sumio Iijima. Transmission electron microscopy imaging of individual functional groups of fullerene derivatives. *Phys. Rev. Lett.*, 96(8):088304, 2006.

[71] G. D Mahan. *Many-Particle Physics*. Plenum, New York, 1990.

[72] David Mann, Ali Javey, Jing Kong, Qian Wang, and Hongjie Dai. Ballistic transport in metallic nanotubes with reliable pd ohmic contacts. *Nano Letters*, 3(11):1541–1544, 2003.

[73] R. Martel, V. Derycke, C. Lavoie, J. Appenzeller, K. K. Chan, J. Tersoff, and Ph. Avouris. Ambipolar electrical transport in semiconducting single-wall carbon nanotubes. *Phys. Rev. Lett.*, 87(25):256805, Dec 2001.

[74] R. Martel, T. Schmidt, H. R. Shea, T. Hertel, and Ph. Avouris. Single- and multi-wall carbon nanotube field-effect transistors. *Appl. Phys. Lett.*, 73(17):2447–2449, 1998.

[75] Yves Martin, David W. Abraham, and H. Kumar Wickramasinghe. High-resolution capacitance measurement and potentiometry by force microscopy. *Appl. Phys. Lett.*, 52(13):1103–1105, 1988.

[76] Paul L. McEuen, Marc Bockrath, David H. Cobden, Young-Gui Yoon, and Steven G. Louie. Disorder, pseudospins, and backscattering in carbon nanotubes. *Phys. Rev. Lett.*, 83(24):5098–5101, Dec 1999.

[77] Aneta J. Mieszawska, Romaneh Jalilian, Gamini U. Sumanasekera, and Francis P. Zamborini. Synthesis of gold nanorod/single-wall carbon nanotube heterojunctions directly on surfaces. *Journal of the American Chemical Society*, 127(31):10822–10823, 2005.

[78] E. D. Minot, Yuval Yaish, Vera Sazonova, Ji-Yong Park, Markus Brink, and Paul L. McEuen. Tuning carbon nanotube band gaps with strain. *Phys. Rev. Lett.*, 90:156401, 2003.

[79] Ethan Minot. *Tuning the Band Structure of Carbon Nanotubes*. PhD thesis, Cornell University, 2004.

[80] L. E. Murr, K. F. Soto, E. V. Esquivel, J. J. Bang, P. A. Guerrero, D. A. Lopez, and D. A. Ramirez. Carbon nanotubes and other fullerene-related nanocrystals in the environment: A TEM study. *JOM*, 56:28, 2004.

[81] D. Natelson, L. H. Yu, J. W. Ciszek, Z. K. Keane, and J. M. Tour. Single-molecule transistors: Electron transfer in the solid state. *Chem. Phys.*, 324:267, 2006.

[82] A. Nikitin, H. Ogasawara, D. Mann, R. Denecke, Z. Zhang, H. Dai, K. Cho, and A. Nilsson. Hydrogenation of single-walled carbon nanotubes. *Phys. Rev. Lett.*, 95(22):225507, 2005.

[83] K. S. Novoselov, A. K. Geim, S. V. Morozov, D. Jiang, M. I. Katsnelson, I. V. Grigorieva, S. V. Dubonos, and A. A. Firsov. Two-dimensional gas of massless dirac fermions in graphene. *Nature*, 438(7065):197–200, November 2005.

[84] K. S. Novoselov, A. K. Geim, S. V. Morozov, D. Jiang, Y. Zhang, S. V. Dubonos, I. V. Grigorieva, and A. A. Firsov. Electric Field Effect in Atomically Thin Carbon Films. *Science*, 306(5696):666–669, 2004.

[85] T. W. Odom, J.-L. Huang, P. Kim, and C. Lieber. Atomic structure and

electronic properties of single-walled carbon nanotubes. *Nature*, 391:62, 1998.

[86] James O'Keeffe, Chengyu Wei, and Kyeongjae Cho. Bandstructure modulation for carbon nanotubes in a uniform electric field. *Appl. Phys. Lett.*, 80(4):676–678, 2002.

[87] J. J. Palacios, P. Tarakeshwar, and Dae M. Kim. Metal contacts in carbon nanotube field-effect transistors: Beyond the schottky barrier paradigm. *Physical Review B (Condensed Matter and Materials Physics)*, 77(11):113403, 2008.

[88] H. Park, A. K. L. Lim, A. P. Alivisatos, J. Park, and P. L. McEuen. Fabrication of metallic electrodes with nanometer separation by electromigration. *Appl. Phys. Lett.*, 75:301, 1999.

[89] J. Park, A. N. Pasupathy, J. I. Goldsmith, C. Chang, Y. Yaish, J. R. Petta, M. Rinkoski, J. P. Sethana, H. D. Abruña, P. L. McEuen, and D. C. Ralph. Coulomb blockade and the kondo effect in single-atom transistors. *Nature*, 417:722, 2002.

[90] Ji-Yong Park, Sami Rosenblatt, Yuval Yaish, Vera Sazonova, Hande Ustunel, Stephan Braig, T. A. Arias, Piet W. Brouwer, and Paul L. McEuen. Electron-phonon scattering in metallic single-walled carbon nanotubes. *Nano Letters*, 4(3):517–520, 2004.

[91] Ji-Yong Park, Yuval Yaish, Markus Brink, Sami Rosenblatt, and Paul L. McEuen. Electrical cutting and nicking of carbon nanotubes using an atomic force microscope. *Appl. Phys. Lett.*, 80(23):4446–4448, 2002.

[92] D. G. Pierce and P. G. Brusius. Electromigration: A review. *Microelectronics and Reliability*, 37(7):1053 – 1072, 1997. Reliability Physics of Advanced Electron Devices.

[93] Richard D. Piner, Jin Zhu, Feng Xu, Seunghun Hong, and Chad A. Mirkin. "Dip-Pen" Nanolithography. *Science*, 283(5402):661–663, 1999.

[94] E. P. De Poortere, H. L. Stormer, L. M. Huang, S. J. Wind, S. O'Brien, M. Huang, and J. Hone. Single-walled carbon nanotubes as shadow masks for nanogap fabrication. *Appl. Phys. Lett.*, 88(14):143124, 2006.

[95] Hendrik Willem Christiaan Postma. *Carbon nanotube junctions and devices*. PhD thesis, Delft University of Technology, 2001.

[96] Yang Quan-Wen, Zhu Ru-Zeng, Wei Jiu-An, and Wen Yu-Hua. Surface-induced melting of metal nanoclusters. *Chin. Phys. Lett.*, 21(11):2171–2174, 2004.

[97] B. C. Regan, S. Aloni, K. Jensen, R. O. Ritchie, and A. Zettl. Nanocrystal-powered nanomotor. *Nano Letters*, 5(9):1730–1733, 2005.

[98] B. C. Regan, S. Aloni, R. O. Ritchie, U. Dahmen, and A. Zettl. Carbon nanotubes as nanoscale mass conveyors. *Nature*, 428(6986):924–927, April 2004.

[99] M. Reibold, P. Paufler, A. A. Levin, W. Kochmann, N. Patzke, and D. C. Meyer. Materials: Carbon nanotubes in an ancient damascus sabre. *Nature*, 444(7117):286, November 2006.

[100] S. Reich, J. Maultzsch, C. Thomsen, and P. Ordejón. Tight-binding description of graphene. *Phys. Rev. B*, 66(3):035412, Jul 2002.

[101] Joshua A. Robinson, Eric S. Snow, Stefan C. Badescu, Thomas L. Reinecke, and F. Keith Perkins. Role of defects in single-walled carbon nanotube chemical sensors. *Nano Letters*, 6(8):1747–1751, 2006.

[102] R. Saito, G. Dresselhaus, and M. S. Dresselhaus. *Physical Properties of Carbon Nanotubes*. World Scientific Publishing Company, 1st edition, September 1998.

[103] R. Saito, M. Fujita, G. Dresselhaus, and M. S Dresselhaus. Electronic structure of chiral graphene tubules. *Appl. Phys. Lett.*, 60(18):2204–2206, 1992.

[104] R. Saito and H. Kataura. Optical properties and Raman spectroscopy of carbon nanotubes. *Topics Appl. Phys.*, 80:213, 2001.

[105] Dror Sarid. *Scanning Force Microscopy: With Applications to Electric, Magnetic, and Atomic Forces*. Oxford University Press, USA, rev sub edition, August 1994.

[106] Philipp A. E. Schoen, Jens H. Walther, Salvatore Arcidiacono, Dimos Poulikakos, and Petros Koumoutsakos. Nanoparticle traffic on helical

tracks: Thermophoretic mass transport through carbon nanotubes. *Nano Letters*, 6(9):1910–1917, 2006.

[107] C. Schönenberger and S. F. Alvarado. Observation of single charge carriers by force microscopy. *Phys. Rev. Lett.*, 65(25):3162–3164, Dec 1990.

[108] Karlheinz Seeger. *Semiconductor Physics: An Introduction*. Springer, 9th edition, July 2004.

[109] James R. Sheats. *Microlithography Science and Technology*. CRC, 1st edition, May 1998.

[110] Zujin Shi, Yongfu Lian, Fuhui Liao, Xihuang Zhou, Zhennan Gu, Yaogang Zhang, and Sumio Iijima. Purification of single-wall carbon nanotubes. *Solid State Communications*, 112(1):35 – 37, 1999.

[111] E. S. Snow and F. K. Perkins. Capacitance and conductance of single-walled carbon nanotubes in the presence of chemical vapors. *Nano Lett.*, 5:2414, 2005.

[112] E. S. Snow, F. K. Perkins, E. J. Houser, Ş. C. Bădescu, and T. L. Reinecke. Chemical detection with a single-walled carbon nanotube capacitor. *Science*, 307:1942, 2005.

[113] Young-Woo Son, Marvin L. Cohen, and Steven G. Louie. Half-metallic graphene nanoribbons. *Nature*, 444(7117):347–349, November 2006.

[114] R. Sordan, K. Balasubramanian, M. Burghard, and K. Kern. Coulomb blockade phenomena in electromigration break junctions. *Appl. Phys. Lett.*, 87:013106, 2005.

[115] Sofia Sotiropoulou and Nikolas A. Chaniotakis. Carbon nanotube array-based biosensor. *Anal. Bioanal. Chem.*, 375:103, 2003.

[116] Alexander Star, Jean-Christophe P. Gabriel, Keith Bradley, and George Gruner. Electronic detection of specific protein binding using nanotube fet devices. *Nano Letters*, 3(4):459–463, 2003.

[117] Alexander Star, Tzong-Ru Han, Vikram Joshi, Jean-Christophe P. Gabriel, and George Grüner. Nanoelectronic carbon dioxide sensors. *Adv. Mater.*, 16:2049, 2004.

[118] Alexander Star, Vikram Joshi, Sergei Skarupo, David Thomas, and Jean-Christophe P. Gabriel. Gas sensor array based on metal-decorated carbon nanotubes. *The Journal of Physical Chemistry B*, 110(42):21014–21020, 2006.

[119] J. E. Stern, B. D. Terris, H. J. Mamin, and D. Rugar. Deposition and imaging of localized charge on insulator surfaces using a force microscope. *Appl. Phys. Lett.*, 53(26):2717–2719, 1988.

[120] Sander J. Tans, Alwin R. M. Verschueren, and Cees Dekker. Room-temperature transistor based on a single carbon nanotube. *Nature*, 393(6680):49–52, May 1998.

[121] Thiti Taychatanapat, Kirill I. Bolotin, Ferdinand Kuemmeth, and Daniel C. Ralph. Imaging electromigration during the formation of break junctions. *Nano Letters*, 7(3):652–656, 2007.

[122] Claes Thelander, Martin H. Magnusson, Knut Deppert, Lars Samuelson, Per Rugaard Poulsen, Jesper Nygrd, and Jørn Borggreen. Gold nanoparticle single-electron transistor with carbon nanotube leads. *Appl. Phys. Lett.*, 79(13):2106–2108, 2001.

[123] Adam W. Tsen, Luke A. K. Donev, Huseyin Kurt, Lihong H. Herman, and Jiwoong Park. Imaging the electrical conductance of individual carbon nanotubes with photothermal current microscopy. *Nat Nano*, advanced online publication, December 2008.

[124] Ryan Tu, Li Zhang, Yoshio Nishi, and Hongjie Dai. Measuring the capacitance of individual semiconductor nanowires for carrier mobility assessment. *Nano Letters*, 7(6):1561–1565, 2007.

[125] Katsunori Wakabayashi. Electronic transport properties of nanographite ribbon junctions. *Phys. Rev. B*, 64(12):125428, Sep 2001.

[126] Katsunori Wakabayashi, Mitsutaka Fujita, Hiroshi Ajiki, and Manfred Sigrist. Electronic and magnetic properties of nanographite ribbons. *Phys. Rev. B*, 59(12):8271–8282, Mar 1999.

[127] Katsunori Wakabayashi, Yositake Takane, and Manfred Sigrist. Perfectly conducting channel and universality crossover in disordered graphene nanoribbons. *Phys. Rev. Lett.*, 99(3):036601, 2007.

[128] P. R. Wallace. The band theory of graphite. *Phys. Rev.*, 71(9):622–634, May 1947.

[129] S. G. Wang, Q. Zhang, R. Wang, and S. F. Yoon. A novel multi-walled carbon nanotube-based biosensor for glucose detection. *Biochem. Bioph. Res. Co.*, 311:572, 2003.

[130] C. M. Wayman and T. P. Darby. Nucleation and growth of gold films on graphite : Ii. the effect of substrate temperature. *Journal of Crystal Growth*, 28(1):53 – 67, 1975.

[131] M. Whitby and N. Quirke. Fluid flow in carbon nanotubes and nanopipes. *Nat Nano*, 2(2):87–94, February 2007.

[132] Jeroen W. G. Wilder, Liesbeth C. Venema, Andrew G. Rinzler, Richard E. Smalley, and Cees Dekker. Electronic structure of atomically resolved carbon nanotubes. *Nature*, 391(6662):59–62, 1998.

[133] K. R. Williams, K. Gupta, and M. Wasilik. Etch rates for micromachining processing-part ii. *Microelectromechanical Systems, Journal of*, 12(6):761–778, Dec. 2003.

[134] S. J. Wind, J. Appenzeller, R. Martel, V. Derycke, and P. Avouris. Fabrication and electrical characterization of top gate single-wall carbon nanotube field-effect transistors. volume 20, pages 2798–2801. AVS, 2002.

[135] Jacob N. Wohlstadter, James L. Wilber, George B. Sigal, Hans A. Biebuyck, Mark A. Billadeau, Liwen Dong, Alen B. Fischer, Satyanarayana R. Gudibande, Stephanie H. Jameison, John H. Kenton, Joseph Leginus, Jonathan K. Leland, Richard J. Massey, and Samuel J. Wohlstadter. Carbon nanotube-based biosensor. *Adv. Mater.*, 15:1184, 2003.

[136] Zhiping Xu, Quan-Shui Zheng, and Guanhua Chen. Elementary building blocks of graphene-nanoribbon-based electronic devices. *Appl. Phys. Lett.*, 90(22):223115, 2007.

[137] Liu Yang and Jie Han. Electronic structure of deformed carbon nanotubes. *Phys. Rev. Lett.*, 85:154, 2000.

[138] Philip Young, Yijiang Lu, Roger Terrill, and Jing Li. High-sensitivity no2 detection with carbon nanotubegold nanoparticle composite films. *Journal of Nanoscience and Nanotechnology*, 5(9):1509–1513, 2005.

[139] L. H. Yu and D. Natelson. The kondo effect in c60 single-molecule transistors. *Nano Lett.*, 4:79, 2004.

[140] T. D. Yuzvinsky, A. M. Fennimore, and A. Zettl. Engineering Nanomotor Components from Multi-Walled Carbon Nanotubes via Reactive Ion Etching. In H. Kuzmany, S. Roth, M. Mehring, and J. Fink, editors, *American Institute of Physics Conference Series*, volume 723 of *American Institute of Physics Conference Series*, pages 512–515, September 2004.

[141] Guangyu Zhang, Pengfei Qi, Xinran Wang, Yuerui Lu, Xiaolin Li, Ryan Tu, Sarunya Bangsaruntip, David Mann, Li Zhang, and Hongjie Dai. Selective Etching of Metallic Carbon Nanotubes by Gas-Phase Reaction. *Science*, 314(5801):974–977, 2006.

[142] Guangyu Zhang, Pengfei Qi, Xinran Wang, Yuerui Lu, David Mann, Xiaolin Li, and Hongjie Dai. Hydrogenation and hydrocarbonation and etching of single-walled carbon nanotubes. *Journal of the American Chemical Society*, 128(18):6026–6027, 2006.

[143] Y. Zhang and Hongjie Dai. Formation of metal nanowires on suspended single-walled carbon nanotubes. *Appl. Phys. Lett.*, 77(19):3015–3017, 2000.

[144] V. P. Zharov and D. O. Lapotko. Photothermal imaging of nanoparticles and cells. *Selected Topics in Quantum Electronics, IEEE Journal of*, 11(4):733–751, July-Aug. 2005.

[145] L. X. Zheng, M. J. O'Connell, S. K. Doorn, X. Z. Liao, Y. H. Zhao, E. A. Akhadov, M. A. Hoffbauer, B. J. Roop, Q. X. Jia, R. C. Dye, D. E. Peterson, S. M. Huang, J. Liu, and Y. T. Zhu. Ultralong single-wall carbon nanotubes. *Nature Mater.*, 3:673, 2004.

[146] Xin Zhou, Hu Chen, and Ou-Yang Zhong-can. Can electric field induced energy gaps in metallic carbon nanotubes? *Journal of Physics: Condensed Matter*, 13(27):L635–L640, 2001.

[147] Xinjian Zhou, Ji-Yong Park, Shaoming Huang, Jie Liu, and Paul L. McEuen. Band structure, phonon scattering, and the performance limit of single-walled carbon nanotube transistors. *Phys. Rev. Lett.*, 95:146805, 2005.

[148] A. Züttel, P. Sudan, Ph. Mauron, T. Kiyobayashi, Ch. Emmenegger, and L. Schlapbach. Hydrogen storage in carbon nanostructures. *International Journal of Hydrogen Energy*, 27(2):203 – 212, 2002.